UC Berkeley
UC Berkeley Electronic Theses and Dissertations

Title
Study of Laser Melted Liquids and of Interfacial Ions by Nonlinear Spectroscopy

Permalink
https://escholarship.org/uc/item/8jv4d4kw

Author
Hull, Christopher James

Publication Date
2019

Peer reviewed|Thesis/dissertation

eScholarship.org Powered by the California Digital Library
University of California

Study of Laser Melted Liquids and of Interfacial Ions by Nonlinear Laser Spectroscopy

By

Christopher Hull

A dissertation submitted in partial satisfaction of the

requirements for the degree of

Doctor of Philosophy in

Chemistry

In the

Graduate Division

Of The

University of California, Berkeley

Committee in charge:

Professor Rich Saykally, Chair

Professor Naomi Ginsburg

Professor Alessandra Lanzara

Fall 2019

Abstract

Study of Laser Melted Liquids and of Interfacial Ions by Nonlinear Laser Spectroscopy

By Christopher Hull

Doctor of Philosophy in Chemistry

University of California, Berkeley

Professor Richard Saykally, Chair

The content of this thesis can be broken into two distinct parts. The first summarizes experimental efforts to develop a better understanding of the structure and properties of liquid carbon and silicon after melting appropriate targets with an intense femtosecond laser pulse. Further research into the properties and structure of liquid carbon, particularly that focused on understanding the relationship between the thermodynamic state of the liquid and the material properties, is critical for resolving the many current controversies. Moreover, as laser synthesis grows in popularity as a tool for the production of nanomaterials, it has become increasingly critical to characterize the liquid melt which serves as an intermediate in the synthesis process, as well as the ensuing nucleation of nanostructures in the melt. To address these issues, we have carried out experiments on laser melted graphite and silicon substrates using a wide array of techniques including linear and non-linear laser spectroscopy as well as x-ray scattering to study the properties of the liquids on ultrafast timescales. The results of these studies provided new insights both into the structure and properties of the non-thermally melted liquid as well as the subsequent dynamics of the ablation plume that forms after laser melting.

The second half of the text discusses nonlinear spectroscopy experiments studying the thermodynamics of ion solvation at the water surface in solutions containing surfactants or mixed salts. Only recently has it been recognized that certain specific anions exhibit enhanced interfacial populations relative to the solution bulk. The interfacial affinity for these ions that accumulate at the interface follows the inverse of the well-known Hoffmeister series. The physics that drive these ions to accumulate at the water surface, contradicting predictions from older theories of ion solvation, remain incompletely understood. The presence of these ions, however, has profound implications for biology and atmospheric chemistry. As such, it is critical to further advance our understanding of the mechanisms that result in selected ions localizing to the interface. The nonlinear optics experiments detailed in the second half of this thesis expand the understanding of the interfacial solvation physics of ions by extending beyond the simple single salt systems studied in previous work. Measurement of the thermodynamics of ion adsorption in these more complex solutions permits the validity of different thermodynamics models of ion adsorption to be assessed and so facilitates the development of a universal model for ion solvation physics at the interface between media. Additionally, the systems studied in the

experiments detailed in this thesis are relevant to real-world atmospheric and biological systems and may lead advances in these areas.

Chapter 1 is a review of the extant literature on the properties and structure of liquid carbon. The importance of studying the properties of the liquid is discussed, as are the difficulties inherent in such experiments. The chapter then discusses previous attempts to study liquid carbon via both experiment and simulations, comparing the findings of different investigators. In doing so, the chapter highlights the many controversies regarding this intriguing substance

Chapter 2 discusses our efforts to expand the understanding of the properties of the liquid state of carbon through ultrafast spectroscopy measurements carried out on liquid carbon samples prepared via the ultrafast melting of graphite substrates. Optical reflectivity was employed to study the production and subsequent ablation dynamics of the laser-prepared liquid carbon. The results are found to be in good agreement with those carried out by other investigators, and provide additional support for liquid carbon being metallic at graphitic density. Second harmonic generation was then employed to study the interfacial properties of the graphite melt. These experiments aimed to develop a better understanding the coordination environment at the liquid carbon surface, as well as to characterize the proposed synthesis of carbon nanomaterials that might be nucleated at the liquid carbon/air interface. However, success in these nonlinear optical experiments was hindered by the presence of a large background from blackbody radiation resulting from the high temperatures in the liquid carbon melt.

In chapter 3, the structure and dynamics of a of liquid silicon ablation plume derived from ultrafast melting of a silicon substrate were studied via ultrafast small angle x-ray scattering. Previous experiment attempting to use x-ray techniques in the study of laser-melted liquids. like liquid carbon and liquid silicon, were hindered by the poor temporal resolution of the available synchrotron x-ray sources, which have x-ray pulse lengths with durations on the order of the liquid lifetime. Here we exploited the ultrafast x-ray pulses available from x-ray free electron lasers to carry out grazing incidence x-ray scattering from liquid silicon as it ablates and expands. In the resultant scattering pattern, we observed the formation of liquid droplets in the ablation plume at 20 ps after laser interaction. These droplets are speculated to result from phase explosion in the laser melt and are the precursors to nanomaterials that nucleate in the plume on longer timescales.

Chapter 4 describes the study of ions at the air/water interface. The chapter gives an overview of the physics of ions at the air/water interface, starting with the WOS model of image charge repulsion and the conclusions drawn from early surface tension measurements. It then describes the first experimental evidence from atmospheric field studies for the presence of ions at the air-water interface, followed by an overview of the simulations and experiments that confirmed the presence of certain anions in the interfacial region. The last section of the chapter reviews the current understanding of the driving forces which cause certain ions to localize at the

interface and discusses the need for additional experimental measurements of ion adsorption thermodynamics in more complex systems.

Chapter 5 discusses deep UV resonant second harmonic generation spectroscopy experiments studying the effect that adding a surfactant to the solution surface has on the adsorption thermodynamics of ions at the air/water interface. Surfactants play an important role in atmospheric chemistry and, according to some proposed mechanisms for the adsorption of ions to aerosol interfaces, should significantly impact the adsorption thermodynamics. In our experiments, it was found that the presence of a carboxylic acid monolayer at the air/water interface results in the complete loss of resonant second harmonic signal from thiocyanate anions, implying that the presence of the acid suppresses the surface affinity of the anion. Alternatively, neutral dodecanol monolayers were found to decrease the surface thiocyanate population through blocking of interfacial adsorption sites, but did not quench the SHG signal entirely, as was seen for the stearic acid. In agreement with previous second harmonic generation studies of ion adsorption at dodecanol monolayers, the free energy of adsorption for the thiocyanate anion at the dodecanol coated water surface was found to be identical to the energy of adsorption at the neat air/water interface. The observed unchanged adsorption thermodynamics is attributed to the persistence of a population of alcohol-free sites at the interface where the thiocyanate can adsorb without interference from the surfactant. Finally, the addition of a positively charged monolayer of the surfactant cetyltrimethylammonium bromide at the interface was found to result in the formation of ion pairs between the surfactant cation and the probed anions thiocyanate and iodide, greatly increasing the surface populations of both species. Bromide, which exhibits lower propensity for ion pairing with the CTA^+ cation, displayed no such surface enhancement. From these results it was clear that the specific ion interactions dominated over electrostatics in the case of the cetyltrimethylammonium bromide monolayers.

Chapter 6 discusses experiments to determine the effect that addition of NaCl as a competing salt had on the surface adsorption of the thiocyanate anion. Again, the surface population and thermodynamics of adsorption for the thiocyanate were measured via deep UV second harmonic generation spectroscopy. In the presence of the NaCl it was observed that the free energy of adsorption for thiocyanate decreased slightly, likely due to the thiocyanate preferentially displacing the chloride at the interface as the surface approaches saturation. The number density of thiocyanate ions at the interface was also observed to increase in the presence of the background salt. This increase in detected thiocyanate was proposed to be a consequence of an increases in the laser probe depth in the experiment due to increased screening lengths at the high total salt concentrations employed.

This thesis contains a single appendix wherein the data acquisition and analysis processes for the second harmonic experiments are discussed in detail.

Acknowledgements

Like most entering graduate school, I wasn't really sure what sort of research I was interested in pursuing in my graduate career save that I was definitely interested in laser spectroscopy of some sort. I was, however, pretty sure what it was that I didn't want to do. I had zero interest in any research involving second order non-linear optics. No SHG and no SFG, that was supposed to be a rule. Part of the rationale was, having worked in a non-linear optics lab as an undergraduate, I wanted the chance to become familiar different spectroscopic techniques in my graduate career. Equally important though, I was well aware of the difficulties and frustrations inherent in the experiments when spectroscopy left linearity behind.

It's a testament to Rich's force of personality that he somehow managed to convince me to change my mind and to sign on to six years of non-linear optical spectroscopy in his research group. Coming to the end of my time in the group now I can honestly say that, despite the fact that the experiments could at times be every bit as onerous as I had expected them to be, I certainly don't regret making that choice to join Rich's group. He has been a fantastic mentor throughout my time here at UC Berkeley, with no shortage of idea, most of them good, for things to try and experiments to carry out. In Rich's group I've still had the privilege to have been able to get hands on experience with a wide variety of different techniques and experiments, from non-linear optics to x-ray spectroscopy. I've also had the chance to travel the world, seeing Japan, Korea and Italy all in the space of a few years. Needless to say, I certainly owe Rich a great deal for having provided me with all of these amazing opportunities.

I would also like to offer the greatest of thank the rest of the Saykally group members, both past and present. Despite working in a laser lab as an undergraduate, I entered the Saykally group with almost no hand-on laser experience, the graduate students at Northwestern not being keen on letting a clumsy undergrad play with their carefully aligned laser systems. Without the tutelage of the many older graduate students in the group I'd probably still be stuck trying to figure out how to turn on the laser. As a senior student in the group myself now, I can only hope I've been a fraction as competent in teaching the newer student in the group as my predecessor were in teaching me. I would also especially like to give special thanks to fellow researcher on the liquid carbon front Sumana Raj. We spent way too many hours over the past few years discussing our experiments and scratching out heads as we tried to figure out liquid carbon. Without someone else working on liquid carbon to bounce ideas off, I have no idea how I would have gotten through all these years of liquid carbon research.

I would like to thank the Bay Area Scientist in Schools program (BASIS). Through BASIS I was continuously reminded of the importance of sharing knowledge of and passion for science to those outside of the field. Whenever things got rough in lab, I could always rely on the enthusiasm of a classroom of young future researchers to remind me why it is I chose to study science. Working with the program also introduced me to the world of non-profit work, something I had no idea I even had any interest in but that I hope to continue to be heavily involved with in the future.

Finally I would like to offer a heartfelt thanks to family and friends for the critical task of keeping me sane throughout the up and downs of graduate school. Without their support it's doubtful I'd ever have made it this far.

Table of Contents

Chapter One: Liquid Carbon 1

Introduction 1

The Carbon Phase Diagram 3

Why Study Liquid Carbon? 5

Computer Simulations of Liquid Carbon 8

Experimental Studies of Liquid Carbon 10

Conclusions 13

Chapter Two: Optical Characterization of Liquid Carbon 19

Introduction 19

Non-Thermal Melting 19

Reflectivity Measurements of Liquid Carbon 24

Second Harmonic Generation Spectroscopy Experiments on Liquid Carbon 35

Conclusions 45

Chapter Three: X-ray Scattering from Liquid Silicon 48

Introduction 48

Free Electron Lasers 48

X-ray Scattering 50

X-ray Scattering from Liquid Silicon 53

Conclusions 58

Chapter Four: On the Nature of Ions at the Air/Water Interface 62

Introduction 62

Ions at the Interface 62

Simulations of Interfacial Halides 65

Experimental Studies of Ions Near the Air/Water Interface 67

Mechanism for Ions Adsorption at Aqueous Interfaces 71

Conclusions 73

Chapter Five: Ion Adsorption at Water-Surfactant Interfaces 77

Introduction 77

Amphiphiles 77

Resonant Second Harmonic Generation at the Surfactant Interface 81

Effects of Surfactants on Thiocyanate Adsorption 92

Conclusions 107

Chapter Six: Ion Adsorption from Mixed Salt Solutions 111

Introduction 111

Motivations for Studying Mixed Salt Systems 111

Past Experiments on Mixed Salt Systems 112

Thiocyanate Surface Adsorption in the Presence of NaCl 114

Conclusions 128

Appendix A: 131

List of Figures and Tables

Chapter One:

Figure 1.1 Carbon phase diagram at low pressure 2

Figure 1.2 Carbon phase diagram at high pressure 4

Table 1.1 Carbon coordination in simulation of liquid carbon 8

Table 1.2 Liquid carbon resistivity as measured in various studies 11

Chapter Two:

Figure 2.1 Timescales of various processes relevant in ultrafast laser melting and ablation of solid substrates. 21

Figure 2.2 Diagram of inertial confinement of laser-prepared liquid 23

Figure 2.3 Experimental design for the reflectivity experiments 25

Table 2.1 Melting fluence for graphite as observed in previous studies 27

Figure 2.4 Excitation density in HOPG as a function of melting laser fluence at 800 nm 28

Figure 2.5 Liquid carbon reflectivity as a function of melting fluence 29

Figure 2.6 Plot of reflectivity vs. input intensity 30

Figure 2.7 Post-mortem microscope images of the melting and probe pulse craters 31

Figure 2.8 Time-dependent reflectivity of laser-melted HOPG 32

Figure 2.9 Schematic and state diagram for the SHG process 35

Figure 2.10 Experimental design used in the second harmonic generation experiments 38

Figure 2.11 Second harmonic signal for pristine unmelted graphite 40

Figure 2.12 Second harmonic generation plot for the laser-melted HOPG at t=0 41

Figure 2.13 Fluence dependence of background 42

Figure 2.14 Second harmonic intensity as a function of delay time after melting 44

Chapter Three:

Figure 3.1 Self amplified spontaneous emission process 51

Figure 3.2 Experimental setup for grazing incidence scattering experiments 55

Figure 3.3 X-ray scattering intensity measured at times of 10 ps and 20 ps after irradiation with a fs laser 56

Chapter Four:

Table 4.1 Free energy of adsorption for various anions at the air/water interface 69

Chapter Five:

Figure 5.1 Model of a surfactant molecule 78

Figure 5.2 Structures of the three utilized surfactants 82

Figure 5.3 Structure of sodium thiocyanate 83

Figure 5.4 CTTS transition for bulk thiocyanate 84

Figure 5.5 Top view of experimental set-up for SHG experiments 88

Figure 5.6 Side view of experimental set-up for SHG experiments 89

Figure 5.7 Signal trace for the input power in SHG experiments 90

Figure 5.8 Input power and SHG intensity trace for a 1M NaSCN solution in the absence of a stearic acid monolayer 92

Figure 5.9 SHG and reference traces in the presence of a stearic acid monolayer 93

Figure 5.10 SHG intensity as a function of the amount of stearic acid added 94

Figure 5.11 SHG intensity from pure water in the presence of stearic acid 96

Figure 5.12 SHG signal from thiocyanate solutions after the addition of 35 µL pentane 96

Figure 5.13 Adsorption isotherm for thiocyanate at the dodecanol interface 98

Table 5.1 ΔG_{ads} of thiocyanate to the dodecanol coated interface 99

Figure 5.14 Mechanism for thiocyanate adsorption to the dodecanol interface 100

Figure 5.15 Adsorption isotherm for thiocyanate solution with added stearic acid crystal 102

Table 5.2 Free energy for Stearic acid monolayer vs. the neat interface 103

Figure 5.16 SHG signal from NaSCN co-dissolved CTAB 104

Figure 5.17 Signal from solution of NaI co-dissolved with CTAB 105

Figure 5.18 SHG signal from a solution of NaBr with CTAB 106

Chapter Six:

Figure 6.1 Adsorption isotherm for thiocyanate anion in the presence of 1 M NaCl 116

Table 6.1 Values of ΔG_{ads} for thiocyanate from fitting isotherm 117

Figure 6.2 Adsorption isotherm for thiocyanate anion in solutions of pure NaSCN 118

Table 6.2 Thiocyanate ΔG_{ads} in different concentrations of NaCl. 119

Figure 6.3 Adsorption isotherms and best fit lines for thiocyanate solutions with added NaCl 120

Figure 6.4 Adsorption isotherm for thiocyanate anion with .5 M NaCl 121

Figure 6.5 Square root of the second harmonic signal intensity for pure NaSCN and 1M NaCl/NaSCN mixed salt solutions 124

Figure 6.6 Concentration dependence of visible SCN in pure SCN and 1M mixed salt solution 126

Appendix A

Figure A1 Signal processing schematic for SHG experiments 131

Figure A2 Example data trace for SHG experiments 132

Figure A3 Example histograms for SHG experiment 133

Figure A4 Example best fir line for SHG experiments 135

Chapter 1

Liquid Carbon

1.1 Introduction

We devote this first chapter to a discussion of the properties of liquid carbon and the controversies surrounding the liquid state. The unique properties exhibited by the many different extant carbon allotropes make carbon very attractive for use in a wide variety of industrial and technology applications, ranging from industrial lubricants[1,2] and abrasives[3], to nuclear reactor moderators[4], and to the anodes in lithium ion batteries[5]. The element's unmatched chemical versatility has resulted in carbon and carbon-based materials assuming an increasingly prominent role in the development of modern technologies. The economic importance of carbon technologies is only expected to grow, as newly-emergent carbon materials are applied in modern technology contexts. The market for advanced carbon materials (graphene and carbon nanotubes, foams, fibers) is expected to reach ca. $13 billion by 2025[6], a growth of nearly 10% in only a few years. The attractiveness of carbon materials for technology applications derives from the wide array of properties exhibited by carbon allotropes. These, in turn, are driven by carbon's ability to flexibly form single, double, and triple covalent bonds. This unmatched flexibility in bonding motifs endows carbon materials with a multitude of available atomic structures with differing mechanical and chemical properties. By tuning the degree of bonding in the solid, these properties can be specifically tuned for whatever application is desired.

As would be expected for such a critical class of materials, a great deal of scientific interest has been devoted to studying carbon in its many forms. Beyond the common phases graphite and diamond, which have been extensively studied[7–10], newer solid carbon materials and nanostructures like nanotubes, graphene and fullerenes, have increasingly received both experimental and theoretical attention[11–14]. The properties of the vapor phase have likewise been carefully analyzed via plume studies of ablated carbon plasmas[15,16] and spectroscopic studies of various C_n chains[17].

The main focus for the first half of this thesis, however, is on the liquid state of carbon. Liquid carbon, unlike the solid or gas states, has received comparatively little attention and our understanding of its properties accordingly remains limited. This lack of research on the liquid phase emanates from the difficulty in both preparing and carrying out measurements on carbon in its liquid state. In fact, as we will discuss in the next section, carbon in its liquid form exists only under extreme condition of temperature and pressure, like those found in planetary and stellar cores. As such, it is very difficult to generate samples of the liquid in the laboratory under equilibrium conditions. Due to that difficulty, coupled with the fact that the liquid state plays a seemingly negligible role in terrestrial chemistry and physics, the liquid has largely been ignored in modern carbon research. However, despite this esoteric nature, in the past decade it has become increasingly apparent that there are both fundamental and practical reasons to address this knowledge gap, and thus to advance our understanding of liquid carbon properties. As we

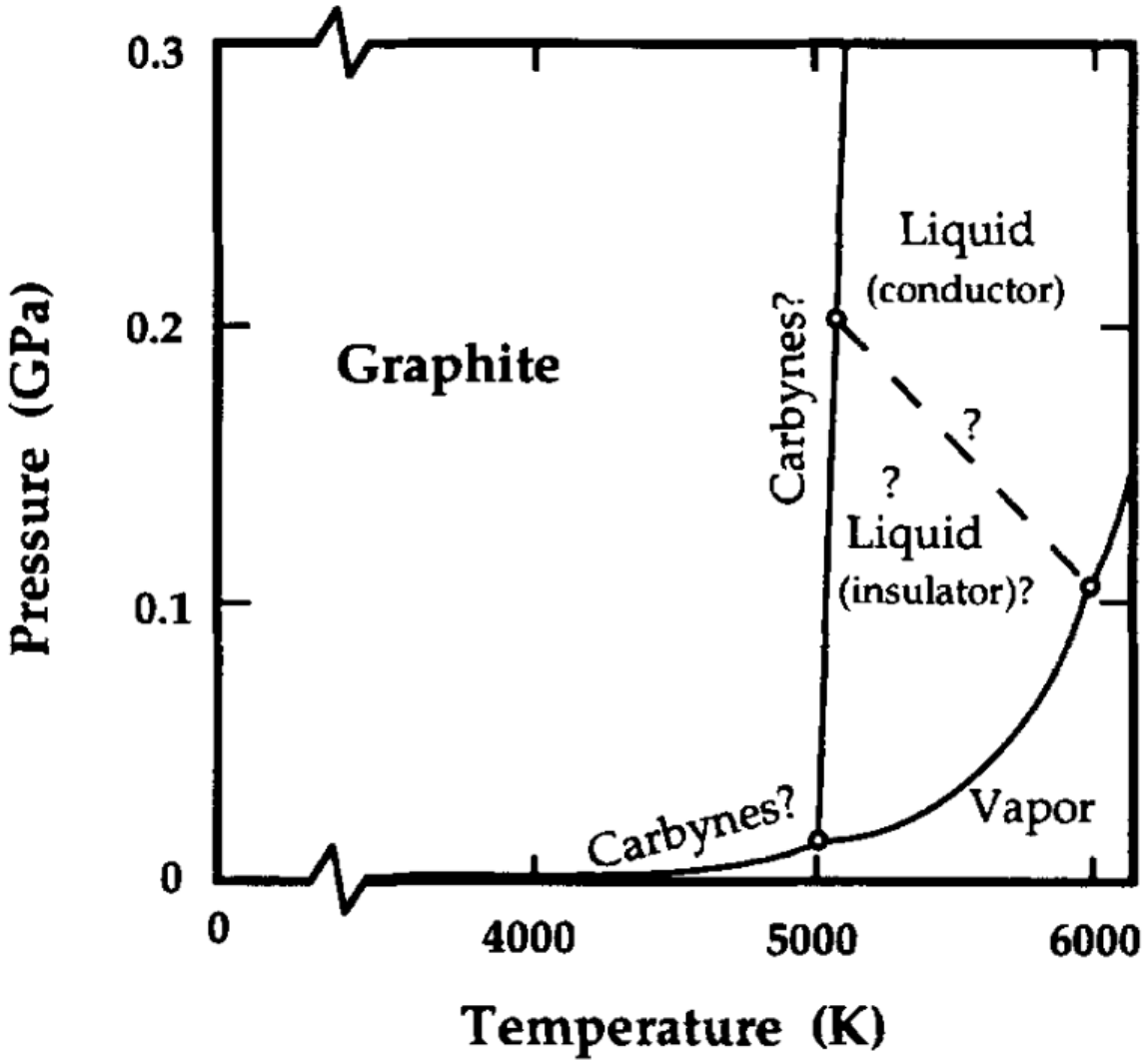

Figure 1.1: The carbon phase diagram at low pressure. Graphite sublimes to the gas phase when heated at ambient pressure. Reproduced from Reference 18.

shall see, however, experiments addressing the nature of liquid carbon are exceptionally difficult, and challenges remain in elucidating its properties.

1.2 The Carbon Phase Diagram

As can be seen from its position on the phase diagram in Figure 1.1, producing carbon in the liquid state presents a challenge. The liquid phase of carbon is favored only under extreme conditions, requiring temperature of ~5000 K and pressures of ca. tens of megapascal to produce an equilibrium sample. The necessity of achieving these conditions to produce the liquid is the chief difficulty in studying liquid carbon. Commonly used sample vessels cannot survive such extreme conditions, and, as such, maintaining the liquid under equilibrium conditions in a laboratory setting is nearly impossible. All experiments seeking to study the liquid state of carbon are thus ostensibly forced to produce the liquid a transient manner. As the gas phase is favored under conditions of high temperature, even these transiently produced liquids are short lived and quickly evaporate. This short sample lifetime is only one many difficulties that arise in trying to perform experiments on the liquid.

Beyond the position of the melt line, the shape of the curve has also drawn a great deal of attention from those studying the carbon phase diagram. The graphite melt line shows an inflection point near 4800K and 5 GPa. The existence of this inflection point has been the origin of much speculation regarding the structure of the liquid. The slope of the melt line is given by the Clausius-Clapeyron equation:

$$\frac{dP}{dT_m} = \frac{\Delta S_m}{\Delta V_m} \qquad (1.1)$$

Here P and T_m are the pressure and melting temperature, respectively, and ΔS_m and ΔV_m are the changes in entropy and volume upon melting. As can be seen in the high pressure phase diagram Figure 1.2 reproduced from Reference 18, due to the existence of the inflection point, the sign of the slope of the graphite melt line changes. As the entropy change upon melting should be positive, the change in sign is then due to a change in volume upon the phase transition. At low pressure, the melt line slope is positive, indicating a liquid which is less dense than graphite, while at high pressure the liquid is denser than graphite, as evidenced by the negative slope of the melt line. This change in the slope of the melting line has been interpreted by several investigators as evidence that the liquid may undergo a first order liquid-liquid phase transition (LLPT) from a low density liquid to a higher density liquid[19,20]. Such transitions have been predicted to occur in other tetrahedral liquids, including silicon[21,22] ,phosphorous[23,24] and for water[25,26].The existence of such a liquid-liquid phase transition in liquid carbon remains a point of contention and further experiments are clearly necessary to determine whether or not such a phase transition actually exists.

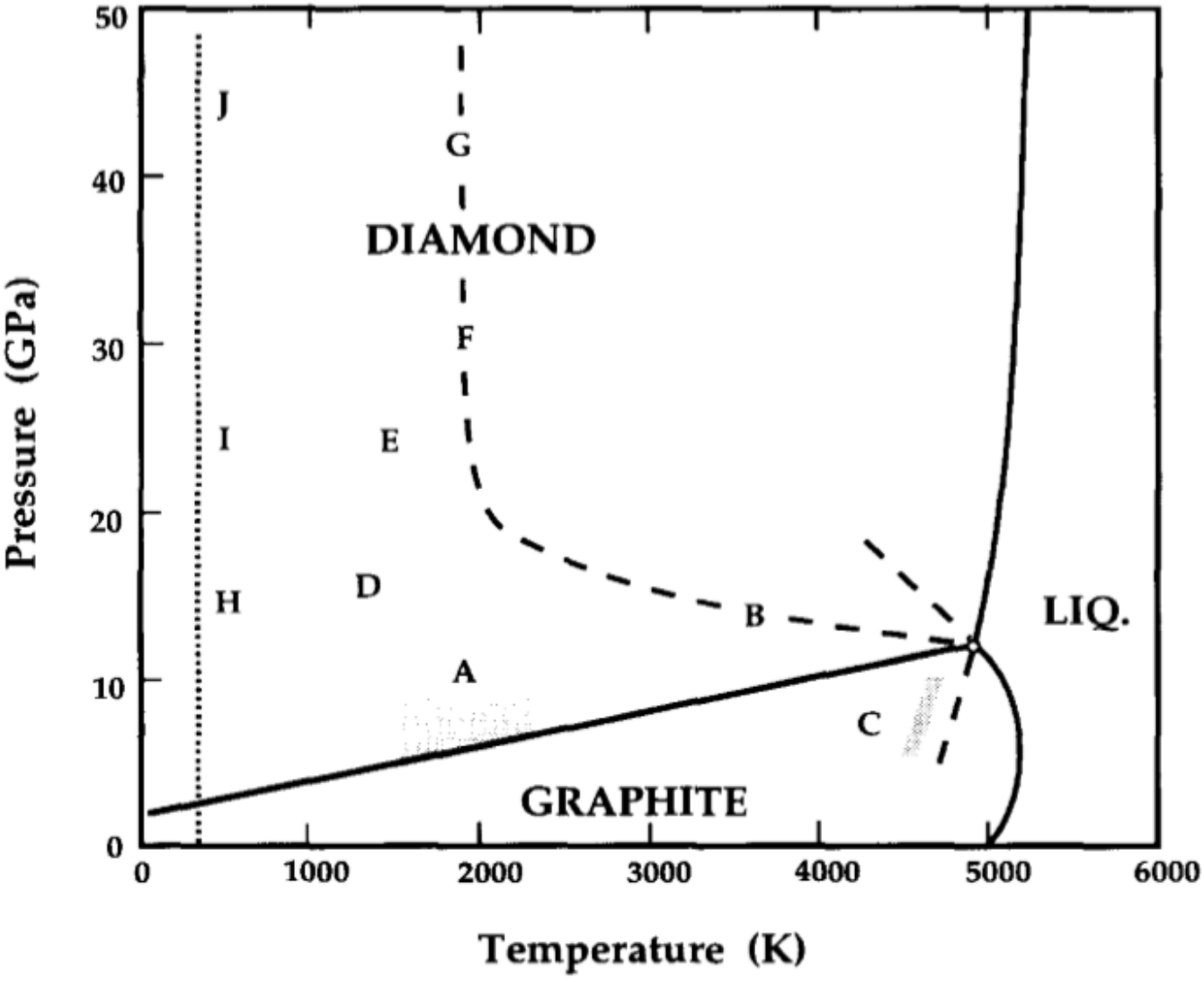

Figure 1.2: Carbon phase diagram at high pressure. The fact that the graphite melt line slope changes sign has been taken as evidence for a potential liquid-liquid phase transition. Reproduced from Reference 18.

1.3 Why Study Liquid Carbon?

As liquid carbon is a material naturally found in only the most extreme environments, it might seem as though there is little reason to undertake a detailed study of its properties-save for natural scientific curiosity. However, though rarely observed, understanding the properties of the liquid is potentially important in the modelling of both terrestrial and astrophysical systems, as well as being critical for the manufacture of emerging carbon materials.

1.3.1 Astrophysical phenomena

While the conditions necessary for the existence of liquid carbon are rarely found in terrestrial environments, such extremes of temperature and pressure are relatively common in astrophysics. Stellar and planetary interiors routinely reach the extreme conditions necessary for liquid carbon to exist in equilibrium[27]. As carbon is the 4th most abundant element in the universe[10,28], the existence of the liquid state in the cores of stars and gas giants is not only possible, but likely. As pointed out by Ross for instance[24], the thermodynamic conditions in the liquid central layers of planets like Uranus and Neptune favor the pyrolysis of methane gas into a mixture of elemental carbon and hydrogen. As such, understanding the properties of liquid carbon is critical in understanding the role it plays in planetary and stellar physics. It has been proposed that a highly conducting layer of metallic liquid carbon could be the source of the magnetic fields detected in gas giant planets[29–31]. However, the question of whether liquid carbon is indeed metallic has been long debated, as we will address later in this chapter, and other explanations for the origin of these planetary magnetic fields have become more widely accepted viz. metallic hydrogen[32]. Clearly, a better understanding of the properties of the liquid phase of carbon is necessary if we are to model this substance and evaluate its importance in planetary magnetic field generation. Our currently primitive understanding of the liquid state makes it difficult to predict how important liquid carbon is in astrophysical phenomena.

1.3.2 Tetrahedral liquids

Liquid carbon is of interest as a prototypical tetrahedrally bonding liquid. While most liquids are icosohedrally coordinated, with up to twelve nearest neighbors, tetrahedral liquids are highly structured, with only four nearest neighbors on average[33]. These liquids are of much experimental and theoretical interest as they often manifest unusual properties as a result of their unique structure. The tetrahedrally bonding liquid most commonly encountered is water, for which the unusual and complex phase diagram is a direct manifestation of its tetrahedral hydrogen-bonding structure.

Carbon is well-known for its ability to form up to four bonds with neighboring carbon atoms, as in its diamond phase. Simulations of the liquid carbon state have predicted that liquid carbon also forms a maximum of four bonds to its nearest neighbors[34,35]. As such, it may prove to be a good model system for testing general theoretical predictions made for tetrahedral liquids. The possibility for the existence of a liquid-liquid phase transition, for instance, is a unique property of tetrahedral fluids[36,37]. As of yet however, there exists little experimental evidence for the widespread existence of such phase transitions, although a vigorous current debate of this subject is ongoing[38–40]. Confirming the existence of such a transition in liquid

carbon would therefore provide valuable evidence for the possibility of such transitions in other tetrahedral liquids. Other properties may emanate from the tetrahedral structure as well. For example, predictions from a Stillinger-Weber model predict that liquid carbon should exhibit an anomalous increase in constant pressure heat capacity upon supercooling, but that the liquid should not exhibit the density anomaly found in some other tetrahedral liquids[41]. As of yet, no experimental data exist to test these predictions. Additional knowledge of the structure and properties of liquid carbon would greatly help to refine such models for tetrahedral liquids, which would advance our understanding, not only of liquid carbon, but of water and other tetrahedral liquids as well.

1.3.3 Advanced carbon materials

In terms of practical applications, liquid carbon has been proposed to be an intermediate in the synthesis of a variety of carbon nanomaterials of interest in modern technology, including nanotubes[10,13], nano-diamonds[42,43] and other novel materials. Liquid carbon is especially relevant to any process that injects large amounts of energy into the carbon substrate on short (ps or shorter) timescales, as this can transiently drive the material to the portion of the phase diagram where the liquid is thermodynamically stable[44]. As synthesis of carbon nanostructures and thin films via femtosecond and picosecond laser ablation grows in popularity due to low cost and high product yields, understanding this liquid intermediate may be vital for controlling the properties and uniformity of the resulting products.

Carbon nanotubes are already a rather widely used new carbon material[10,13]. Commercialization of carbon nanotubes, however, has been hindered by the difficulty in producing them with controlled uniform properties[10] like diameter and chirality. To address these difficulties, the physics of nanotube formation has been an area of fundamental interest[45,46]. Recent evidence suggests that liquid carbon may be vital in the synthesis under some common synthesis routes. De Heer studied the formation of carbon nanotubes by the catalyst-free arc discharge method, with an emphasis on elucidating the mechanism of nanotube formation[47]. In post-synthesis TEM images, large spherical droplets of amorphous carbon were observed to have deposited along the length of the arc-produced carbon nanotubes. He interpreted the presence of these droplets as evidence that the carbon nanotubes were nucleating from a liquid carbon intermediate state[47]. It remains unclear, however, why, if the resulting nanotubes do nucleate from a liquid intermediate, nanotubes rather than the more thermodynamically stable graphite phase, form.[48] As De Heer's mechanism cites the surface of liquid carbon droplets as the point of nanotube growth, perhaps undercooling of the liquid plays a role in this. To understand the role of the liquid during nanotube synthesis more data on the properties of the liquid and its surface are clearly needed.

Nano-diamonds are emerging as a critical new carbon technology, with applications in manufacturing[49,50], medicine[51,52], and sensing[42,43]. The most common procedure for nano-diamond synthesis involves the detonation of a mixture of TNT and RDX in a chamber of liquid water or inert gas, with the resultant nano-diamonds being produced in the explosion. This method has high yield, but results in a mixture of carbon product, requiring extensive purification to yield the desired nano-diamonds[42]. As such, newer, cheaper synthesis routes are desirable.

One promising new route for nano-diamond synthesis involves the ablation of a carbon target immersed in a liquid medium, commonly water. Termed laser ablation in liquid or LAL, in this approach to laser ablation synthesis the liquid acts to confine the laser produced plasma, increasing the temperature and pressure of the plume after laser irradiation[53]. In a recent study, Gorrini et al. synthesized nano-diamond from a graphite target irradiated in water with a 20 ns 248 nm laser pulse. The resulting nano-diamonds were then analyzed using Raman and electron spectroscopies[54]. Applying Fabbro's[55]model to map the thermodynamic trajectory of the carbon in the confined plume, they proposed that the nano-diamonds nucleate from a supercooled liquid carbon. Under the confinement of liquid water, the laser-irradiated pyrolytic carbon target reaches the extreme temperatures and pressures at which liquid carbon is thermodynamically stable. The liquid carbon plume then expands and supercools, nucleating the nano-diamonds as a stable colloid. This same mechanism was also described in the synthesis of N-vacancy doped nano-diamonds produced in a similar manner[56]. As with nanotubes, better understanding of the properties of the liquid may help with refining this synthetic process, resulting in better yield, higher degrees of homogeneity and reduced cost.

Laser synthesis of carbon materials is being increasingly applied to create novel phases of carbon with interesting properties. One exciting new carbon material is Q-carbon, an amorphous carbon with a high degree of sp^3 content, first synthesized and reported by Narayan et al[57]. As with the nano-diamonds discussed previously, the Q-carbon is believed to be synthesized from an undercooled liquid carbon, prepared via nanosecond excimer laser irradiation of a graphite target. It has a wealth of very interesting and potentially useful properties, including a predicted hardness higher than that of diamond, ferromagnetism, and high temperature superconductivity[57–59]. Critically, the successful synthesis of Q-carbon, as opposed to the more typical diamond or graphite phases, requires careful control of the incident laser power and the starting film morphology[59]. This is an example of how controlling the properties of the intermediate liquid can allow for tuning of the properties and phase of the end product.

The many available bonding arrangements of carbon result in many different possible structures with potentially unique properties. One novel class of carbon-based materials, called novamenes, was proposed and modelled using DFT calculations by Birchfield et al[60]. This new class of carbon materials is comprises a combination of the graphite and diamond lattice structures with a combination of sp^2 carbon rings fully surrounded by diamondlike sp^3 carbon. Simulations carried out on the simplest of these structures, the single ring novamene, predicted it to be a small bandgap semiconductor with a density intermediate between that of graphite and diamond. These authors speculated that the previously discussed Q-carbon could perhaps be one of these novamene-class materials, although there was insufficient evidence to determine whether or not that was the case. Even if Q-carbon is not related to the novamenes, with careful tuning of the liquid properties by varying melt fluence and starting substrate density, it is possible that these interesting novamene materials could be synthesized in an analogous manner.

1.4 Computer Simulations of Liquid Carbon

1.4.1 Structural simulations

With the high temperatures and pressure necessary to generate equilibrium liquid carbon so difficult to maintain in a laboratory setting, simulations have become a principal tool for elucidating its properties. One of the earliest simulations of liquid carbon was carried out by Gallli and Martin in 1989[61]. In their molecular dynamics study, an amorphous carbon precursor with an initial density of 2 g/cm^3 was heated to a temperature of 5000 K. The initially solid carbon was observed to melt at a temperature of around 4500 K, as judged by diffusion of the carbon atoms in the simulation, a melting temperature consistent with predictions from early carbon phase diagrams. The liquid in their simulation proved to be a metal, with the energy of the π and π* bands beginning to overlap and then merge as the carbon underwent the solid/liquid phase transition. Structurally, the liquid in the simulation was observed to be a mixture of two-, three - and four-coordinated carbon atoms, with the recorded ratio detailed in Table 1.1. The average coordination in the system was measured to be 2.9 nearest neighbors per atom[61]. While the fourfold coordinated carbon was quite unlike diamond, with variable bond lengths and bonding angles, the threefold coordinate sites could be regarded as slightly distorted sp^2 hybridized carbons, with bond angles near 120^o and bond lengths near 1.5 Angstroms. The twofold coordinate carbons were mostly seen as sp-bound chains, similar to the proposed carbyne phase in early carbon phase diagrams.

Coordination	Simulation population
Two-fold coordinated	32%
Threefold coordinated	52%
Fourfold coordinated	16%

Table 1.1: Carbon coordination in simulation of liquid carbon in Reference 61.

Subsequent studies on the structure of the liquid illustrated that there existed a strong correlation between the liquid structural properties and density. Wang et al.,[62] carried out molecular dynamics simulations on the liquid and found good agreement with Galli et al. for a carbon material of density near 2 g/cm^3, noting that the system was dominated by threefold coordination. However, the liquid structure was found to change dramatically with density of the starting material. At low densities, ca. ~1.5 g/cm^3, twofold coordinate carbon was found to dominate the liquid, accounting for 60-70% of all atoms in their simulation box. Meanwhile at densities of ca. 3.5 g/cm^3, the three-fold coordinate carbon was still the dominant species, but the share of twofold carbon dropped off quickly while fourfold-coordinated carbon atoms began to make up a significant portion of the total species [62]. At all densities studied, the liquid was found to exhibit metallic character, providing further support for the notion that liquid carbon is

indeed a metal. Later studies did observe that the conductivity increased, and then decreased with increasing density of the liquid, likely due to the shifting degree of sp^2 bonding in the liquid.[63]

A common observation in most simulations of liquid carbon was that the average coordination was quite low for a liquid. In Wang's simulation, the average coordination was found to vary from ~2.1 at low densities of 1.2 g/cm^3 to 3 at higher densities of 2.68 g/cm^3 [62]. Harada et al[34] studied the electronic structure of the liquid with a particular interest in its dependence on the system pressure. At low densities, it was observed that there existed pronounced anisotropic electronic density surrounding the carbon atoms in the liquid, a sign that covalent bonding persists in the liquid phase at these densities. This is a characteristic that liquid carbon shares with liquid silicon and explains the unusually low coordination in the melt. Bonding in liquid carbon, as with liquid silicon, is very short-lived, with an average bond lifetime of 100-200 fs. Simulations of the liquid as it cools ,however, imply that the bonds can have lifetimes that approach 1 ps or longer at lower temperatures, allowing for evolution of sp^2 domains in the solid[64]. At higher densities, on the order of 10 g/cm^3, the electron density is more uniformly distributed throughout the system and the covalent character is lost. Under these high-density conditions, more traditional metallic bonding dominates in the liquid.

1.4.2 Presence of the liquid-liquid phase transition

Based on the previously-observed inflection point in the melting line of graphite, it has long been proposed that liquid carbon might exhibit a liquid-liquid phase transition (LLPT), like those previously predicted for phosphorous and silicon[19]. As in silicon, it was proposed that the liquid structure should undergo a shift from a high density, highly conductive liquid to a low density insulator with a higher degree of sp bonding. Some of the first theoretical support for the existence of a liquid-liquid phase transition was provided by Glosli[65], who performed a molecular dynamics study of carbon at high temperature and pressure using a Brenner potential model. In his simulation, Glosli observed a transition from a fourfold coordinate-dominated liquid to a twofold coordinate-dominated fluid as a function of temperature. The graphite-liquid-liquid triple point was predicted to exist at 5133 K and 1.88 GPa. The simulation also found that sp^2 bonding was rare in the liquid, as the torsional barrier in pi-bonded systems led to low entropy. The absence of threefold coordination in the simulation was at odds with previous molecular dynamics studies[61]. These results were later challenged by Wu[20], who employed an *ab initio* molecular dynamics approach akin to that used by Galli. Contrary to Glosli's results, the simulated liquid carbon exhibited substantial degrees of sp^2 bonding and showed no evidence for an LLPT. Instead, in agreement with prior studies, the liquid coordination was found to vary smoothly as a function of pressure from sp-dominated liquids at low pressure to sp^3-dominated diamond-like liquid at high pressure. Glosli's observation of the phase transition in their MD simulations was attributed to the overestimation of the torsional barrier between threefold coordinate carbons.

The most recent investigation into the existence of an LLPT in liquid carbon occurred in 2014, when He et al. once again found evidence for the existence of an LLPT in liquid carbon[64]. In a study using classical molecular dynamics with long range carbon bond order potentials they observed a shift from a two-fold coordinate dominated liquid to a threefold coordinate dominated liquid as the system temperature dipped below 7900 K. The three-fold coordinate carbons that makeup the low temperature liquid were observed to have structure analogous to

sp^2 carbons in graphite and served as nucleation seeds for the eventual transition back to the solid state.

To conclude, while many simulations of liquid carbon have been carried out, consensus on the properties of the liquid is still mixed. It is now well-accepted that the coordination of the liquid is highly dependent on the liquid density and that the liquid displays metallic character. Other properties, like the existence of an LLPT remain contentious however, with simulations finding evidence both for and against its existence. To validate the various theoretical models for the liquid and test their predictions, it is critical that additional experimental measurements of the liquid be obtained. As we discuss in the next section, there has been little success in studying the liquid due to the difficulties inherent in the experiments. The results of experimental studies are often contradictory, and as such, have thus far done little to facilitate consensus regarding the properties of liquid carbon.

1.5 Experimental Studies of Liquid Carbon

1.5.1 Flash heating experiments

Preparing liquid carbon in a laboratory setting and in a manner compatible with appropriate characterization tools has been and remains a significant challenge. As the conditions necessary to transition to the liquid state are impossible to sustain in the laboratory, due to the extreme temperature and pressure requirements, samples must be generated transiently and are generally very short-lived. This puts significant constraints on the types of experiment that can be performed on the material, as these transiently generated samples usually only persist for picoseconds[44]. Additionally, as the density and temperature, both properties which strongly influence the structure and properties of the liquid, are expected to change as the prepared liquid carbon expands and cools, all experimental measurements to some degree tend to average over a range of differing liquid structures[44]. As a result, the apparent properties of the liquid may be strongly dependent on the timescale of both the liquid preparation and measurement. Nevertheless, and despite these challenges, a handful of experimental studies have successfully characterized some properties of the liquid state.

One of the earliest attempts to produce and characterize the liquid state of carbon were Bundy's flash heating experiments in 1962[66]. In these experiments, a graphite filaments contained in a high pressure cell was rapidly heated via a pulse of electrical current and the voltage drop a crossed the graphite filament were measured as a function of injected power. Recognizing the difficulty in maintaining a sample under the extreme conditions necessary to produce carbon in the liquid state, heating was carried out using a bank of capacitors, which could deliver the input energy on a timescale under 10 ms, allowing the graphite to be heated and subsequently cooled before significant damage to the containment cell could occur. By performing the experiment at a range of different pressures, the graphite melting curve was mapped out, revealing an inflection point at ~4600K and 5 GPa. The measured resistivity of the liquid was found to be lower than that of the initial graphite fibers, which was interpreted as evidence for the liquid being metallic.

Subsequent flash heating experiments carried out by Heremans improved on Bundy's initial efforts, using a faster capacitor bank that could deliver the necessary electrical current on microsecond rather than millisecond timescales[67]. As in the Bundy experiment, there was an observed decrease in the carbon resistivity following pulse heating. The measured resistivity for the liquid in the Heremans' experiment was, however, an order of magnitude lower than that obtained by Bundy, as can be seen in Table 1.2. This lower resistivity may be a result of the different measurement timescales in the two experiments. Regardless, based on the results from this pair of experiments, there was growing evidence that, as expected from earlier prediction, graphite in its liquid state was a metal.

The consensus on the properties of liquid carbon derived from flash heating experiments was, however, short lived. Already laser melting experiments, to be discussed in the next section, revealed conflicting evidence regarding the nature of the liquid. In 1997 Togaya carried out another series of flash heating measurements that seemed to imply that the liquid was, in fact, an insulator. Using a system similar to that used by Heremans, Togaya mapped out the melting curve for graphite, just as Bundy had previously.[19] His results for the phase diagram were in good agreement with Bundy's, revealing an inflection point at 4790 K and 5.6 GPa. His measured resistivity was markedly different, however, with a value that ranged from 600 μΩ cm at 0.4 GPa to 1000 μΩ cm at a pressure of 30 GPa, a full order of magnitude higher than Bundy's values. As such, while successful in mapping out the thermodynamically stable range for liquid carbon, these flash heating experiments served to create more controversy regarding the liquid's putative metallic character.

Experiment	Measured resistivity
Bundy (Ref 66, 1962)	150 μΩ cm
Heremans (Ref. 67, 1988)	30-70 μΩ cm
Togaya (Ref 19, 1996)	600-1000 μΩ cm
Reitze (Ref 72, from optical reflectivity) (1991)	625 μΩ cm
Cavalleri (Ref 68, optical reflectivity, Fullerite) (1992)	2 mΩ cm

Table 1.2: Liquid carbon resistivity as measured in various studies

1.5.2 Optical reflectivity experiments

With the advent of high-powered ultrafast laser systems came a new methodology for preparing liquid carbon via ultrafast non-thermal melting, a preparation method we will further discuss in later chapters. Earlier investigations using nanosecond lasers had established the capability to optically melt the sample surface, as evidenced by surface cratering following illumination. The properties of the melt could not be studied in these early experiments, however, as the ablation of the melted carbon layer obscured the surface on timescales shorter than the pulse duration[69]. Newly available picosecond and femtosecond lasers, however, provided sufficiently short pulses that it was assumed the optical properties of the melted carbon

could be studied before significant surface ablation could occur. The first experiments on the ultrafast laser melting of carbon were carried out by Malvezzi[70] in the mid-1980s. Graphite targets were melted using a 20 ps 532 nm pulse from a YAG laser and the resulting liquid reflectivity was probed using time delayed pulses at 532, 1064 and 1900 nm wavelengths. It was observed that above a critical melting laser threshold of .14 J/cm^{2,} there was a fluence-dependent decrease in the optical reflectivity, with higher input fluence resulting in a larger reflectivity loss. The change in the material reflectivity was taken as evidence that the laser had successfully induced a phase transition in the target, in accordance with earlier investigation into the ultrafast melting of silicon[71]. The decrease in reflectivity observed after laser irradiation of the graphite was taken as a sign that liquid carbon was an *insulator*, rather than a metal.

These results were later challenged by Reitze et al., who carried out a similar experiment using a femtosecond, rather than a picosecond, laser system as both the pump and probe. In contrast to Malvezzi's results, Reitze[72] observed first a short lived instantaneous *increase* in the optical reflectivity, followed by a long lived decay. The initial increase in reflectivity, which persisted for several ps, was attributed to the production of a metallic liquid carbon state. The observed reflectivity decay, Reitze argued, was the result of the development of a plasma plume as the liquid carbon ablated. The reflectivity loss observed by Malvezzi was therefore a result of the low time resolution of the 20 ps laser pulse used as the probe in those experiments. Using a Drude model, Reitze was able to extract a dc resistivity of 625 μΩ cm for the liquid, which compared favorably with some of the earlier resistivity measurements from flash heating. The experiment was also carried out using diamond as the melting target instead of graphite, with similar results for the observed reflectivity. Reitze argued that the initial increase in reflectivity upon melting of graphite and diamond was an indication of a transition to a liquid metal state upon melting. This opinion continued to be controversial, however, as further laser melting experiments carried out by Mavezzi[73] and Chauchard[74] found further evidence for the liquid being an insulator rather than metallic.

The most recent laser reflectivity measurements were carried out by Mincigrucci et al[75]. These reflectivity experiments were performed on laser-melted amorphous carbon with femtosecond deep UV pulses generated by the FERMI free electron laser in Trieste, Italy. Carrying out reflectivity measurements at wavelengths between 19 and 30 nm, their results showed a decrease in reflectivity beginning at about 0.8 ps after laser excitation. As the high frequency of the deep-UV laser pulses in these experiments resulted in their pulses being insensitive to the electron dynamics of the system, they argued that the reflectivity decrease they observed must be a result of hydrodynamic expansion, as was proposed by Reitze. They estimated that the liquid had a high free electron density of ca. ~10^{21} /cm^3, with the corresponding plasma frequency in the visible. The authors concluded, as did Reitze, that interpreting the results of optical reflectivity in the study of liquid carbon can be difficult, as the electronic and liquid expansion dynamics are inextricably linked.

1.5.3 X-ray studies of the liquid state

Experimental studies of liquid carbon have historically been more concerned with the liquid electronic properties than with its structure. This is because, until recently, there was a lack of x-ray sources with the appropriate time resolution and flux needed to observe the short-lived liquid state. A few x-ray studies have nonetheless been conducted on liquid carbon. In 2005, Johnson et al studied the bonding in laser-melted carbon using x-ray absorption spectroscopy at the Berkeley ALS synchrotron light source[76]. To compensate for the low time resolution of the x-ray pulses from the synchrotron source, which had x-ray pulse durations of 70 ps, their amorphous and diamond-like carbon targets were tamped with a thin layer of LiF, which served to temporarily delay the ablation of the liquid after melting, and results from the tamped and untamped samples were compared. The resulting x-ray absorption spectra were fit with peaks corresponding to the sigma and pi states of carbon solids, allowing for an estimate of the relative amounts of sigma vs. pi bonding in the fluid. The liquid was found to exhibit a higher degree of pi bonding than was observed in the unmelted carbon films, in agreement with the simulation results obtained by Galli[61] for the melting of amorphous carbon at intermediate densities. It was also observed that, in agreement with previous simulations of the liquid, density played an important role in determining bonding in the liquid. The *untamped,* low density liquid was found to favor primarily sp bonding, with an average of ~2.3 pi bonds per site. The higher density *tamped* films, in contrast, had an average pi bonding per site of 1.5. These results provided the first experimental evidence that the liquid *structure* depended on the system density, although only two different density points were examined in these experiments. Unfortunately, the low 70 ps time resolution of the synchrotron source precluded dynamics studies of the liquid.

In an attempt to more directly probe the atomic structure of the liquid, Kraus et al. performed x-ray scattering on a graphite target shock-compressed to 100 GPa with a ns laser[77]. Both elastic and inelastic scattering contributions were measured in a backscatter geometry at two different scattering angles, 105^{o} and 126^{o}. These angles were chosen because it was predicted that scattering at these angles should be especially sensitive to the shock induced phase change. The authors indeed observed an increase in the scattering intensity upon shocking the target, providing good evidence for the successful transition to the liquid phase. They found that their derived structure factor for the liquid could not be fit using simple Lennard-Jones or repulsive pair potentials, but compared favorably to the results of DFT-MD simulations. This result was interpreted as proof that the bonding in liquid carbon is complex and likely includes large contributions from different covalent interactions, as had been predicted by earlier simulations. The fact that only two scattering angles were measured, however, precluded a more detailed characterization of the liquid structure.

Conclusions

Clearly, many unanswered questions remain regarding the properties of liquid carbon. While theory has produced a wide array of predictions regarding the structure, phase diagram and electronic nature of the liquid, as of yet, few of these predictions have been experimentally tested and several of the predicted properties of the liquid remain controversial. On the

experimental side, the results of measurements are often conflicting and provide little concrete insight into the true nature of the liquid. Many of these apparent contradictions emanate from the fact that the liquid structure is highly dependent on its temperature, pressure and density at the time of measurement. In order to attain a better understanding of the liquid state, additional experiments designed to probe the electronics, structure, and bonding in the liquid as a function of its thermodynamic state are urgently needed. However, the extreme conditions necessary to generate the liquid, coupled with its short-lived nature, make such experiments on the liquid difficult to both carry out and interpret. Nevertheless, there is hope that by embracing new tools like x-ray free electron lasers and non-linear spectroscopies, we may soon resolve the interesting questions regarding the properties of the liquid state of carbon.

References:

1. Zhang, Z., Simionesie, D. & Schaschke, C. Graphite and Hybrid Nanomaterials as Lubricant Additives. *Lubricants* **2**, 44 (2014).
2. Peyvandi, A., Soroushian, P., Farhadi, N. & Balachandra, A. M. Evaluation of the Reinforcement Efficiency of Low-Cost Graphite Nanomaterials in High-Performance Concrete. *KSCE J. Civ. Eng.* **22**, 3875 (2018).
3. Lavrinenko, V. I. Current Advances in the Development of Abrasive Tools and Investigation of Diamond Abrasive Machining Processes (Materials Science Approach). Review INVESTIGATION OF MACHINING PROCESSES. *J. superhard Mater.* **40**, 69–78 (2018).
4. Institution of Electrical engineers. *Nuclear Reactor Types*. (Institution of Electrical engineers).
5. Yoshio, Masaki, Ralph J. Brodd, A. K. *Lithium-Ion Batteries*. (Springer, 2009).
6. Adroit Market Research. Advanced Carbon Materials Market will grow at a CAGR of 9.1% to hit $12.66 Billion by 2025 - Global Analysis by Trends, Size, Share, Business Opportunities and Key Developments: Adroit Market Research. 1 (2017).
7. Nostro, P. Lo & Ninham, B. W. Hofmeister Phenomena : An Update on Ion Specificity in Biology. *Chem. Rev.* **112**, 2286 (2012).
8. Chung, D. D. L. Review: Graphite. *J. Mater. Sci.* **37**, 1475 (2002).
9. Davies, G. *Properties and growth of diamond*. (INSPEC, the Institution of Electrical Engineers, 1994).
10. Pierson, H. *Handbook of Carbon, Graphite, Diamond and fullerenes: Properties, Processing and applications*. *Noyes Publication* (Sandia national Laboratories, 1993).
11. Geim, A. K. & Novoselov, K. S. The rise of graphene. *Nat. Mater.* **6**, 183 (2007).
12. Allen, M. J., Tung, V. C. & Kaner, R. B. Honeycomb Carbon: A Review of Graphene. *Chem.*

Rev. **110**, 132 (2006).

13. Saifuddin, N., Raziah, A. Z. & Junizah, A. R. Carbon nanotubes: A review on structure and their interaction with proteins. *J. Chem.* **18**, 76815 (2013).

14. Acquah, S. F. A. *et al.* Review—The Beautiful Molecule: 30 Years of C 60 and Its Derivatives. *ECS J. Solid State Sci. Technol.* **6**, M3155 (2017).

15. Shusser, M. Kinetic theory analysis of laser ablation of carbon: Applicability of one-dimensional models. *J. Appl. Phys* **101**, 33529 (2007).

16. Harilal, S. S. Expansion dynamics of laser ablated carbon plasma plume in helium ambient. *Appl. Surf. Sci.* **172**, 103 (2001).

17. Orden, A. Van & Saykally, R. J. Small Carbon Clusters: Spectroscopy, Structure, and Energetics. *Chem. Rev.* **98**, 2313 (1998).

18. Bundy, F. P. *et al.* The pressure-temperature phase and transformation diagram for carbon; updated through 1994. *Carbon N. Y.* **34**, 141 (1996).

19. Togaya, M. Pressure Dependences of the Melting Temperature of Graphite and the Electrical Resistivity of Liquid Carbon. *Phys. Rev. Lett.* **79**, 2474 (1997).

20. Wu, C. J., Glosli, J. N., Galli, G. & Ree, F. H. Liquid-Liquid Phase Transition in Elemental Carbon: A First-Principles Investigation. *Phys. Rev. Lett.* **89**, 1 (2002).

21. Sastry, S. & Angell, C. A. Liquid-liquid phase transition in supercooled silicon. *Nat. Lett.* **2**, 739 (2003).

22. Beye, Martin, Florian Sorgenfrei, William F. Schlotter , Wilfried Wurth, and A. F. The liquid-liquid phase transition in silicon revealed by snapshots of valence electrons. *PNAS* **107**, 16772 (2010).

23. Morishita, T. Liquid-Liquid Phase Transitions of Phosphorus via Constant-Pressure First-Principles Molecular Dynamics Simulations. *Phys. Rev Lett.* **87**, 105701 (2001).

24. Yoshinori Katayama, Takeshi Mizutani, W. U. & Osamu Shimomura, M. Y. & K. F. A first-order liquid-liquid phase transition in phosphorus. *Nature* **403**, 170 (2000).

25. Palmer, J. C., Poole, P. H., Sciortino, F. & Debenedetti, P. G. Advances in Computational Studies of the Liquid−Liquid Transition in Water and Water-Like Models. *Chem. Rev.* **118**, 9129 (2018).

26. Singh, R. S., Biddle, J. W., Debenedetti, P. G. & Anisimov, M. A. Two-state thermodynamics and the possibility of a liquid-liquid phase transition in supercooled TIP4P/2005 water. *J. Chem. Phys.* **144**, 144504 (2016).

27. Phillips, A. C. *The Physics of Stars*. (John Wiley and Sons, 1994).

28. Dufour, P., Liebert, J., Fontaine, G. & Behara, & N. White dwarf stars with carbon atmospheres. *Nature* **450**, 522 (2007).

29. Ross, M. The ice layer in Uranus and Neptune-diamonds in the sky? *Nature* **292**, 475 (1981).

30. F. Ancilotto, G. L. Chiarotti, S. Scandolo, E. T. Dissociation of Methane into Hydrocarbons at Extreme (Planetary) Pressures and Temperatures. *Science (80-.).* **275**, 1288 (1997).

31. Paleari, S. *et al.* THE EUROPEAN PHYSICAL JOURNAL D A new target design for laser shock-compression studies of carbon reflectivity in the megabar regime. *Eur. Phys. J. D* **67**, 136 (2013).

32. Zaghoo, M. & Collins, G. W. Size and Strength of Self-excited Dynamos in Jupiter-like Extrasolar Planets. *Astrophys. J.* **862**, 19 (2018).

33. Jabes, B. S., Nayar, D., Dhabal, D., Molinero, V. & Chakravarty, and C. Water and other tetrahedral liquids: order, anomalies and solvation. *J. Phys. Condens. Matter* **24**, 28411 (2012).

34. Harada, A., Shimojo, F. & Hoshino, K. Structural and electronic properties of liquid carbon: *ab initio* molecular-dynamics simulation. *J. Phys. Conf. Ser.* **98**, 042014 (2008).

35. Marks, N. A., Mckenzie, D. R., Pailthorpe, B. A., Bernasconi, M. & Parrinello, M. Ab initio simulations of tetrahedral amorphous carbon. *Phys. Rev Lett.* **54**, 9703 (1996).

36. Mcmillan, P. F. Polyamorphic transformations in liquids and glasses. *J. Mater. Chem* **14**, 1506 (2004).

37. Peter H Poole, I. S.-V. and F. S. Density minimum and liquid-liquid phase transition. *J. Phys. Condens. Matter* **17**, L431 (2005).

38. Harrington, S., Zhang, R., Poole, P. H., Sciortino, F. & Stanley, H. E. Liquid-Liquid Phase Transition: Evidence from Simulations. *Phys. Rev. Lett.* **78**, 2409 (1997).

39. Limmer, D. T. & Chandler, D. The putative liquid-liquid transition is a liquid-solid transition in atomistic models of water. II. *J. Chem. Phys.* **138**, 214504 (2013).

40. Limmer, D. T. & Chandler, D. The putative liquid-liquid transition is a liquid-solid transition in atomistic models of water. *J. Chem. Phys.* **135**, 134503 (2011).

41. Hujo, W., Shadrack Jabes, · B, Rana, V. K., Chakravarty, C. & Molinero, V. The Rise and Fall of Anomalies in Tetrahedral Liquids. *J Stat Phys* **145**, 293 (2011).

42. Kazi, S. A Review Article on Nanodiamonds Discussing Their Properties and Applications. *Int. J. Pharm. Sci. Invent. ISSN* **3**, 40 (2014).

43. Nagl, A., Robert Hemelaar, S. & Schirhagl, R. Improving surface and defect center chemistry of fluorescent nanodiamonds for imaging purposes-a review. *Anal Bioanal Chem* **407**, 7521 (2015).

44. Perez, D. & Lewis, L. J. Ablation of solids under femtosecond laser pulses. *Phys. Rev. Lett.* **89**, 255504 (2002).

45. Zhang, Y., Gu, H., Suenaga, K. & Iijima, S. Heterogeneous growth of B-C-N nanotubes by laser ablation. *Chem. Phys. Lett.* **279**, 264 (1997).

46. Gavillet, J. *et al.* Root-Growth Mechanism for Single-Wall Carbon Nanotubes. *Phys. Rev Lett.* **87**, 275504 (2001).

47. De Heer, W. A. *et al.* Liquid carbon, carbon-glass beads, and the crystallization of carbon nanotubes. *Science (80-.).* **307**, 907 (2005).

48. Harris, P. J. F. Solid state growth mechanisms for carbon nanotubes. *Carbon N. Y.* **45**, 229 (2007).

49. Cheng, X.-B. *et al.* Nanodiamonds suppress the growth of lithium dendrites. *Nat. Commun.* **8**, 336 (2017).

50. V Yu Dolmatov. Detonation synthesis ultradispersed diamonds: properties and applications. *Russ. Chem. Rev.* **70**, 607 (2001).

51. Shakeel Ahmed Ansari , Rukhsana Satar , Mohammad Alam Jafri , Mahmood Rasool, W. & Ahmad, S. K. Z. . Role of Nanodiamonds in Drug Delivery and Stem Cell Therapy. *Iran J Biotech.* **14**, e1320 (2016).

52. Tsai, L.-W. *et al.* Molecular Sciences Nanodiamonds for Medical Applications: Interaction with Blood in Vitro and in Vivo. *Int. J. Mol. Sci* **17**, 1111 (2016).

53. YANG, G. Laser ablation in liquids: Applications in the synthesis of nanocrystals. *Prog. Mater. Sci.* **52**, 648 (2007).

54. Gorrini, F. *et al.* On the thermodynamic path enabling a room-temperature, laser-assisted graphite to nanodiamond transformation. *Sci. Rep.* **6**, 5244 (2016).

55. Fabbro, R., Fournier, J., Ballard, P., Devaux, D. & Virmont, J. Physical study of laser-produced plasma in confined geometry. *J. Appl. Phys.* **68**, 775 (1990).

56. Basso, L. *et al.* An all-optical single-step process for production of nanometric-sized fluorescent diamonds. *Nanoscale* **10**, 5738 (2018).

57. Narayan, J. & Bhaumik, A. Novel phase of carbon, ferromagnetism, and conversion into diamond. *J. Appl. Phys* **118**, 215303 (2015).

58. Bhaumik, A., Sachan, R. & Narayan, J. High-Temperature Superconductivity in Boron-Doped Q-Carbon. *ACS Nano* **11**, 5351 (2017).

59. Narayan, J., Bhaumik, A., Gupta, S., Haque, A. & Sachan, R. Progress in Q-carbon and related materials with extraordinary properties. *Mater. Res. Lett.* **6**, 353 (2018).

60. Burchfield, L. A. *et al.* Novamene: A new class of carbon allotropes. *Heliyon* e00242 (2017).

61. Galli, G., Martin, R. M., Car, R. & Parrinello, M. Carbon: The Nature of the Liquid State. *Phys. Rev Lett.* **63**, 988 (1989).

62. Wang, C. Z., Ho, K. M. & Chan, C. T. Structure and dynamics of liquid carbon. *Phys. Rev. B* **47**, 14835 (1993).

63. Morris, J. R., Wang, C. Z. & Ho, K. M. Relationship between structure and conductivity in liquid carbon. *Phys. Rev. B* **52**, 4138 (1995).

64. He, Y., Li, H., Jiang, Y., Li, X. & Bian, & X. Liquid-liquid phase transition and structure inheritance in carbon films. *Sci. Rep.* 3635 (2014).

65. Glosli, J. N. & Ree, F. H. Liquid-Liquid Phase Transformation in Carbon. *Phys. Rev. Lett.* **82**, 4659 (1999).

66. Bundy, F. P. Melting of Graphite at Very High Pressure. *J. Chem. Phys* **38**, 618 (1963).

67. Heremans, J., Olk, C. H., Eesley, G. L., Steinbeck, J. & Dresselhaus, G. *Observation of Metallic Conductivity in Liquid Carbon*. **60**, (1988).

68. Cavalleri, K. Sokolowski-Tinten, D. Von der Linde, I. Spagnolatti, M. Bernasconi, G. Benedek, A. P. and P. M. Generation of the low-density liquid phase of carbon by non-thermal melting of fullerite Related content Modelling ultrafast laser ablation. *Europhys. Lett.* **57**, 281 (2002).

69. Venkatesan, T. *et al.* Measurement of Thermodynamic Parameters of Graphite by Pulsed-Laser Melting and Ion Channeling. *Phys. Rev. Lett.* **53**, 360 (1984).

70. Malvezzi, A. M., Bloembergen, N. & Huang, C. Y. Time-resolved picosecond optical measurements of laser-excited graphite. *Phys. Rev. Lett.* **57**, 146 (1986).

71. Shank, C. V., Yen, R. & Hirlimann, C. Femtosecond-time-resolved surface structural dynamics of optically excited silicon. *Phys. Rev. Lett.* **51**, 900 (1983).

72. Reitze, D. H., Wang, X., Ahn, H. & Downer, M. C. Femtosecond laser melting of graphite. *Phys. Rev. B* **40**, 986 (1989).

73. Malvezzi, A. M. & Romanoni, M. The Optical Properties of Graphite Under Intense Picosecond Laser Illumination t. *Int. J. Thermophys.* **13**, 131 (1992).

74. Chauchard, E. A., Lee, C. H. & Huang, C. Y. Graphite picosecond optoelectronic opening switch. *Appl. Phys. Lett* **50**, 812 (1987).

75. Mincigrucci, R. *et al.* Transient EUV Reflectivity Measurements of Carbon upon Ultrafast Laser Heating. *Photonics* **4**, 23 (2017).

76. Johnson, S. L. *et al.* Bonding in Liquid Carbon Studied by Time-Resolved X-Ray Absorption Spectroscopy. *Phys. Rev. Lett.* **94**, 57407 (2005).

77. Kraus, D. *et al.* Probing the Complex Ion Structure in Liquid Carbon at 100 GPa. *Phys. Rev Lett.* **111**, 255501 (2013).

Chapter 2

Optical Characterization of Liquid Carbon

2.1 Introduction

In this chapter, we discuss the preparation of liquid carbon via ultrafast laser melting and subsequent spectroscopic studies of the liquid. Lasers are attractive in such investigations because sample preparation is straightforward, requiring only irradiation of the substrate with a sufficiently intense laser pulse, and because the same laser system used to prepare the liquid sample can also serve as the experimental probe. Equally important, ultrafast lasers are ideally suited for carrying out these experiments because the short-lived nature of liquid carbon necessitates measurements of the liquid properties with high time resolution. As such, past studies have used ultrafast lasers to study not only liquid carbon[1,2], but liquid silicon[3,4], liquid GaAs,[5] and a variety of liquid metals[6]. Given the success of these past experiments, optical spectroscopy seemed an appropriate approach to investigate the properties of liquid carbon.

2.2 Non-Thermal Melting

2.2.1 Introduction to laser melting

For the experiments on liquid carbon discussed in this chapter, the liquid was produced via non-thermal melting with a femtosecond laser. This manner of preparation of the liquid carbon samples was selected both for its simplicity and because there exists a considerable literature[1,2,7] with which to compare the results of the measurement. We begin with a discussion of the physics via which the ultrafast laser pulse drives the initially solid substrate into the liquid state. The manner by which the laser pulse melts the target substrate can generally be divided into two separate pathways, thermal melting and non-thermal melting. As we will discuss in the following sections, while the product of these two different mechanisms may be identical, the respective physical mechanisms for liquid formation are quite different. The fluence threshold for initiating the melting transition can also differ significantly between the two methods[5,8]. Whether the non-thermal or thermal pathways is favored by a given substrate for melting after laser irradiation depends on the optical and thermodynamic properties of the target. In the case of the graphite targets used in the experiments discussed here, the non-equillibrium, non-thermal pathway provides a route for forcing the graphite targets into the liquid state, despite carbon favoring direct sublimation to the gas phase when heated at atmospheric pressures.

For both the thermal and the non-thermal pathways, the physics of the first few hundred femtoseconds after laser irradiation are identical[9]. When the optical laser pulse first impinges on the target simple optical absorption occurs, wherein the laser energy is absorbed via the excitation of electrons across the bandgap. The energy distribution of these excited electrons is initially in a highly non-equilibrium state. Over the course of a few tens of femtoseconds after excitation, this initially non-equilibrium distribution of electronic energies thermalizes to a Fermi-

Dirac distribution via carrier-carrier scattering, and it becomes possible to define a temperature for the electrons. At this point, the system is in a two-temperature state, with the electronic system at high temperature T_e due to the optical excitation and the ionic lattice temperature T_l ,defined by the phonon distribution, which is still cold. We emphasize this lack of thermal equilibrium between the electronic and ionic systems because it will be an important point going forward in defining the difference between the thermal and non-thermal melting pathways. It is at ~100 fs after laser irradiation that the thermal and non-thermal pathways diverge.

2.2.2 The mechanism of thermal melting

We begin by discussing the *thermal* melting pathway, as doing so will help illustrate the differences inherent in the *non-thermal* pathway discussed later. Trapped in the two-temperature state comprising hot electrons and a cold atomic lattice, the system attempts to restore thermal equilibrium by transferring energy from the electrons to the lattice through the emission of phonons. The characteristic timescale for this electron-phonon coupling is ~1 ps[10,11]. The energy transfer between the two systems increases the lattice temperature while simultaneously cooling the electronic system. As the ionic system heats, if the laser pulse deposited sufficient energy, it may reach its melting point, at which time it undergoes a phase transition to the liquid state. Because the time scale for coupling energy from the electronic system to the ionic lattice is ~1 ps, the melting transition in thermal melting is expected to occur on a timescale of several picoseconds following laser irradiation. Melting by nanosecond lasers, wherein the optical pulse is longer than the characteristic electron-phonon coupling time, is well-described by this thermal melting mechanism[12,13]. A graphic of the relevant timescales for thermal and non-thermal is given in Figure 2.1.

2.2.3 The non-thermal melting mechanism

As was stated, the first steps in both pathways are identical, with the laser pulse first exciting electrons, which subsequently cool to a Fermi-Dirac distribution, while the lattice remains cool. However, in the non-thermal melting case, it is this extreme excitation of the electronic system itself that plays the key role in initiating the phase transition. In a manner analogous to promotion of an electron to an antibonding orbital in a molecule, the extreme degree of electronic excitation into the conduction band of the material results in weakening of the interatomic bonding in the solid lattice[4]. Assuming sufficient electron density is achieved in the conduction band, predicted by to be[9] ca. 10^{22}/ cm ^{3}, the interatomic potential weakens to the point wherein the room temperature thermal motions in the ionic lattice are able to break the bonds inside the material. In such a scenario, the substrate can be predicted to lose structural order on the timescale of molecular vibrations, viz. tens to hundreds of femtoseconds. As this timescale for melting is significantly shorter than the characteristic time for the electron-phonon coupling discussed previously, in the non-thermal pathway melting occurs while the ionic lattice is still relatively cool. This is the origin of the term *non-thermal*, as the phase transition is not driven by increasing the lattice temperature.

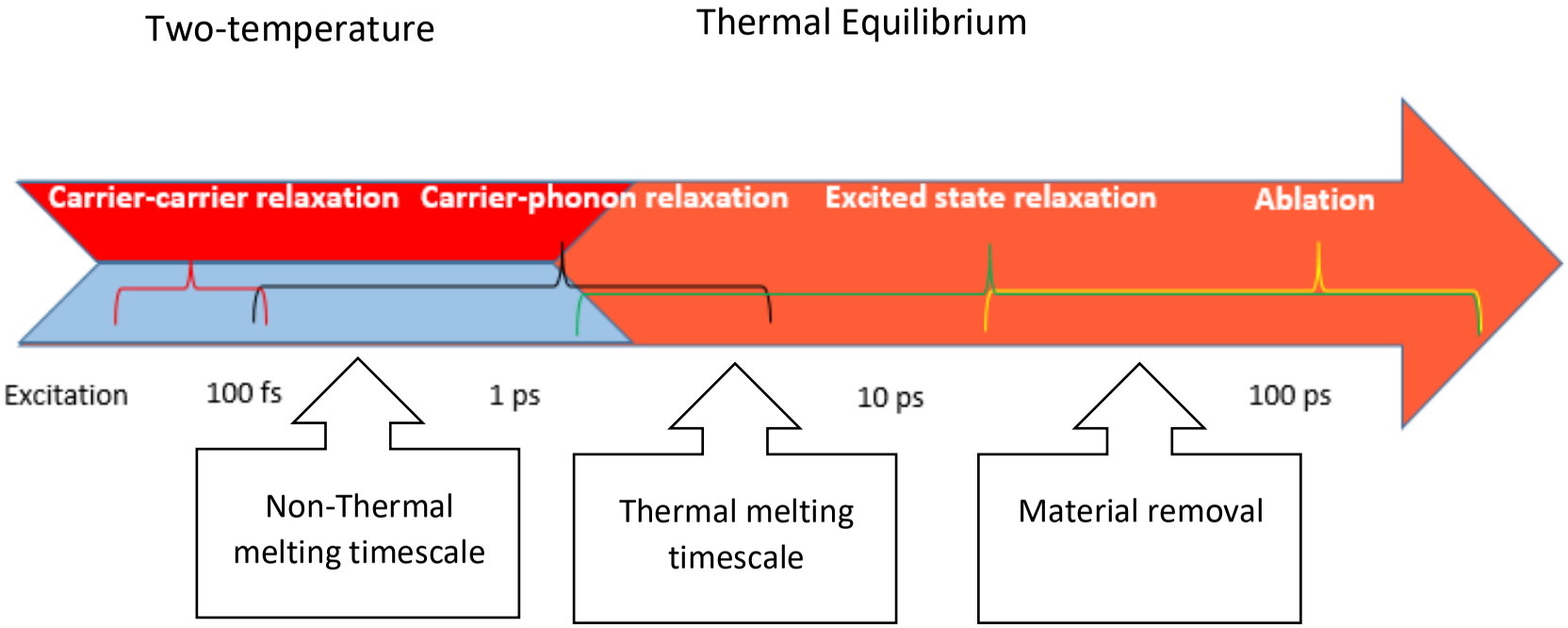

Figure 2.1: Timescales of various processes relevant in ultrafast laser melting and ablation of solid substrates.

In the non-thermal melting mechanism, the physics following the melting transition proceed in a manner very similar to that of the thermal pathway. Energy from the electronic system is coupled into the ionic lattice via the scattering of phonons, bringing the system back to thermal equilibrium[14]. Thus, on picosecond timescales, the properties of fluids produced from both mechanisms are similar, and equilibrium properties of the non-thermally prepared liquid can thus be studied, provided data are taken on picosecond timescales.

2.2.4 Inertial confinement

A critical aspect of the laser preparation of liquid carbon samples is the inertial confinement of the melt. It is from the inertial confinement effect that the ability to control the density, and therefore the structural properties, of the resultant liquid carbon is derived. At picoseconds timescales after laser melting, the liquid is expected to be in a high temperature and pressure state due to the large amount of energy coupled into the system by the melting laser pulse. To relieve the stresses induced by the high temperature and pressure in the melt, the systems launches pressure waves from the surface of the material, including a rarefaction wave that propagates from the material surface into the bulk[15]. On an infinite timescale, this rarefaction wave leads to ablation of the prepared liquid, leaving behind a crater on the sample surface. However, the rarefaction wave launched into the material travels with finite speed in the liquid, ca. ~1000 m/s [16], the speed of sound in the material. As this wave is responsible for material expansion, before the rarefaction wave reaches a given depth in the prepared sample, the density of the liquid remains identical to that of the initial solid. Assuming an optical melting depth of ca. 100 nm, the optical penetration depth in the solid, we can expect the rarefaction wave to reach the back of the melted material in a time of:

$$(100\text{x}10^{-9}\text{ m})/(1000\text{ m/s}) \approx 100\text{ ps}$$

If we therefore carry out our experimental measurement on shorter timescales, the bulk of the melt will have achieved thermal equilibrium, but will remain at or near the initial target density. See Figure 2.2 for an illustration of the expansion dynamics in the liquid.

The expansion of the material can itself be exploited as a tool to access more of the carbon phase diagram. The pressure and temperature of the ablation plume decrease as the liquid expands. By taking a series of measurements at different time points in the expansion, the liquid properties as a function of the thermodynamic state can be mapped out.
As was discussed previously, such measurements of the liquids properties as a function of the temperature, pressure and density are critical for fully understanding the physics of liquid carbon and how the material properties evolve as the liquid structure varies. With the aid of theoretical calculations of the substrates ablation dynamics, we can model the temperature and pressure in the plume and correlate these with the results of experimental measurements. Doing so may help to resolve some of the controversies that impede the understanding of liquid carbon, such as the proposed existence of a liquid-liquid phase transition.

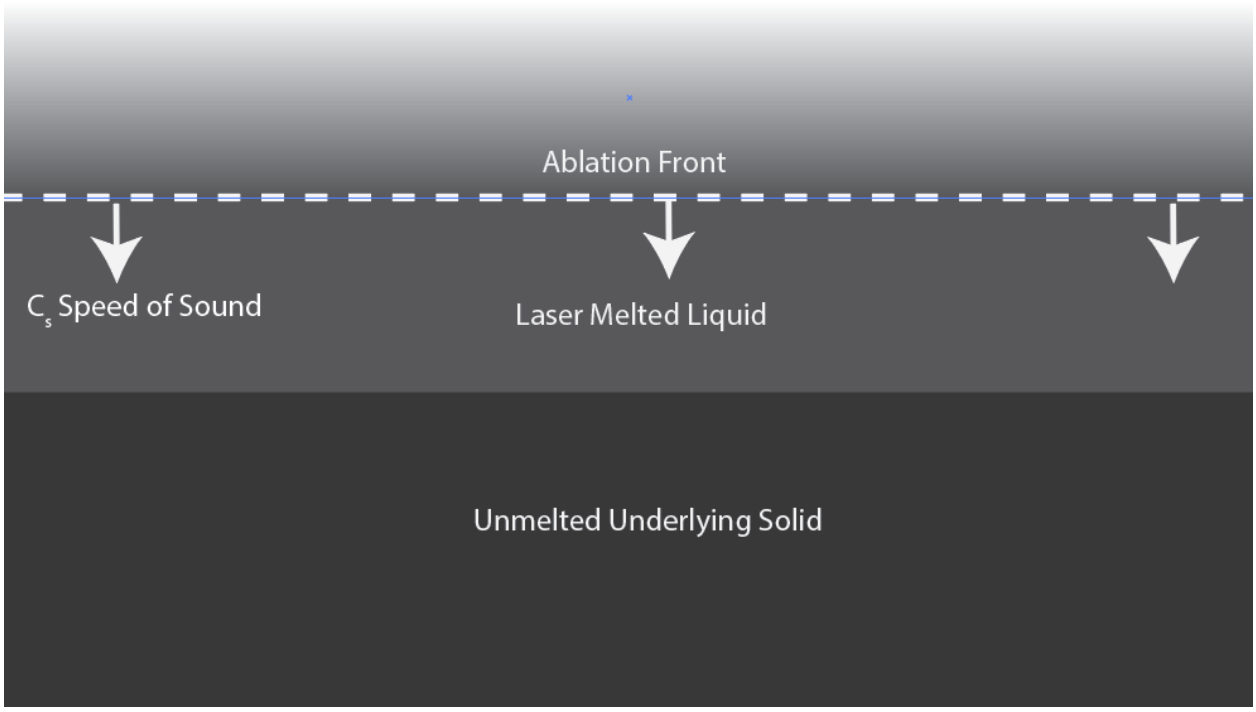

Figure 2.2: Inertial confinement of laser-prepared liquid. Material underneath the ablation front, which moves at the speed of sound in the material, remains at the density of the initial substrate.

One important aspect of the liquid ablation is the maintenance of a sharp interface between the liquid and the ambient medium as the material ablates. As the liquid expands, the melt crosses into the two-phase coexistence regime on the phase diagram. This results in the decomposition of the initially liquid-state ablation plume into a mixture of gas and liquid droplets[14]. A consequence of this transition to the two-phase regime is a sharp decrease in the speed of sound in the material, slowing the plume expansion velocity and resulting in the formation of a sharp and optically smooth interface between the ablation plume and its surroundings[14]. This optically smooth interface is responsible for the phenomenon of the Newton rings seen in the ablation of liquid carbon and other laser melted materials[3,14]. The fact that the ablation plume maintains such a sharp interface is critical for the second harmonic generation experiments we will discuss later, as the technique relies on the existence of a well-defined non-centrosymmetric boundary between media.

2.3 Reflectivity Measurements of Liquid Carbon

For the experimental characterization of liquid carbon, we begin with measurements of the liquid carbon optical reflectivity. These experiments are important as they provide a benchmark for confirming the ability to successfully melt the carbon substrate. In the laser melting of materials like silicon[17,18] and gallium arsenide[3], previous authors have observed a large increase in the optical reflectivity after laser irradiation, which has often been interpreted as a hallmark of the melting transition. Whether carbon, on melting, undergoes an increase or decrease in the optical reflectivity, however, remain controversial[1,2,19,20] as was discussed in the previous chapter. This question is intimately tied to the question of whether the liquid state is a metal or an insulator, as the reflectivity of the sample is interconnected with the material electronic structure. To help resolve this fundamental controversy and to confirm our ability to generate liquid carbon, we carried out a series of optical reflectivity experiments on laser melted graphite.

2.3.1 Experimental design

The experiment used to conduct the reflectivity measurements is diagrammed in Figure 2.3. In our system, 800 nm, 100 fs ultra-fast laser pulses were first generated by a Mai Tai Titanium:sapphire oscillator, operating at a repetition rate of 80 MHz. The pulses from the oscillator were then used to seed the Spitfire chirped pulse regenerative amplifier, which served to increase the per pulse energy by a factor of ~10^6, while the pulse repetition rate was decreased to 1 KHz. After exiting the amplifier, the beam was split with a 55/45 plate beam splitter, with the more intense transmitted beam becoming the melting pulse, while the reflected beam was used as the probe.

The high intensity melting pulse first traveled through a variable time delay stage, with time resolution ~100 fs, and then through a chopper that was phase locked to the Spitfire amplifier, which served to reduce the laser repetition rate to 333 Hz. The reduction in repetition rate was necessary to allow sufficient time for sample translation between laser shots. The melting pulse was then focused normal onto the carbon target surface with a 150 mm focal length lens, producing an on-sample spot diameter of 150 microns. Melting fluence in the experiments was ca. 1 J/cm^2 to ensure total melting of the substrate in the beamspot.

After the beamsplitter, the probe pulse was directed into an optical parametric amplifier (TOPAS), which allowed for the probe to be tuned to the desired wavelength. After exiting the TOPAS, the frequency-shifted probe was directed through a second chopper to reduce the repetition rate to 333 Hz. After the chopper, the probe beam then passed through a motorized rotating neutral density filter, which continuously modulated the power of the probe pulse. The

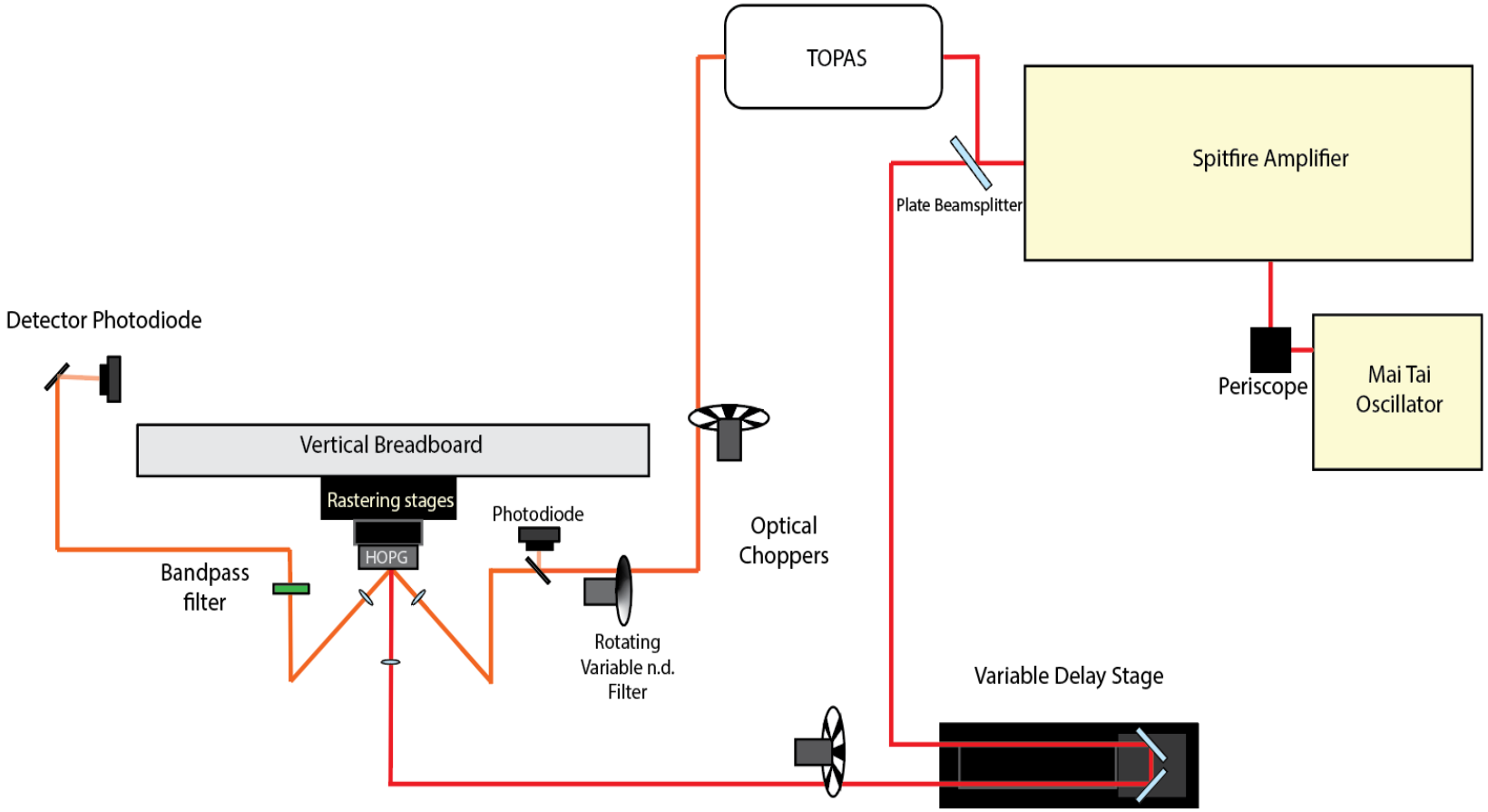

Figure 2.3: Experimental design for the reflectivity experiments

power of each laser pulse after the rotating N.D. filter was then measured using a 1% reflectivity beamsplitter and photodiode. After power measurement, the probe pulse was focused onto the sample surface at a 45^{o} angle relative to the sample normal with a 33mm focal length lens, resulting in an on-sample spot of 70 microns in diameter. The smaller size of the probe spot relative to the melting spot ensured that only regions pumped by the melting pulse were measured when the two spots were overlapped on the sample. The time-zero for temporal overlap of the melt and probe pulses was determined by overlapping the two pulses on a BBO crystal positioned in the same location as the sample and tuning the time delay until the sum frequency of the probe and melt beams was observed.

For the experiments detailed here the chosen carbon substrate was highly oriented pyrolytic graphite (HOPG), supplied by Structure Probe Incorporated supplies. Highly oriented graphite, in which the graphitic planes have a high degree of parallelism, was selected because the samples are large and uniform and because the sample surfaces exhibit low roughness, which ensured good optical reflectivity. Graphite, with a density of 2.2 g/cm^3, was chosen as the sample because it is easily cleaved using Scotch tape, allowing for the laser-damaged topmost layers to be removed after each experiment. Cleaving was measured to remove about ~30 microns of sample each time the surface was refreshed. As the melt depth is ca. 100 nm, cleaving removed enough material to ensure a completely fresh graphite surface for every experiment. The ability to cleave the sample to create a fresh surface was invaluable, as it ensured the substrate did not have to be replaced for every experimental run. The sample itself was mounted on an X,Y computer-controlled translation stage. The stage allowed the carbon target to be rastered during the experiment, ensuring that each pair of melt/probe laser pulses was incident on a pristine sample surface. A tip-tilt stage between the sample and the translation stage ensured that the HOPG sample surface was rigorously parallel to the plane of translation, preventing errors in the alignment due to the rastering.

After impinging on the sample, a second 33 mm focal length lens recollimated the reflected probe pulse. The reflected probe then passed through a bandpass filter to remove any stray light and finally, the intensity of the reflection was measured using a second photodiode. The reflected intensity was analyzed using custom-written LabVIEW software, wherein the input power measurements for the probe pulses were binned and the reflected signal measurements in each bin were averaged. The reflectivity signal was taken to be the slope of the graph of reflected signal intensity vs. input power. Measurement of the signal in this manner allowed for the reflectivity to be accurately measured even in the presence of a constant background.

2.3.2 Determination of the melting threshold

The first step in the characterization of liquid carbon samples was the determination of the graphite melting threshold at the melting wavelength of 800 nm used in the experiments. Previous measurements for the melting threshold at a variety of different wavelength were available from the literature and are detailed in Table 2.1.

Study	Melting wavelength (nm)	Threshold fluence
Downer[1]	632	.13
Malvezzi[2]	532	.14
Cavalleri[7]	620	.10 (fullerite film)
Kudryashov[21]	800	.08

Table 2.1: Melting fluence for graphite as observed in previous studies

As the absorption coefficient of graphite is relatively constant across the visible spectrum, it should be expected that the melting threshold at 800 nm would be similar in magnitude to that measured by other investigators at visible wavelengths. Theoretically, one can predict the melting threshold from the optical constants of the substrate. Previous studies have predicted that that for successful nonthermal melting, an excitation density of ~10^{22}/cm^3 must be achieved in the material conduction band[9]. We can estimate the excitation density in a solid using[17]:

$$N_{e-h} = F_0 \frac{(1-R)}{\hbar\omega}\left[\alpha_0 + \frac{\beta f_0(1-R)}{2\sqrt{\pi}\tau_0}\right] \quad (2.1)$$

Here $N_{e\text{-}h}$ is the electron-hole excitation density, F_0 the applied melting fluence, R is the reflectivity at the melting wavelength, α_0 and β are the linear and two-photon absorption coefficients for graphite, and τ_0 is the pulse duration. Figure 2.4 shows a plot of the predicted excitation density in an HOPG substrate as a function of the exciting laser fluence.

It is observed that assuming a necessary threshold excitation density of 10^{22}/cm^3 tends to underestimate the necessary fluence to achieve melting. For instance, Reitze found an experimental melting threshold for his system of 0.13 J/cm^2 at 632 nm[1]. Inserting the optical constants at this wavelength into the expression, we obtain an electron density ~2.0x10^{23}, about an order of magnitude higher than predicted as necessary for ultrafast melting of a graphite substrate. If we assume that this electron density is the necessary value to initiate nonthermal melting of HOPG, we find the melting threshold for 800 nm to be ~0.16 J/cm^2, a value close to that measured at 632 nm, as expected.

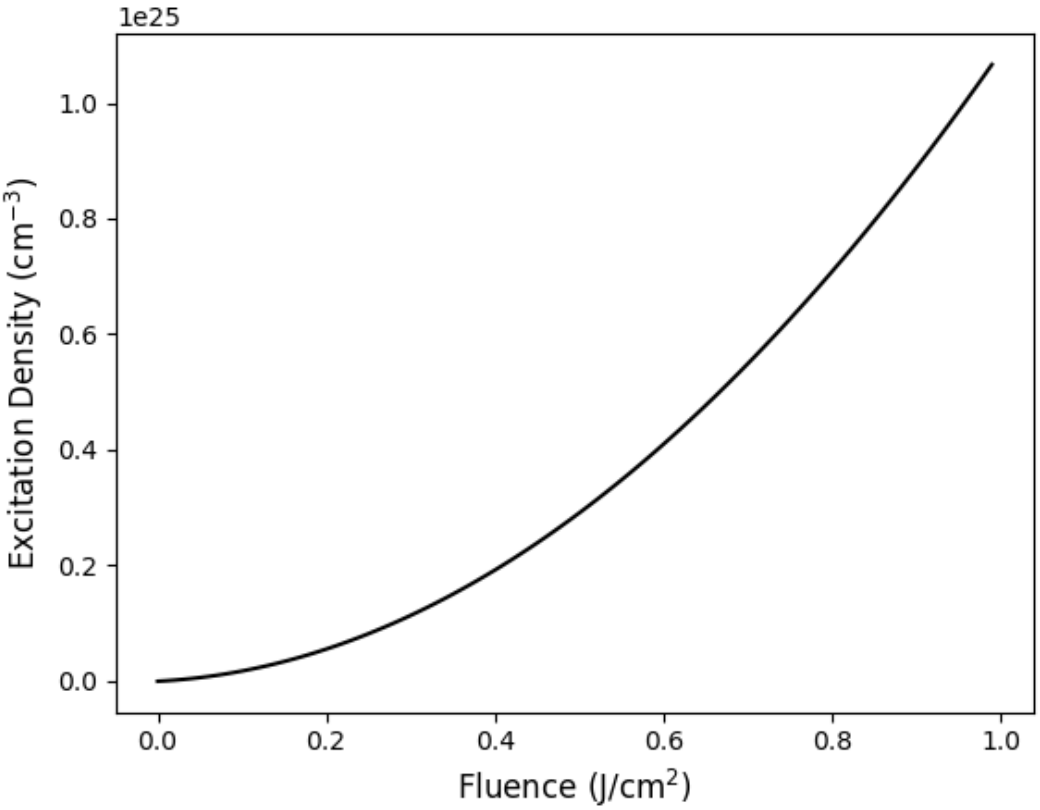

Figure 2.4: Excitation density in HOPG as a function of melting laser fluence at 800 nm, as predicted by Equation 2.1.

Taking this value as a starting point, we set out to experimentally determine the threshold melting fluence necessary to non-thermally melt HOPG graphite targets. The method for determining the threshold, following examples from the literature, was to look for a large and abrupt change in the HOPG reflectivity after interaction with the melting laser pulse. Figure 2.5 shows the 700 nm relative reflectivity as a function of the melting fluence at t=0, defined as when the melting and probe pulses were temporally overlapped on the sample. We chose 700 nm for the probe wavelength to permit spectral discrimination between the reflected probe and scattered light from the melting pulse. In all the melting threshold experiments, care was taken to ensure the probe pulse fluence was kept below 0.05 J/cm^2 to prevent potential melting of the sample with the probe. The reflected intensity of the laser-irradiated carbon at each fluence is normalized to that of the pristine HOPG surface without melting pulse irradiation.

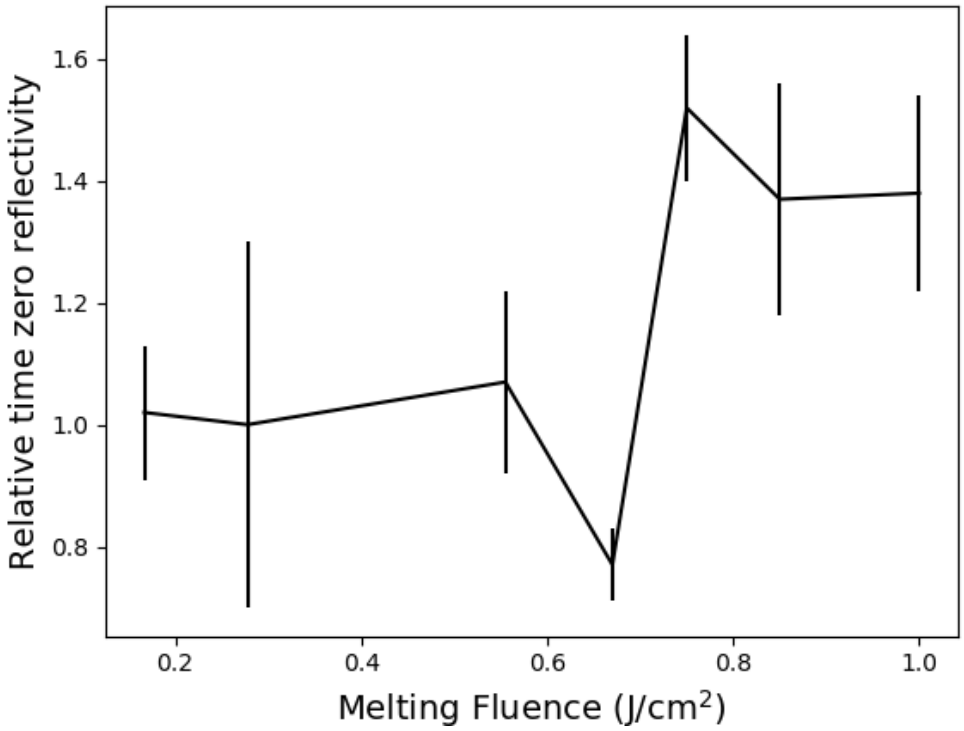

Figure 2.5: t=0 reflectivity as a function of melting fluence. The large increase in reflectivity seen for fluences above .75 J/cm^2 is a result of ultrafast melting of the HOPG target.

Experiments at fluences below 0.6 J/cm^2 showed no evidence for melting of the substrate. Instead, the reflectivity remains unchanged until a fluence of about 0.67 J/cm^2. At this input fluence, a small decrease in the reflectivity can be observed after laser irradiation. This decrease is a result of the generation of an intense electron-hole plasma by the melting pulse, and has been seen before by other investigators of non-thermal melting[1]. This dip is usually observed to occur just below the threshold for non-thermal melting. The most notable observation is the massive increase in the sample reflectivity observed at when the melting fluence exceeds .75 J/cm^2. As this threshold is crossed, the system demonstrates an instantaneous 50% increase in the reflectivity, as is further illustrated in Figure 2.6. Following the examples of past studies which used reflectivity as a probe for liquid formation, we take this value to be the melting threshold for the HOPG target. The measured value is significantly higher than predicted by the earlier estimate based on the excitation density. It is also higher than that measured previously by any investigator, as can be seen in Table 2.1. The study most relevant to our measurement is that of Kudryashov, who employed ellipsometry measurements on a laser-excited graphite target. For an incident fluence of 0.08 J/cm^2 he observed an increase in the in-plane reflectivity for HOPG targets, which was interpreted

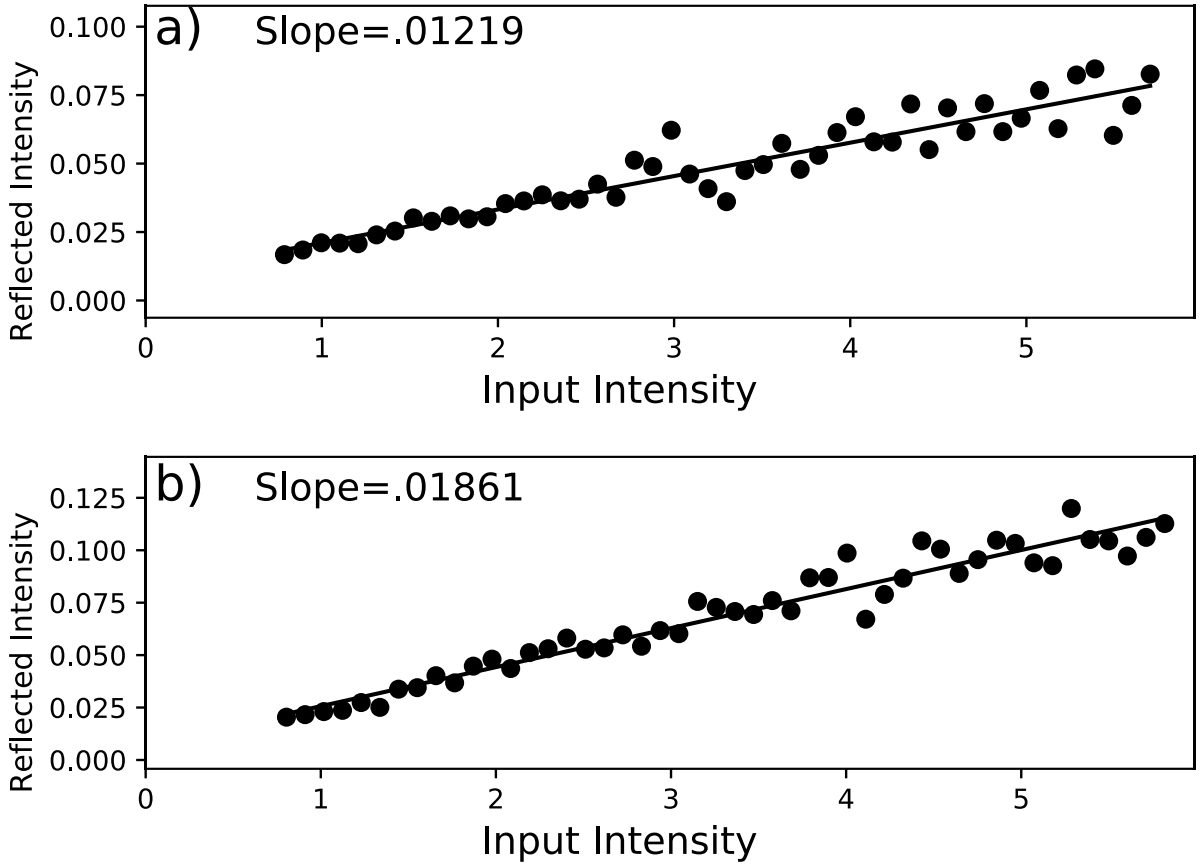

Figure 2.6: Plot of reflected signal vs. input intensity for **a)** unmelted graphite and **b)** laser melted graphite at t=0 for a melting fluence of .75 J/cm^2. The reflectivity increases by 50% when the melting pulse is allowed to impinge in the target.

as a transition from the 2-dimensional HOPG to a 3-D carbon material without pronounced structural anisotropy. Our measured melting threshold is approximately an order of magnitude higher than that measured by Kudryashov for the initiation of this structural change. Kudryashov's study, however, didn't specify whether his observed change in reflectivity was explicitly a result of laser melting and therefore, the changes observed by Kudryashov at a fluence of 0.08 J/cm^2 may have been a result of other structural changes. Even so, our measured threshold is significantly higher than any other threshold measured in other studies of the laser melting of graphite. At present, it is not fully understood why such an intense pulse is necessary to initiate melting in HOPG at 800 nm.

Post-mortem analysis of the HOPG substrates also confirmed successful melting of the HOPG target for fluences above .75 J/cm^2. Figure 2.7 shows a confocal microscope image of the target after laser irradiation at 1 J/cm^2 for the melting pulse. In the image, two damage points

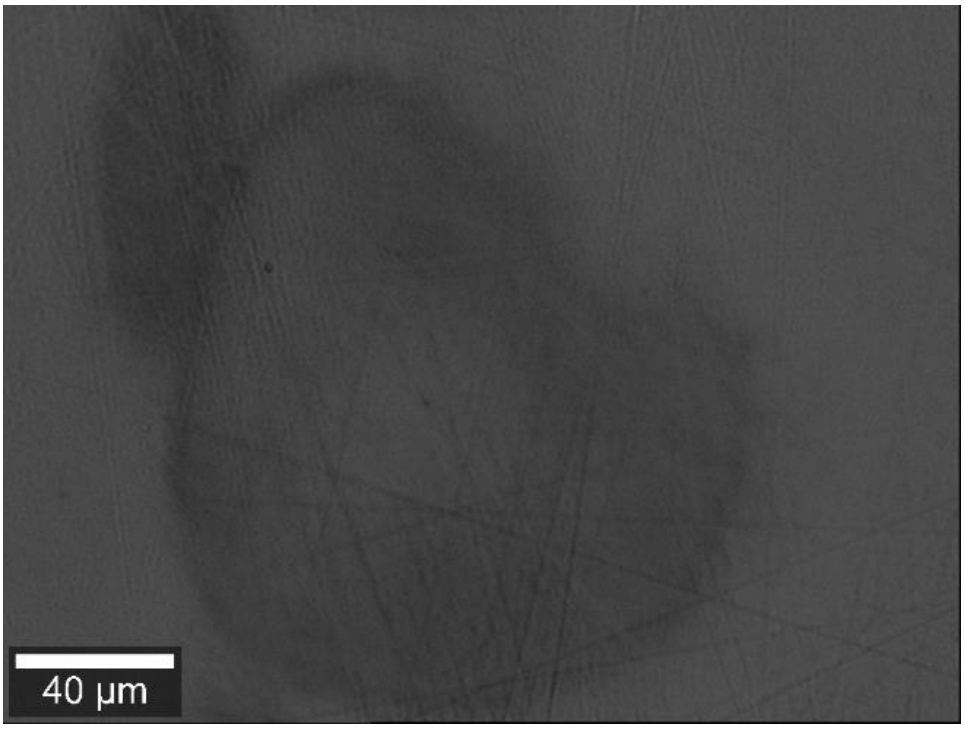

Figure 2.7: Post-mortem microscope images of the melting and probe pulse craters. The fact that the melting pulse craters are observed to be well-separated implies the sample is rastered at a speed sufficient to prevent hitting the same spot twice with the laser. The oblong spot is a result of the probe pulse. As evident in the image, the probe spot is significantly smaller than the melting spot.

are clearly seen. The larger one, with a diameter of about 150 µm, is a result of the melting pulse. The second smaller spot is from the probe beam, which was intentionally increased in power so that the probe spot size relative to the melting spot could be assessed. Only one melting pulse crater is apparent in the image, well-separated from its neighbors. From this, we can be confident that there was sufficient time between laser shots to properly translate the sample during the experiment. This is critical, as hitting the same spot twice would result in significant reflectivity losses due to scattering from the residual ablation crater. From both the change in the system reflectivity and the presence of the leftover ablation crater, we can be reasonably confident that for fluencies above 0.75 J/cm^2 we are successfully driving the graphite into the liquid state.

2.3.3 Time-dependent reflectivity

Having determined the threshold necessary to initiate melting, the dynamics of the reflectivity as a function of time after irradiation were then measured. The main image in Figure 2.8 shows the sample reflectivity for the first 10 ps after melting with an ultrafast laser pulse with melting fluence of 1 J/cm^2. The line in the main figure is simply intended as a guide for the eye. As evident in the data, following the instantaneous reflectivity increase, the reflectivity of the sample undergoes an exponential decay. The inset of Figure 2.8 shows the natural logarithm of the reflectivity as a function of time. From best fit line of this plot, we extract a decay time of ~22 ps for the reflectivity of laser excited HOPG. This pattern of instantaneous reflectivity increase followed by exponential decay is very similar to that observed by Reitze in his experiments on the laser melting of HOPG at 632 nm.

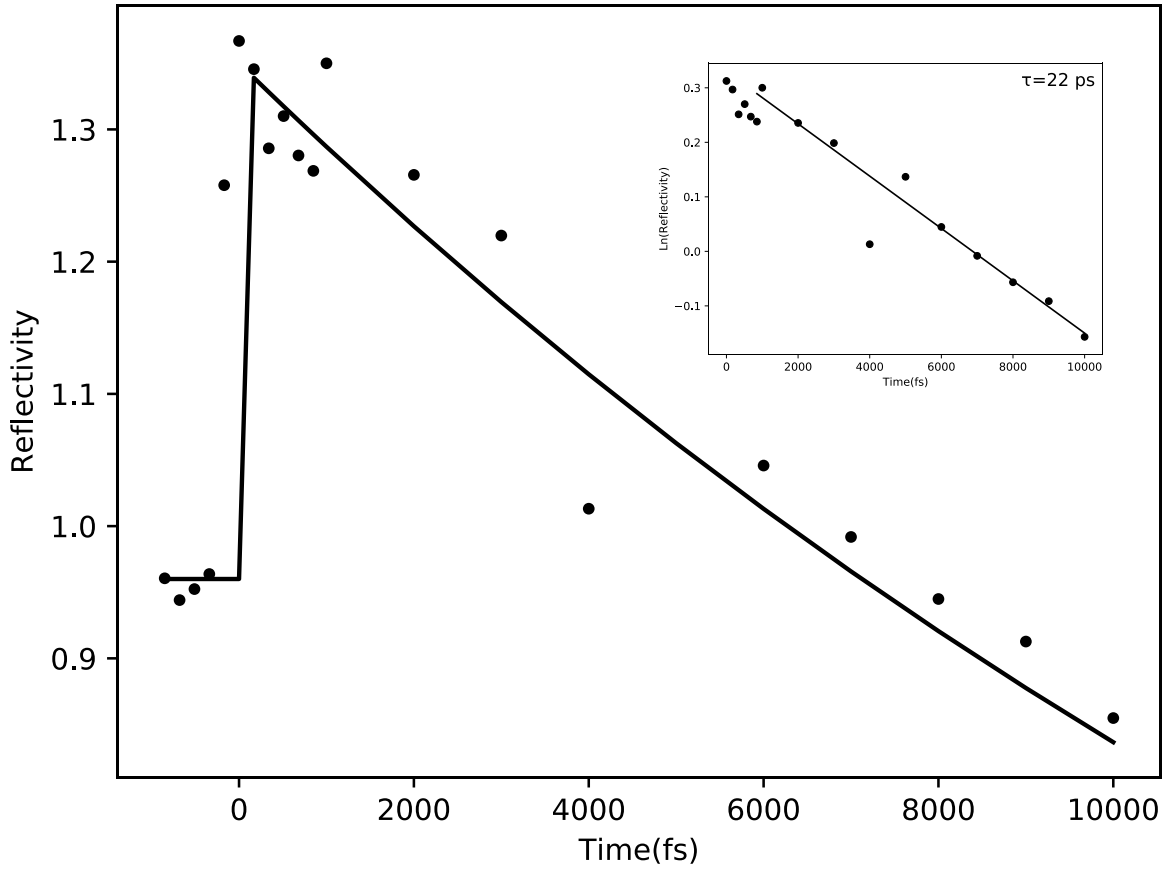

Figure 2.8: Time-dependent reflectivity of laser-melted HOPG. After the initial increase, the sample reflectivity undergoes an exponential decay. The line is a guide for the eye.

Inset: natural log of the reflectivity vs. time, which yields a decay time constant of 22 ps.

The measured 22 ps timescale for the reflectivity decay also compares favorably with that measured in Reitze's study, where the initial increase in reflectivity was noted to decay with a time constant of ~20-30 ps for melting fluencies in the range of 1 J/cm^2. As in his experiment, we attribute the near instantaneous rise in the reflectivity to the transition from solid graphite to a liquid metal. This argument can be justified through the application of a simple Drude model. The motion of electrons in the presence of a driving electric field can be written as:

$$E_0 e^{-i\omega_i t} = \frac{\partial^2 x}{\partial t^2} + \frac{m}{\tau}\frac{\partial x}{\partial t} \qquad (2.2)$$

Here $E_0 e^{-i\omega_i t}$ is the driving electric field, m is the electron mass, and the second term on the right-hand side of Equation 2.2 describes frictional forces with damping time τ. With the oscillatory electric field of frequency ω_1 as the driving force term, we can assume the electronic motion of a single electron to also be sinusoidal and write it as:

$$\vec{v} = \overrightarrow{v_0} e^{-i\omega_i t} \qquad (2.3)$$

Here $\overrightarrow{v_0}$ is the electron drift velocity. The motion for the entire electric cloud is described by the current density in the system, which can be written as:

$$\overrightarrow{J_w} = -ne\vec{v} = \sigma E \qquad (2.4)$$

Here n is the total number of electrons and e is the elementary charge. Combining Equations 2.3 and 2.4 with Equation 2.2, an expression for the A.C. conductivity of the material can be derived:

$$\sigma_\omega = \frac{\tau N e^2}{m(1+i\tau\omega_i)} \qquad (2.5)$$

Finally, we can use the relationship between the conductivity and the dielectric constant to write the complex dielectric of the material:

$$\widetilde{\varepsilon_w} = \varepsilon(\infty) - \frac{\omega_p^2}{-\omega^2 + i\omega\Gamma_d} \qquad (2.6)$$

Here ε(∞) is the dielectric at infinite frequency, taken to be ~ 1, Γ_d is 1/τ and we have introduced the plasma frequency defined as:

$$\omega_p = \sqrt{\frac{Ne^2}{m\varepsilon_0}} \qquad (2.7)$$

The interpretation of this expression for the dielectric constant of a metal is straightforward. The real part of the dielectric is related to the reflectivity and can be written as:

$$\varepsilon_r = \varepsilon(\infty) - \frac{\omega_p^2}{\omega^2 - \Gamma^2} \approx 1 - \frac{\omega_p^2}{\omega^2 - \Gamma^2} \qquad (2.8)$$

For probe frequencies below the plasma frequency, we should expect the real part of the dielectric to become large and negative, resulting in total reflection at these wavelengths. For most metals, the electron density is ~10^{22}/cm^3, with the corresponding plasma frequency being in the UV. As such, we see large reflectivity at visible wavelengths in metals. The fact that we see a large increase in the reflectivity akin to that observed by Reitze in his experiments is strong evidence for liquid carbon having metallic character. The results of our study into liquid carbon reflectivity, along with many others performed at visible wavelengths, all seems to indicate that liquid carbon is metallic in nature, at least at densities near 2 g/cm^3.

In conclusion, based on the results of our reflectivity measurements on an HOPG target after laser irradiation, we are confident in our ability to prepare carbon in its liquid state using an ultrafast laser. Our measured threshold melting fluence of 0.75 J/cm^2 is significantly higher than that measured in previous experiments, which, given how little the absorption constant for graphite changes a crossed the visible spectrum, is difficult to explain. Nonetheless, we find the characteristic reflectivity increase seen by previous investigators, which has historically been taken as an indicator of success in driving the substrate into the liquid state. Our measured timescales for both the reflectivity increase and its subsequent exponential decay are in line with those measured by previous investigators, adding further evidence we have successfully generated liquid carbon. The results of these reflectivity experiments are interpreted as further evidence for liquid carbon being metallic, at least at graphitic densities. To measure the properties of the liquid at lower density will require finding or synthesizing a sample of the desired density with an optically smooth surface, and is something we will investigate further in the future. Given that studies carried out by other investigators showed similar behavior for the reflectivity at both higher[1] and lower[7] densities, however, there aren't expected to be significant differences in the reflectivity behavior or in the dynamics as a function of substrate density.

2.4 Second Harmonic Generation Spectroscopy Experiments on Liquid Carbon

2.4.1 Introduction

Having confirmed the ability to generate liquid carbon via laser melting, focus now turns towards making spectroscopic measurements of the surface properties of the liquid. The interface of liquid carbon is of special interest due to implications from previous studies that it may play a key role in the nucleation of nanomaterials, such as nanotubes and Q-carbon[22,23]. The liquid carbon surface is also fundamentally interesting because it represents a unique coordination environment. As previously noted, there exists a strong relationship between the structure of liquid carbon and its density. Near the interface, carbon atoms are expected to be undercoordinated. One can therefore speculate that the bonding and resultant properties may be drastically different at the surface, as compared to the bulk, with perhaps a higher degree of sp and sp^2 bonding and associated changes in conductivity. These structural differences may have additional interesting implications for the nucleation of materials from the liquid. To investigate these possibilities, we attempted to carry out measurements of the surface properties of liquid carbon using second harmonic generation (SHG) spectroscopy.

2.4.2 Second harmonic generation

To study the structure of the liquid surface requires a tool that can discriminate between those carbon atoms near the interface and the far more numerous carbon atoms which make up the bulk of the liquid. One of the best probes for interfacial phenomena is second order non-linear spectroscopy, one type of which is second harmonic generation.

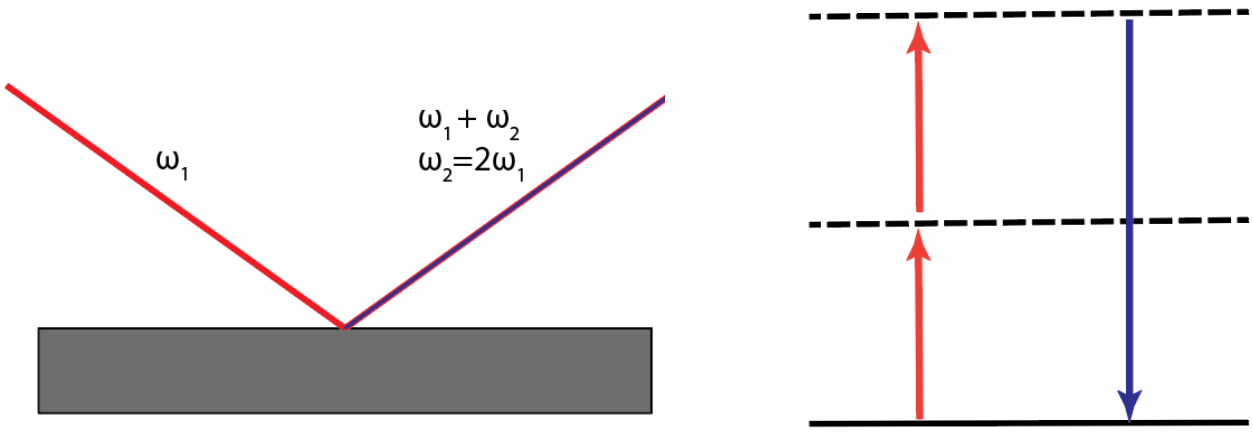

Figure 2.9: Schematic and state diagram for the SHG process. In SHG two input photons are combined into a single output photon at twice the energy

In this process, two photons incident on the sample at frequency ω_1 are combined into a single outgoing photon at ω_2, where ω_2 is twice the input frequency:

$$\omega_2=2*\omega_1 \qquad (2.9)$$

A schematic and state diagram for this SHG process is shown in Figure 2.9. The origin of this phenomenon can be understood by considering the polarization of the material and noting that the common linear expression is only a first-order approximation of the actual polarization response, valid only at low intensities. Going beyond this first-order assumption, we can expand the polarization as follows:

$$P(t) \propto \chi^{(1)}E(t) + \chi^{(2)} E(t)E(t)+ \chi^{(3)} E(t)E(t)E(t)+ \ldots \qquad (2.10)$$

Here $\chi^{(n)}$ is the n^{th} order hyperpolarizability coefficient and E(t) is the incident, time-dependent electric field. The magnitude of each $\chi^{(n)}$ term decreases with increasing order, which implies that strong field, like those from ultrafast lasers, are required to detect the nonlinear effects. In the case of second harmonic generation, the term of interest is the second-order term, with hyperpolarizability $\chi^{(2)}$. As evident in Equation 2.10, the second-order term is proportional to the square of the input electric field. As a result, this term has contributions at twice the frequency of the input field, as well as a zero-frequency term (optical rectification), which can be shown as follows:

$$E(t) = e^{i\omega_1 t} + e^{-i\omega_1 t} \qquad (2.11)$$

$$|E(t)|^2 = e^{i2\omega_1 t} + e^{-i2\omega_1 t} + 2E(0) \qquad (2.12)$$

Here E(0) is the zero frequency contribution. $\chi^{(2)}$ itself is a second rank tensor with 27 elements, $\chi^{(2)}_{ijk}$, although the number of independent elements can be greatly reduced by the symmetry of the surface. Under the electric dipole approximation this second-order hyperpolarizability contribution $\chi^{(2)}$ and all other even-order polarizability terms in Equation 2.10 can be shown to vanish in a centrosymmetric medium, such as the bulk of a liquid in the dipole approximation. Starting from the second-order polarization term

$$\mathrm{P} = \chi^{(2)}_{i,j,k}\mathrm{E(t)E(t)}\,, \qquad (2.13)$$

we invert in a centrosymmetric medium to yield

$$-P = \chi^{(2)}_{-i,-j,-k} E(t)E(t) = \chi^{(2)}_{ijk} E(t)E(t) , \qquad (2.14)$$

where we have exploited the fact that, in a centrosymmetric medium, the optical properties of opposing directions must be equivalent. Therefore, we find

$$P = -P = 0 , \qquad (2.15)$$

for all input electric fields. Therefore, $\chi^{(2)}$ must necessarily vanish for a centrosymmetric medium. Physically, this results from cancellation of dipoles, with oppositely oriented moieties oscillating 180^o out-of-phase with one another, leading to complete cancellation of the outgoing field. Near the interface between two media, however, the centrosymmetry is broken. All SHG intensity measurements in the experiment are derived specifically from this non-centrosymmetric interfacial region. The expression for the magnitude of the χ^2 tensor itself can be written as:

$$\chi^2 \propto \frac{A}{(\omega_t - \omega_E - i\Gamma)(\omega_t - 2\omega_E - i\Gamma)} \qquad (2.16)$$

Here A is the proportionality constant, related to transition diploes in the medium, ω_t is a transition in the sample, ω_E is the input electric frequency and Γ is the state lifetime. From Equation 2.16, it can be seen that second harmonic generation exhibits resonant enhancement when either the fundamental or the second harmonic are resonant with a transition in the material. Exploiting this resonant enhancement indicates that a surface spectrum for liquid carbon can be measured by tuning the input frequency of the probe laser and monitoring the corresponding intensity of the SHG response. This spectrum, coupled with knowledge from previous carbon cluster studies and simulations, will permit characterization of the carbon bonding structure at the outermost layers of the fluid. Assuming an optically flat surface maintained as the liquid carbon ablates, we can also measure the surface spectrum as a function of delay time after melting, allowing for the analysis of the liquid properties as the material cools and expands. In this way, we might also gain insights into the earliest steps in the nucleation of materials like nanotubes or even Q-carbon

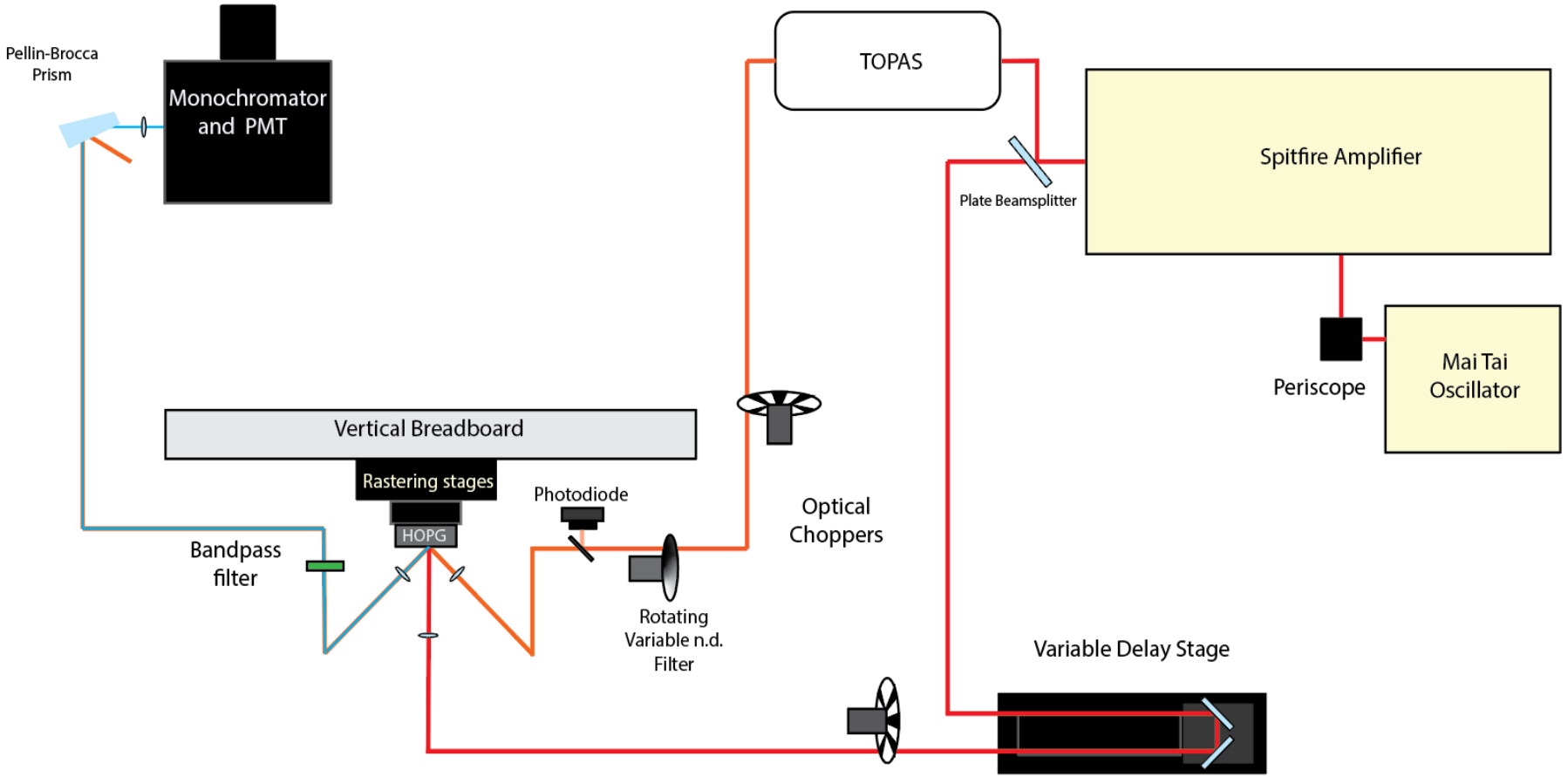

Figure 2.10: Experimental design used in the second harmonic generation experiments

2.4.3 Experimental design

The experimental configuration used for the SHG measurements is shown in Figure 2.10. This design is nearly identical to that used for the measurements of the liquid carbon optical reflectivity. The output from the amplifier was again split into separate melting and probe pulses, 800 nm and 700 nm respectively, which are focused onto out carbon sample with a relative delay set by the time delay stage in the melting pulse line. The main changes for the SHG measurement are in the detection scheme for the second harmonic photons. After reflection from the laser irradiated HOPG target and recollimation of the input beam by the post-sample lens, the SHG photons are traveling co-linearly with the remaining input fundamental. To spectrally separate the desired second harmonic signal from the unwanted fundamental field, the beam was first directed through a bandpass filter centered at 350 nm, which removed most of the residual 700 nm fundamental. After the bandpass filter, the second harmonic light was further separated from any remaining fundamental via transmission through a Pellin-Broca prism, which rotated the travel direction of the second harmonic photons by exactly 90°, while the fundamental was deviated by a smaller angle and directed into a beam dump. After separating out the desired signal, the SHG photons were focused into a monochromator and photomultiplier tube, where the intensity of the second harmonic light was measured. As with the reflectivity data, the data analysis was handled via custom Python software. The signal intensity at a given timepoint was determined by plotting the intensity of the SHG as a function of the input intensity squared and taking the slope, which is proportional to $\chi^{(2)}$. For more details of the signal processing in the second harmonic experiments see Appendix A.

The samples used in the second harmonic generation experiments were the same HOPG substrates as used in the previously described reflectivity studies. A second set of experiments on graphitic films of density near 1 g/cm^3 was attempted, but the surface proved to be too rough to obtain satisfactory specular reflection from those samples.

2.4.4 Second harmonic generation from liquid carbon

Figure 2.11 shows a plot of the second harmonic intensity vs. the square of the input laser power for the pristine, unmelted graphite surface. The signal-to-noise ratio is only moderate, a consequence of the imperfections in the alignment as the sample is rastered, but the overall linearity is good. As SHG is second-order process, the intensity of the second harmonic is dependent on the square of the input intensity:

$$I_{SHG} \propto \left|\chi^{(2)}\right|^2 I_{fund}^2 \qquad (2.17)$$

Here I_{fund} is the intensity of the input fundamental. From Equation 2.1,7 it can be seen that the intensity of the second harmonic should be linear in the square of the input intensity. The linearity of the SHG response apparent in Figure 2.11 is evidence that the observed signal intensity does indeed originate from a second-order process, as opposed to some other effect.

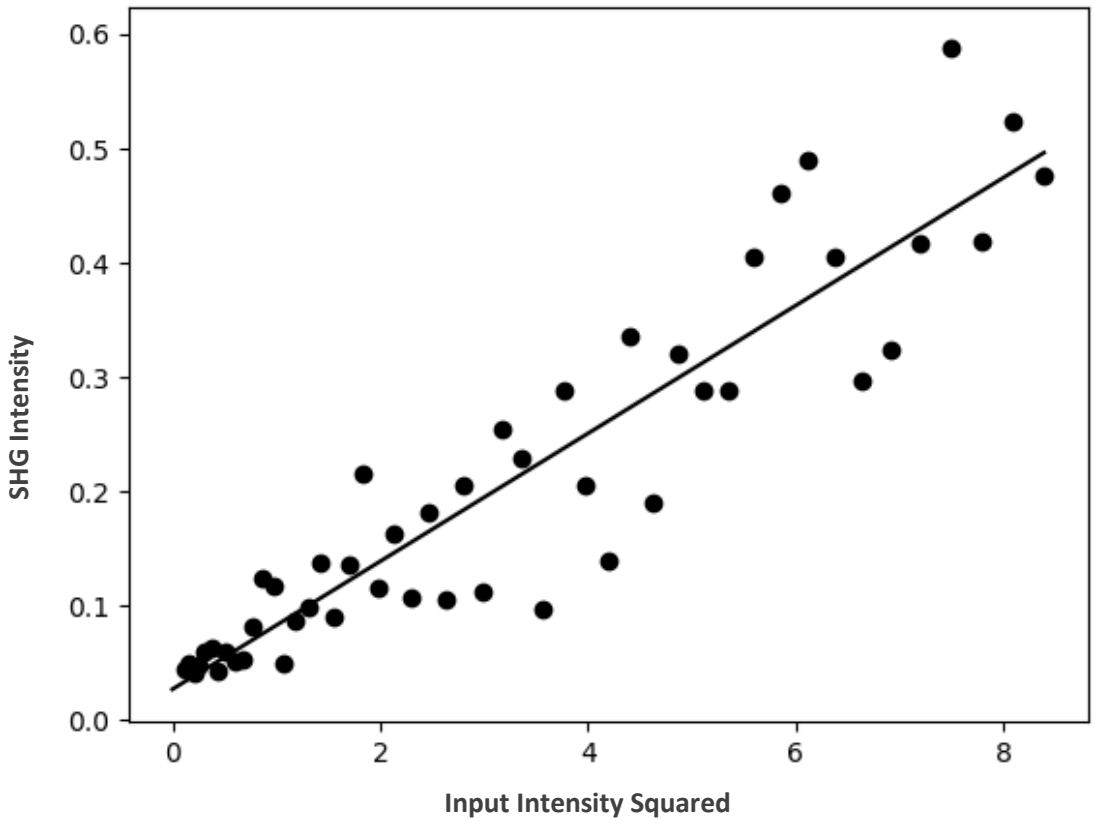

Figure 2.11: Second harmonic signal for pristine unmelted graphite. As expected for a second order process, the intensity is linear in the square of the input power

When the melting pulse was unblocked and both melt and probe pulses were allowed to simultaneously reach the sample surface, a large increase in the measured signal was observed. At first, it was hoped that this increase resulted from the transition to the liquid metal state, but it was quickly discovered that he same increase in intensity was observed even when the probe pulse was blocked and only the melting pulse was allowed to reach the sample. Furthermore, as evident in Fig 1.12, the plot of the signal vs. input intensity squared was flat and exhibited a low signal-to-noise ratio. The data comprise a largely random scatter, with the lack of linearity being a clear sign that the observed photons were the results of some unwanted contribution originating from the melting pulse itself. The presence of an unwanted background had been noted during the reflectivity experiments, but in that case, the reflected signal was strong enough that the background did not obviate the measurement. The SHG signal intensity, however, is many orders of magnitude weaker than the intensity of the reflected fundamental and, as such, the melting pulse background was significantly more problematic. The high intensity of the background obscured the SHG signal generated from liquid carbon, rendering it very difficult to detect. Accurate measurement of the second harmonic signal from the liquid after melting required that the origin of this unwanted background from the melting pulse be identified and removed.

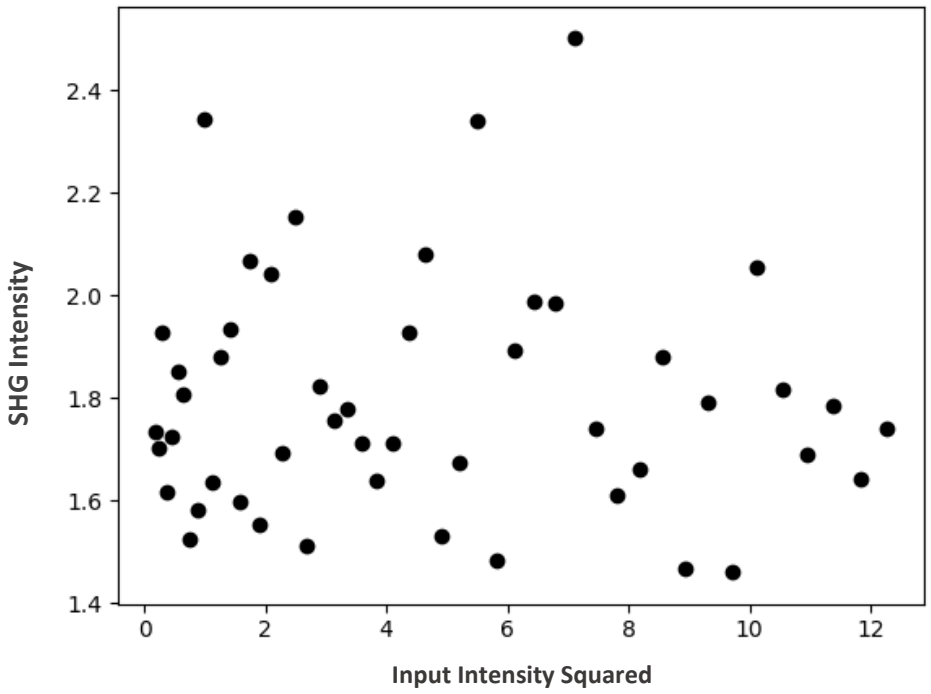

Figure 2.12: Second harmonic generation plot for the laser-melted HOPG at t=0. The lack of linearity indicate that the observed photons are not a result of a second- order optical process

The possibility that the background in the experiments was the result of scattered light from the melting pulse was ruled out by the addition of the bandpass filter after the sample. The melting pulse, centered at 800 nm, should have minimal transmission through the filter. However, the intensity of the background was found to remain unchanged after the filter was added to the beam path. With the possibility of scattered laser light ruled out, a second likely origin for the background from the melting pulse was blackbody radiation from the irradiated sample. Blackbody radiation is the temperature-dependent, spectrally broad emission radiated by heated objects. The intensity dependence for blackbody radiation at a selected frequency is given by the following expression:

$$I(v) = \frac{2hv^3}{c^2}\frac{1}{1 - e^{\frac{hv}{kT}}} \qquad (2.17)$$

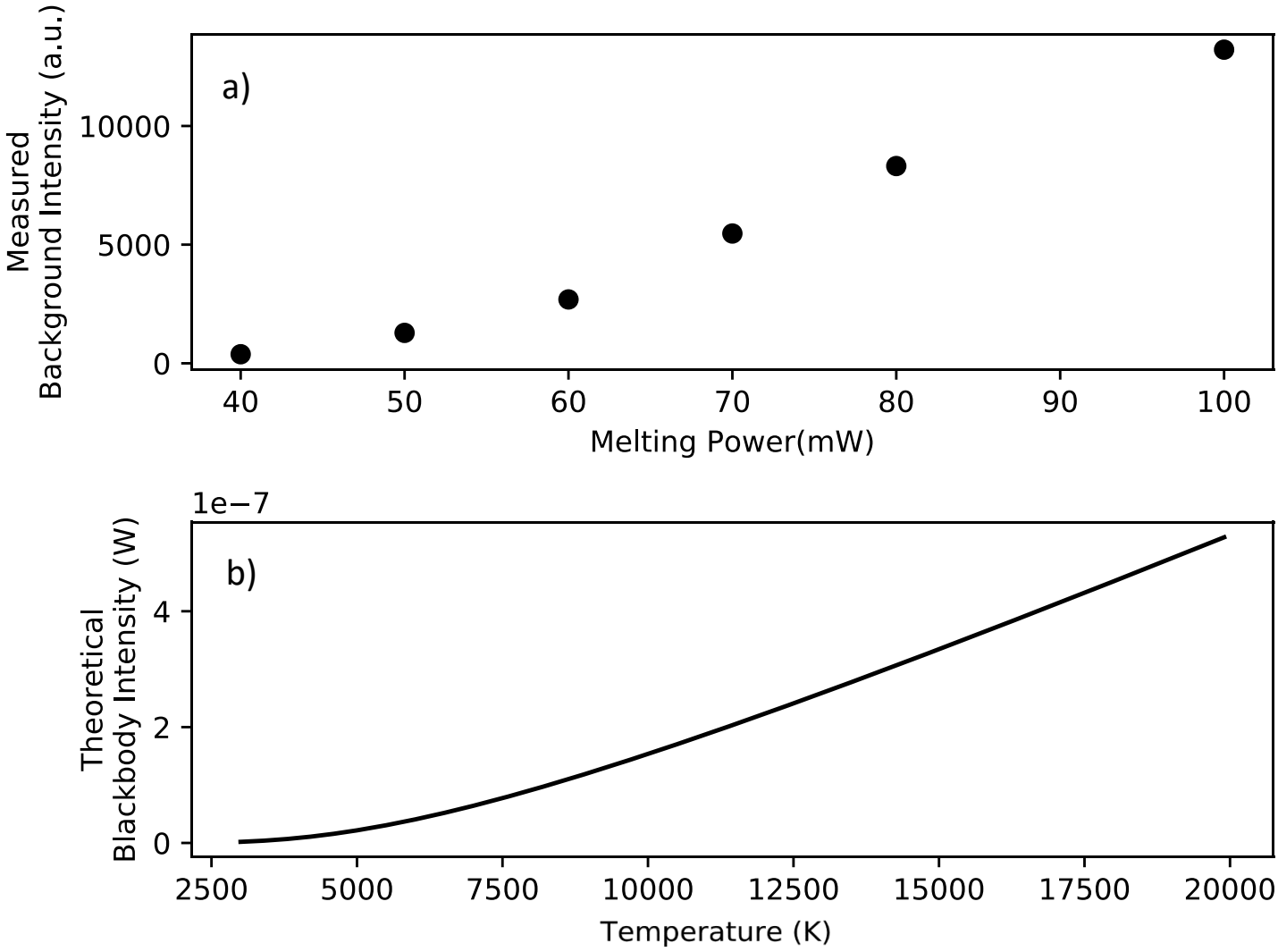

Figure 2.13: a) Background from the melting pulse as a function of melting laser fluence. **b)** Blackbody intensity as a function of temperature as predicted by Equation 2.17. The similar shape for the two curves provides evidence that the observed background does result from blackbody radiation

Here I(v) is the blackbody intensity at frequency v, h is Planck's constant, k is the Boltzmann constant and T is the system temperature. Based on the results of previous studies, immediately after melting the liquid reaches temperatures between 10000 and 12000 K[19,24]. At these temperatures, significant blackbody radiation in the visible would be expected from the graphite substrate. As this radiation is incoherent, some small portion of this blackbody emission was collimated by the post-sample collection optics and was thus reaching the detector. To investigate this, the intensity of the background radiation was measured as a function of the melting power, which is directly related to the temperature after melting. Fig 2.13a shows these data, while Fig 2.13b plots the predicted blackbody intensity as a function of the substrate temperature, as predicted by Equation 2.17. As is apparent in the figure, the shape of the background intensity curve is a good match with the expected temperature dependence of blackbody radiation. This provides further evidence for the melting pulse background being a result of blackbody radiation due to the high temperature reached by the liquid carbon. As can be seen from Equation 2.17, the intensity of the radiation at a given temperature is highly wavelength dependent. It was hoped that carrying out the SHG measurement at shorter wavelengths would therefore result in a reduced background. To test this hypothesis, the probe wavelength was decreased from 700 nm to 400 nm, with the second harmonic at 200 nm in the deep UV. While indeed the blackbody background was reduced at 200 nm, unwanted photons from the pump pulse continued to be a problem and the weak second harmonic signal at 200 nm was still being overwhelmed by unwanted blackbody intensity. Attempts to further reduce the incoherent background through measure such as adding additional irises to the beam path were also found to be ineffective in reducing the intensity of the background.

Despite the unwanted contributions from the blackbody background, the time dependence of the measured SHG was studied for a probe wavelength of 700 nm. It was hoped that at later time points following melting, a combination of sample cooling and increased second harmonic intensity as a result of transition to the liquid metal phase might result in the second harmonic signal becoming dominant over the blackbody background. Metals, like gold, are often used as standards in sum frequency generation experiments, as they are known to have a strong second harmonic response. Figure 2.14 shows the time dependent second harmonic generation intensity after the melting pulse. As evident in the figure, the measured intensity was highly inconsistent and exhibits no real changes as a function of melt-probe delay. Analysis of the intensity vs. squared input power plots clearly showed that the measured signal was still dominated by contributions from the blackbody background at all measured timepoints in the experiment. From the analysis, it is clear that any changes in the second harmonic intensity emanating from transitions to the liquid state are not large enough to overcome the intense blackbody background.

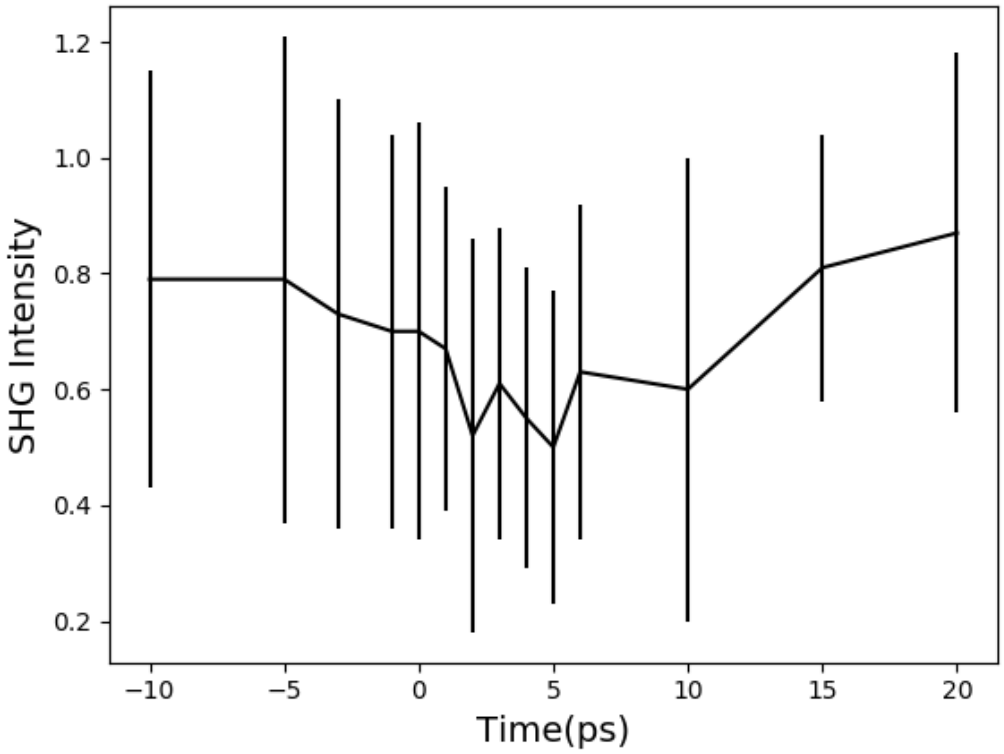

Figure 2.14: Second harmonic intensity as a function of delay time after melting with 1 J/cm^2. The data is dominated at all time points by the blackbody background, which results in the large observed uncertainties.

While a *decrease* in the second harmonic signal as a result of the melting transition can't be ruled out, due to the poor signal to noise, we clearly do not see a large *increase* in the SHG signal derived from the generation of liquid carbon. Given the known large second order response from metals like gold, the fact a large increase in the SHG signal following melting is not observed makes it tempting to question whether or not the liquid is metallic. We can evaluate the validity of this argument by considering the relative SHG response expected from a metal compared to the measured blackbody intensity. Even the metals with the highest SHG responses only generate SHG signal intensities about an order of magnitude higher than that of a semiconductor, like silicon[25,26]. The baseline SHG intensity from unmelted graphite, being a zero-bandgap semimetal, is probably expected to lie somewhere in between that of a typical semiconductor and that of a metal. Considering the level of signal observed from the pristine un-melted graphite, even if the melting transition resulted in the SHG intensity increasing by an order of magnitude, the resulting SHG response would still be masked by the noise derived from the blackbody background. As such, it is premature to draw any conclusions regarding the electronic nature of the liquid from the results of this SHG study.

Conclusions

Efforts to measure the surface spectrum of liquid carbon were complicated by the intense blackbody radiation resulting from the high surface temperature after laser melting. This intense background served to mask the desired second harmonic signal. Attempts to mitigate the intensity of the background by changing the probe wavelength and time delay between melt and probe did little to improve the signal-to-background, making meaningful measurement of the second harmonic nearly impossible. While attempts to obtain a surface spectrum of the liquid carbon were unsuccessful, it is still believed that the liquid is metallic based on the results of reflectivity measurements and the knowledge that even a modest increase in SHG intensity from the liquid would have been lost in the overwhelming blackbody background. Due to the high temperature of the substrate after melting, measurements on liquid carbon by optical spectroscopy methods require techniques with either very large signals (reflectivity) or that use wavelengths much shorter than those in the visible background. While second-order nonlinear optical spectroscopy in the UV-visible proved problematic as a technique for analyzing the surface properties of liquid carbon, in the future, techniques like XPS or the newly emergent soft x-ray second harmonic generation[27] may prove more successful for analyzing the interface of the melt.

References:

1. Reitze, D. H., Ahn, H. & Downer, M. C. Optical properties of liquid carbon measured by femtosecond spectroscopy. *Phys. Rev. B* **45**, 2677 (1992).

2. Malvezzi, A. M., Bloembergen, N. & Huang, C. Y. Time-Resolved Picosecond Optical Measurements of Laser-Excited Grayhite. *Phys. Rev Lett.* **57**, 146 (1986).

3. Cavalleri, A., Sokolowski-Tinten, K., Bialkowski, J., Schreiner, M. & Von der Linde, D. Femtosecond melting and ablation of semiconductors studied with time of flight mass spectroscopy. *J. Appl. Phys.* **85**, 3301 (1999).

4. Sokolowski-Tinten, K., Bialkowski, J. & Von Der Linde, D. Ultrafast laser-induced order-disorder transitions in semiconductors. *Phys. Rev.* **8**, 14186 (1995).

5. Saeta, P., Wang, J.-K., Siegal, Y., Bloembergen, N. & Mazur, E. Ultrafast Electronic Disordering during Femtosecond Laser Melting of GaAs. *Phys. Rev Lett.* **67**, 1023 (1991).

6. Von der Linde, D., Sokolowski-Tinten, K. & Bialkowski, J. Laser–solid interaction in the femtosecond time regime. *Appl. Surf. Sci.* **109**, 1 (1997).

7. Cavalleri, K. Sokolowski-Tinten, D. Von der Linde, I. Spagnolatti, M. Bernasconi, G. Benedek, A. P. and P. M. Generation of the low-density liquid phase of carbon by non-thermal melting of fullerite Related content Modelling ultrafast laser ablation. *Europhys. Lett.* **57**, 281 (2002).

8. Sokolowski-Tinten, K., Bialkowski, J., Boing, M., Cavalleri, A. & Von Der Linde, D. Thermal

and nonthermal melting of gallium arsenide after femtosecond laser excitation. *Phys. Rev. B* **58**, 11805

9. Van Vechten, J. A., Tsu, R. & Saris, F. W. Nonthermal pulsed laser annealing of Si; plasma annealing. *Phys. Lett. A* **74**, 422 (1979).

10. Ferrari, A. C. Raman spectroscopy of graphene and graphite: Disorder, electron-phonon coupling, doping and nonadiabatic effects. *Solid State Commun.* **143**, 47 (2007).

11. Jiang, J., Saito, R., Grüneis, A., Dresselhaus, G. & Dresselhaus, M. S. Electron–phonon interaction and relaxation time in graphite. *Chem. Phys. Lett.* **392**, 383 (2004).

12. Sundaram, S. K. & Mazur, E. Inducing and probing non-thermal transitions in semiconductors using femtosecond laser pulses. *Nat. Mater.* **1**, 217 (2002).

13. Sokolowski-Tinten, K. & Von Der Linde, D. Generation of dense electron-hole plasmas in silicon. *Phys. Rev. B* **61**, 2643 (2000).

14. Sokolowski-Tinten, K. *et al.* Transient States of Matter during Short Pulse Laser Ablation. *Phys. Rev. Lett.* **81**, 224 (1998).

15. Kudryashov, S. I. *et al.* Femtosecond laser ablation of carbon: From spallation to formation of hot critical plasma. *AIP Conf. Proc.* **1464**, 244 (2012).

16. Johnson, S. L. *et al.* Bonding in Liquid Carbon Studied by Time-Resolved X-Ray Absorption Spectroscopy. *Phys. Rev. Lett.* **94**, 57407 (2005).

17. Sokolowski-Tinten, K. & Von der Linde, D. Generation of dense electron-hole plasmas in silicon. *Phys. Rev. B* **61**, 2643 (2000).

18. Shank, C. V, Yen, R. & Hirlimann, C. Time-Resolved Reflectivity Measurements of Femtosecond-Optical-Pulse-Induced Phase Transitions in Silicon. *Phys. Rev. Lett.* **50**, 454 (1983).

19. Reitze, D. H., Wang, X., Ahn, H. & Downer, M. C. Femtosecond laser melting of graphite. *Phys. Rev. B* **40**, 986 (1989).

20. Malvezzi, A. M. & Romanoni, M. The Optical Properties of Graphite Under Intense Picosecond Laser Illumination t. *Int. J. Thermophys.* **13**, 131 (1992).

21. Kudryashov, S. I. & Emel'yanov, V. I. Nonthermal structural transformation in quasi-monocrystalline graphite during 100-fs laser pulse. *J. Exp. Theor. Phys. Lett.* **73**, 487 (2001).

22. De Heer, W. A. *et al.* Liquid carbon, carbon-glass beads, and the crystallization of carbon nanotubes. *Science (80-.).* **307**, 907 (2005).

23. Narayan, J. & Bhaumik, A. Novel phase of carbon, ferromagnetism, and conversion into diamond. *J. Appl. Phys* **118**, 215303 (2015).

24. Mincigrucci, R. *et al.* Transient EUV Reflectivity Measurements of Carbon upon Ultrafast

Laser Heating. *Photonics* **4**, 23 (2017).

25. Boyd, G. T., Rasing, T., R Leite, J. R. & Shen, Y. R. Local-field enhancement on rough surfaces of metals, semimetals, and semiconductors with the use of optical second-harmonic generation. *Phys. Rev. B* **30**, 519 (1984).

26. Che, F., Grabtchak, S., Whelan, W. M., Ponomarenko, S. A. & Cada, M. Relative SHG measurements of metal thin films: Gold, silver, aluminum, cobalt, chromium, germanium, nickel, antimony, titanium, titanium nitride, tungsten, zinc, silicon and indium tin oxide. *Results Phys.* **7**, 593 (2017).

27. Lam, R. K. *et al.* Soft X-Ray Second Harmonic Generation as an Interfacial Probe Elettra-Sincrotrone Trieste. *Phys. Rev. Lett.* **120**, 23901 (2018).

Chapter 3

X-Ray Scattering from Liquid Silicon

Text of this chapter submitted to Chemical Physical Letters as Early Time Dynamics of Laser-Ablated Silicon Using Ultrafast Grazing Incidence X-ray Scattering

3.1 Introduction

Structure and structural evolution of laser prepared liquids are becoming increasingly critical areas of research, owing to growing evidence that liquid intermediate states exist in the laser synthesis of nanomaterials like carbon nanotubes. X-ray scattering techniques are powerful tools for structural determination in condensed media, however their application to the study of laser prepared liquids has been limited due to the poor time resolution available from most x-ray sources. As a result, few studies have utilized x-ray techniques for the study of laser melted solids. However, a newly emerged tool in the form of the free electron laser presents the opportunity for a more complete elucidation of the structure of the non-thermally melted liquids. By utilizing the ultrafast femtosecond x-ray pulses available from free electron lasers, experiments to characterize the structure of both the liquid and the resultant ablation plume become possible. The results of such experiments allow for direct observation of the evolution of the liquid structure with unprecedented temporal resolution.

3.2 Free Electron Lasers

Tunable x-ray sources have become a crucial tool in x-ray science, allowing for the study of structure, chemistry and composition in a wide variety of materials. Third generation synchrotron sources are the most commonly used and widely available x-ray sources, with user facilities built worldwide. At these facilities wide range of x-ray experiments can be performed viz, scattering[1], imaging[2], absorption and emission spectroscopies[3,4]. Despite this flexibility, synchrotrons are not without their limits. Major drawbacks for these synchrotron sources include low brilliance and poor time resolution of ca. 50-100 picoseconds. Due to these limitations, synchrotron sources are ill suited for carrying out experiments that require high x-ray power or that require high time resolution. To remedy these issues a new class of tunable x-ray sources has recently emerged. The free electron laser (FEL) couples a linear accelerator with a long undulator to produce x-ray pulses with significantly higher power than is available from synchrotron sources. The x-ray pulse duration for these free electron laser sources of ca. 10 fs are also several orders of magnitude shorter than those available from synchrotrons. As such, these new sources have quickly become invaluable tools in ultrafast x-ray science.

3.2.1 Physics of free electron lasers

The very high power and short pulse durations available from free electron lasers are a consequence of the physics through which the FEL radiation is generated. To generate photons in a free electron laser, first an electron beam is accelerated to relativistic speed via a linear accelerator. Once the electrons in the beam have attained kinetic energies of ca. 5-10 gigaelectronvolts, the electron beam is ejected from the accelerator into the long FEL undulator,

where alternating poled magnets generate a strong periodic magnetic field. This magnetic field in the undulator region exerts a periodically alternating Lorentz force on the relativistic electrons, forcing the electrons in the beam to oscillate. The sinusoidal acceleration of these undulating electrons results in the emission of electromagnetic radiation, with the frequency of the emitted light dependent on the undulator period as follows:

$$\lambda_r = \frac{\lambda_u}{2\gamma^2}\left(1 + \frac{K^2}{2}\right) \qquad (3.1)$$

Here λ_r is the FEL output wavelength, λ_u is the undulator period, and K is the dimensionless strength parameter given by:

$$K = \frac{eB_o\lambda_u}{2\pi m_e c} \qquad (3.2)$$

In Equation 3.2 B_0 is the field strength, e is the elementary charge and m_e is the mass of an electron. In Equation 3.1 γ is the relativistic factor given by:

$$\frac{1}{\sqrt{1 - \frac{v^2}{c^2}}} \qquad (3.3)$$

Here v is the electron velocity after exiting the accelerator and c is the speed of light. The relativist speed of the electrons results in the undulator appearing to have a compressed undulator period as observed by the electron beam. This apparent compression allows for electromagnetic radiation from the electrons in the undulator all the way out into the hard x-ray region of the electromagnetic spectrum. The frequency output from free electron lasers is highly tunable, by controlling the beam energy the FEL is capable of generating photons with frequencies from microwave radiation all the way to the x-ray regime.

The high power of FEL emission, relative to that from other sources such as synchrotrons, results from *coherent* radiation from the electron beam in the FEL undulator. The photons emitted from the electron beam due to oscillation in the undulator are initially *incoherent*, with each electron in the beam emitting radiation with a random phase. As a result of this incoherence, total laser intensity near the start of the undulator scales as n, the number of electrons in the beam, similar to the emission scaling from a synchrotron source. However, as the electron beam traverses the undulator, the electron begin to increasingly emit their radiation

coherently due to the effects of *self-amplified spontaneous emission* (SASE). In SASE the electrons in the beam interact with electric field of previously emitted light, gaining or losing energy due to the columbic force exerted by the net electric field in the undulator. This self-interaction with the undulator radiation has the effect of ordering the electrons, stacking the electron beam into microbunches, separated by the emission radiation wavelength. When bunched in this manner, the electrons now begin to oscillate more in phase, with the radiation intensity now scaling superlinearly. The stronger resultant electric field serves to more tightly bunch the electrons and further increase the coherence of the emitted electromagnetic field. This self-amplification process, akin to the gain inside a visible wavelength lasing medium, results in exponential growth in the output x-ray power intensity up until the system achieves saturation. The total x-ray radiation intensity from the free electron laser at the end of the undulator scales as N^2, resulting in significantly higher brilliance than can be achieved from synchrotron sources.

FELs can also offer pulse duration that are significantly improved over what is available from 3rd generation synchrotrons. Through compression of the electron bunches in the accelerator FEL pulses can be as shorts as 10's of femtosecond[5]. This makes XFELs invaluable for use in experiments where high time resolution is critical. However, the pulses generated by the SASE process in FELs tend to have poor temporal coherence, as a result of the noisy fluctuation which seed the SASE process. Improved temporal coherence can be achieved by instead seeding the XFEL with an external optical pulse, a method employed in some free electron lasers[6,7]. However, the lack of temporal coherence is not a problem for many commonly performed x-ray experiments, and such seeding processes are required only in certain experiments like x-ray non-linear optics that require the x-ray pulses be temporally coherent[8].

Free electron lasers are critical complements to synchrotron sources in x-ray science. While 3rd generation synchrotrons have the benefit of reliability and the capability of high experimental throughput, FEL's allow for experiments that require higher x-ray power or temporal resolution than is available from synchrotrons. These capabilities enable x-ray experiments at FELs that would be impossible to carry out using traditional x-ray sources. Due to the emerging importance of FELs in x-ray science, construction of new FEL experimental facilities is taking place worldwide, initiating a new era of ultrafast x-ray science.

3.3 X-Ray Scattering

X-ray scattering has become an essential tool in studying the structure of solids, liquids, proteins and other nanomaterials. Due to the short wavelength of x-rays, they are sensitive to variations in electron density on length scales on the order of bond lengths, allowing their use as a probe of the structural arrangement of atoms that make up condensed phase materials. From a simple perspective, the relationship between-ray scattering patterns and material structure can be understood through simple Bragg diffraction laws:

$$\sin\theta = \frac{n\lambda}{2d} \qquad (3.4)$$

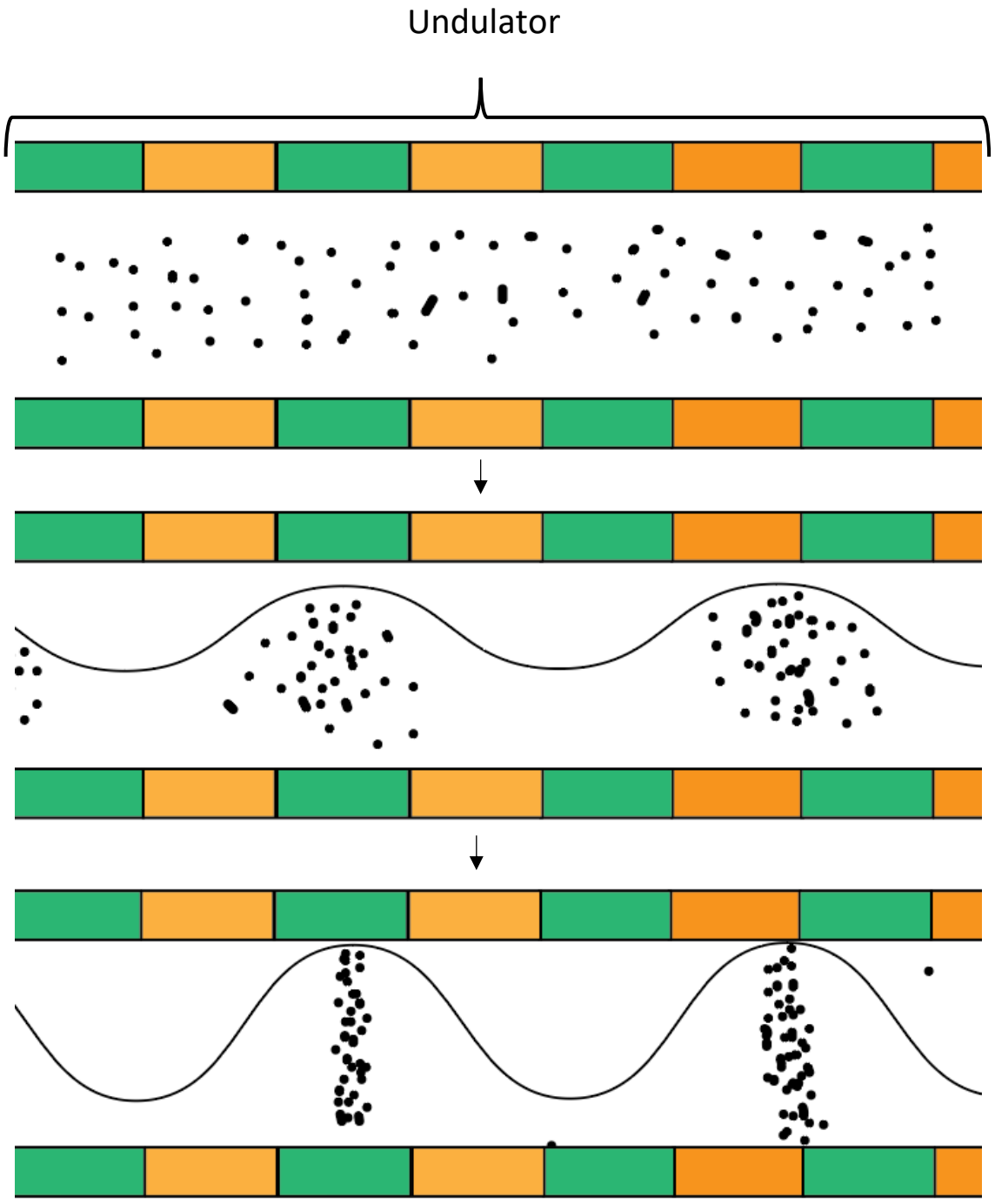

Figure 3.1: Self amplified spontaneous emission process. The interaction between the electrons (dots) on the emitted electromagnetic wave (solid lines) leads to microbunching of the electrons. This serves to amplify the emitted fields, which through the SASE feedback mechanism, results in tighter bunching in the electron beam

Here λ is the x-ray wavelength and d is the distance between planes in the medium. In the case of scattering from crystalline solids, d corresponds to distances between atomic lattice planes in the crystal. For a well-ordered crystal the x-ray scattering pattern takes the form of a series of diffraction spots. From the pattern formed by the resultant diffraction spots, the crystal structure of the material can be deciphered.

For amorphous materials like glasses or liquids there are no well-defined atomic planes, and the scattering pattern does not take the form of diffraction spots as are seen from crystalline materials. Nonetheless, analysis by x-ray diffraction can still yield structural information about even amorphous solids and liquids. In this case, the information encoded in the scattering pattern instead describes the average arrangement of the atoms that make up the material. For a disordered system like a liquid or nanoparticle suspension, an expression for the scattering intensity as a function of angle can be written as follows:

$$I(q) = \langle N \rangle F(q)^2 \left[1 - \frac{1}{v_1}\int (1-P(r))\frac{Sin(qr)}{qr} 4\pi r^2 \delta r\right] \quad (3.5)$$

Here N is the average number density of scatterers, F(q) is the form factor for a single scatterer as a function of the scattering vector. The scattering vector q is defined as:

$$q = \frac{4\pi \sin(\theta)}{\lambda} \quad (3.6)$$

Here θ is the scattering angle and λ is the wavelength of the x-ray radiation. The scattering vector is inversely related to the size of the scattering object[9]. Larger objects exhibit scattering at lower q values, with nanoparticles often being analyzed at scattering vectors below .1 $Å^{-1}$. From the scattering in this region details about particle size and morphology can be obtained by fitting of the resultant x-ray scattering pattern. This approach is often used to characterize nanostructures and proteins in solution.

For the scattering intensity from amorphous materials as described by Equation 3.5, the first term represents independent scattering from all particles in the sample, while the second term describes interference effects between waves scattered by different particles. It is this second term that contains the desired information regarding the structure of the material. Focusing on this second term, we can rewrite it as the product of two terms:

$$I(q) = P(q)\, S(q) \quad (3.7)$$

Here P(q) is the form factor which describes independent scattering from each particle, while S(q) is the structure factor and describes the arrangement of particles in space. In the case of an atomic liquid, the form factor is simply the angle dependent scattering cross section for the atom in question, the value of which can be found in the literature. The structure factor, which describes the average arrangements of the atoms in the liquid, is the Fourier transform of the radial distribution function of the liquid. As a result, measurement of the angle dependent scattering intensity allows for the extraction of the liquid structure factor, from which details of the structure of amorphous materials to be determined.

3.4 X-Ray Scattering from Liquid Silicon

In this section we describe grazing incidence x-ray scattering experiments on liquid silicon ablation plume after melting with an 800 nm 100 fs laser pulse. Liquid silicon was chosen over liquid carbon as the sample due to its structural simplicity, with tetrahedral coordination rather than liquid carbons mixture of different coordination sites. As such, it was hoped might prove to be a good model system for testing the viability of employing ultrafast x-ray scattering to study the nucleation of nanomaterials in the post-irradiation ablation plume. As we will discuss in the next section there is a growing interest in understanding and controlling the nucleation of nanostructures that takes place in the interior of these ablation plume as it expands and cools.

3.4.1 Justification

The behavior of solids following ultrafast laser irradiation have garnered considerable attention, driven by the growing interest in using ultrafast lasers as tools for synthesis and manipulation of electronic materials. Materials of both scientific and economic interest can be synthesized via laser irradiation, including nanoparticles[10–12], thin films[13], and carbon nanotubes and Fullerenes[14–16]. Laser-based methods are attractive in the production of such materials as they are fast, compatible with a wide variety of different material , and, unlike other synthesis methods, usually do not require multistep reactions or extensive purification steps[17] to achieve the desired product. A major impediment for pulsed laser synthesis, however, is the difficulty in producing uniform products with selective control over the final morphology, phase and composition. For example, gold nanoparticles synthesized using the “pulsed laser ablation in water” approach display a much higher degree of poly-dispersity than do particles manufactured using more traditional wet chemistry techniques. This makes them undesirable for uses wherein control over the size is critical[18]. To facilitate the use of laser synthesis in the large-scale manufacture of the materials, a more detailed understanding of the entire process of ablation and material condensation is necessary[19]. The ablation process itself is complex, with multiple modes of material removal, including fragmentation, vaporization, explosive boiling, and spallation[19–21]. Both the structure of the plume and its thermodynamic pathways are directly related to the properties of the initial substrate[19,22], the power of the incident laser radiation[23], and the environment in which the synthesis is performed, such as a vacuum or a liquid[16]. The composition of the ablation plume is similarly complex, made up of multiple species, including monomers and ions, small clusters and large liquid droplets, all emitted with different time and

velocity scales. Understanding the interaction among these different constituents is critical to controlling the final product morphology.

The key to resolving these unknowns lies in attaining a better understanding of the post-ablation physics via direct experimental characterization. Observation of the earliest steps in the formation has proven to be a challenge however, as the short length- and time-scales of the process make the experiments difficult[24]. The melted material initially has a thickness only on the order of the optical depth of the material (less than 100 nm), requiring measurement techniques with high surface specificity. Furthermore, the time scale for condensation is also relatively short, ~50 ps in vacuum. Few techniques have the combined spatial and temporal resolution necessary to directly observe the sub-nanosecond dynamics of the melt and resultant ablation plume. Optical absorption has been a popular tool in imaging and spectroscopy of ablation plumes [25–27]. By measuring the emission or absorption spectra of the plume, the components comprising it can be identified. Rough velocity measurements of the plume constituents can also be obtained by imaging only small slices of the plasma at different distances from the substrate as a function of time. Due to the nanosecond measurement timescales and millimeter spatial resolution achieved in such experiments, however, they often provide only limited insight into the actual formation mechanism of the observed particles. Time of flight mass spectrometry has also been utilized to characterize the composition of the plasma plume[28,29] and can provide more detailed measurements of the velocities of the various plume constituents as well as the cluster sizes in the plasma. This technique is limited by poor time resolution and cannot be used to measure dynamics of cluster formation or growth. In both techniques, the details of nanomaterial nucleation and growth can only be indirectly inferred.

X ray diffraction is well-suited to carrying out direct characterization of the clusters in the plume and has been used in the past to study nanoparticle formation following laser ablation of gold targets with a nanosecond laser[30]. Based on the small angle scattering pattern observed, the formation of both primary nanoparticles (8-10 nm diameter) and secondary nanoparticles with average diameters of 45 nm were reported. However, the scattering measurements in that experiment were only taken at a time point of ~100 μs after laser irradiation long after the initial particle formation. Observation of the initial particle formation using modern synchrotron sources would be precluded as these light sources have pulse durations on the order of tens of picoseconds. Tabletop X-ray sources can achieve the desired femtosecond time resolution but lack the necessary photon flux.

In this study, we sought to observe the earliest dynamics in the femtosecond ablation of silicon by time-resolved grazing incidence X-ray scattering measurements with an X-ray free electron laser. The femtosecond pulses available from the XFEL also have the requisite time resolution and intensity to directly observe the earliest stages of the ablation process. We overcome the penetration depth mismatch problem by carrying out the measurement in a total external reflection grazing incidence geometry. By doing so, we limit the penetration depth of the x-ray pulse to the uppermost few nm of the laser irradiated sample, allowing direct observation of only the ablation plume and the formation of particles on a timescale previously unavailable to x-ray scattering.

3.4.2 Experimental design

Figure 3.2 shows a schematic of the set-up used in the scattering experiments. Experiments were carried out at the Beamline 3[31,32] of the SACLA (SPring-8 Angstrom Compact Free Electron LAser) XFEL[33] at the SPring-8 facility. Figure 1 shows a schematic of the experimental set-up. The 1 mm thick silicon wafers used as samples in the experiment were mounted on a diffractometer stage with XYZ translation capability. X-ray pulses (10 fs, 10 keV) from SACLA were impinged on the sample silicon's (100) face at a 0.1° incident angle, well below the calculated critical angle of 0.17°, ensuring total external reflection of the x-ray beam. For the 10 keV x-ray used in the experiment we estimate our penetration depth to only be 4-6 nm into the sample[34]. The diameter of the incident x ray beam was 2 um, which spread to a final on-sample footprint of ~1 mm length. The shallow angle of incidence also introduced ~1 ps of temporal smearing.

Ablation of the silicon target was carried out using a Ti:Sapphire laser (λ = 800 nm, τ = 40 fs, F = 1.0 J/cm^2). The laser pulses were focused onto the sample at a 70° angle relative to surface normal using a cylindrical lens, resulting in an optical spot size that was 2mm long by 35 µm wide, sufficiently large to ensure complete spatial overlap with the x-ray pulse. The incident fluence of the optical laser was sufficient to ensure complete melting of the probed region. Between each laser shot, the silicon sample was rastered to ensure that each measurement was conducted on a pristine surface. Optical and XFEL repetition rates were restricted to 1 Hz to ensure sufficient time between shots for sample translation.

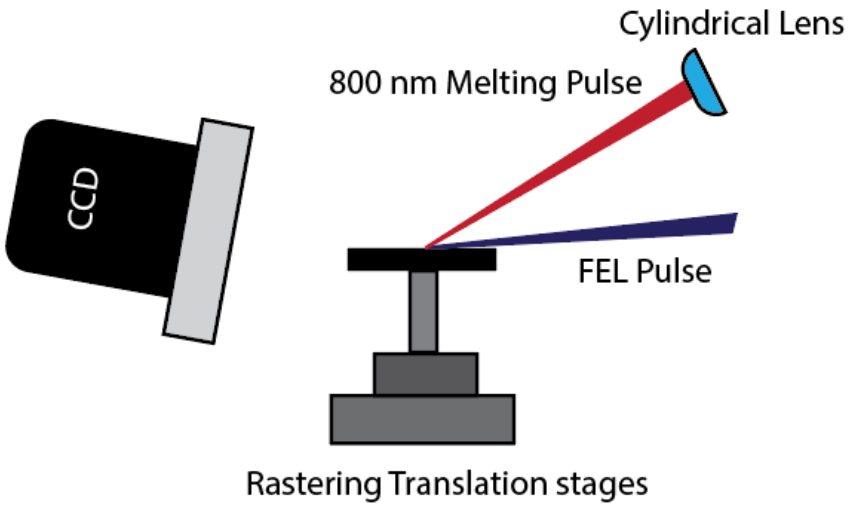

Figure 3.2: Experimental set-up for grazing incidence scattering experiments. The sample is mounted on a diffractometer and aligned at grazing incidence relative to the X-ray pulse. The FEL pulse, focused by Kirkpatrick-Baez mirrors, is spatially overlapped with an 800nm optical pulse, focused with a cylindrical lens. The sample was rastered in the plane of the sample surface and perpendicular to the travel direction of the laser propagation. Use of the grazing incidence geometry limits the penetration of the x-ray beams to only the uppermost few nanometers of the sample, as the penetration depth for the optical pulse I on the order of 100 nm, this ensures only the optically pumped portion of the sample is probed.

X-ray scattering patterns were collected for the unmelted sample and at 10 and 20 ps following excitation by the optical laser. Scattering intensity as a function of scattering angle was measured with a MPCCD (multi-port charge-coupled device) set at a working distance of 155 mm from the sample surface[35]. The CCD was subsequently scanned to obtain a q range of .25 to 2.4 $Å^{-1}$. Unmelted patterns were also taken at beamlines 2-1 and 10-2 of the Stanford Synchrotron Radiation Lightsource (SSRL) for comparison but exhibited no noticeable features over the angle range studied here.

3.4.3 Results/discussion

Figure 3.3 shows the difference in scattering patterns between the pumped and unpumped silicon target at times of 10 and 20 ps following the arrival of the optical laser pulse. For the first 10 ps following laser irradiation, the scattering is largely unchanged, remaining nearly identical to that of the silicon sample before irradiation. At 20 ps after the optical pulse, a dramatic shift in the scattering pattern is observed. The scattering intensity at low values increases by over an order of magnitude as can be seen.

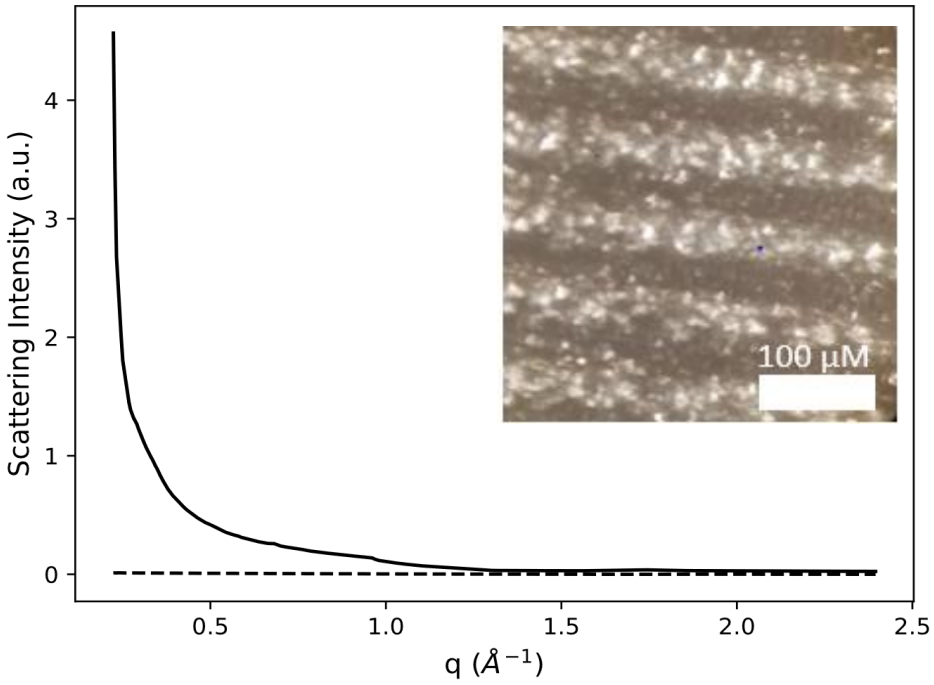

Figure 3.3: Main - X-ray scattering intensity measured from q=0 .25 to q o=2.4 $Å^{-1}$ at times of 10 ps (dashed) and 20 ps (solid) after irradiation with a fs laser. The scattering pattern for the unpumped silicon has been background-subtracted to highlight the impact of the ablation. While the scattering signal at 10 ps is quite similar to that of the unpumped sample, after 20 ps a large increase in scattering intensity is observed, attributed to the formation of liquid silicon droplets in the ablation plume.

Inset: Optical microscopy images of the silicon after laser ablation. The bright stripes are the ablation craters left over from interaction with the optical laser.

Scattering intensity in this region is associated with the development of inhomogeneity on the nanoscale, usually associated with nanoparticles and structures. The large increase in scattering intensity at t=20 ps is thus assigned to nanoscale sized objects that form in the ablation plume. Due to experimental limitation, we did not collect data at q values low enough for accurate modeling, which precludes a complete analysis and characterization of the scattering objects. Nevertheless, the magnitude of the intensity increase is compelling, and we can infer some details as to the carrier of the observed scattering signal.

Based on similarities to other studies[36,37], we assign the scattering intensity increase seen at 20 ps to the formation of large liquid silicon droplets in the ablation plume as it expands. The inset of figure 2 shows optical microscope images of the sample surface after interaction with the optical laser. As can be seen from the presence of ablation craters on the surface at 1.0 J/cm^2 fluence, we are clearly in the ablation regime for silicon. It has been observed that after laser irradiation of sufficient intensity, silicon transitions to a liquid metallic state, as evidenced by the increase in the sample's optical reflectivity for laser fluences above ~0.14 J/cm^2[2,38]. Initially in a high temperature and pressure state, the plasma expands and cools, eventually crossing the spinoidal line in the phase diagram, which results in fragmentation via the homogenous nucleation of gaseous bubbles throughout the liquid[20,39,40]. This process, known as *phase explosion*, is well-known to be important in the ablation of semiconductors after femtosecond irradiation, and has been observed in both experiments and theoretical investigations of the ablation process[13,41]. The 20 ps timescale observed in this experiment for the appearance of ablation-derived droplets agrees well with previous experimental observations of silicon ablation, wherein it was also observed that reflectivity loss due to the ablation occurred between 10 and 50 ps for the silicon (111) surface[42]. Additionally simulations of femtosecond laser ablation of solids find that when the ablating laser fluence is significantly above the ablation threshold, the onset of fragmentation due to void coalescence occurs on a similar 10's of ps timescale[20]. Thus, it is quite probable that we observed the very earliest steps in the liquid ablation process, with the observed droplets being related to the subsequently formed nanoparticles. As semiconductor ablation plumes are known to maintain optically smooth interfaces throughout the ablation process, it's possible to maintain the grazing incidence condition throughout the entirety of the material ablation[39,43]. As such the experiment is only sensitive to a narrow slice at the outermost surface of the ablation plume. In future experiments this fact may be of aid in modelling thermodynamic condition plume and relating them to the evolution of nanoparticles in the plume as probed by the x-ray scattering. While the two time points collected in this experiment are insufficient for an in depth analysis of the plume dynamics, the experimental techniques developed here establish the viability of applying an XFEL-based grazing incidence small angle x-ray scattering experiment as a tool for studying ablation dynamics. The use of a grazing incidence geometry results in a probe that is highly sensitive to the plume itself, while mitigating interference from the sample bulk. As small angle scattering is a sensitive tool for studying both nanoparticle size and morphology, it is well-suited to studying the formation dynamics of nanostructures in the plume on the ultrafast timescales enabled via use of an XFEL. Additionally, by tuning parameters such as laser fluence, gas pressure around the sample, and the nature of the substrate, a more complete understanding of how these interesting properties affect shape and properties of the resulting nanostructures can be achieved.

Conclusions

We have employed grazing incidence hard x-ray scattering using an ultrafast free electron laser source to study the earliest time points in the laser ablation of a silicon target. The dramatic rise in scattering intensity observed at low q in the experiment is attributed to the formation of nanoscale droplets of liquid silicon, resulting from phase explosion in the laser-prepared liquid. Grazing incidence x-ray scattering shows considerable promise as a tool for studying the ablation dynamics of laser irradiated substrates and the formation of nanoparticles. The technique can be easily extended to other materials, conditions, and time delays. This is significant, as very few experiments have been able to directly measure the properties of the ablation plume on ultrafast timescales. In future work, we hope to study the scattering over a broader angle and time range, effecting the direct study of both the growth and structural composition of the nanomaterials in the ablation plumes, which will facilitate a deeper understanding of the factors controlling the properties and morphology of nanoparticles produced by laser ablation, and will provide a valuable complement to the femtosecond second harmonic generation[8]and two-photon absorption[44]. experiments that we recently performed with free electron laser sources in the soft X-ray region.

References:

1. Koch, M. H. J. & Bordas, J. X-ray diffraction and scattering on disordered systems using synchrotron radiation. *Nucl. Instruments Methods Phys. Res.* **208**, 461 (1983).
2. Cloetens, P. *et al.* Phase objects in synchrotron radiation hard x-ray imaging. *J. Phys. D Appl. Phys* **29**, 133 (1996).
3. Uejio, J. S. *et al.* Characterization of selective binding of alkali cations with carboxylate by x-ray absorption spectroscopy of liquid microjets. *PNAS* **105**, 6809 (2008).
4. Wilson, K. R., Tobin, J. G., Ankudinov, A. L., Rehr, J. J. & Saykally, R. J. Extended X-Ray Absorption Fine Structure from Hydrogen Atoms in Water. *Phys. Rev Lett.* **85**, 4289 (2000).
5. Emma, P. ISSUES AND CHALLENGES FOR SHORT PULSE RADIATION PRODUCTION. *Proc. EPAC* 225 (2004).
6. Yu, L. H. Generation of intense UV radiation by subharmonically seeded single-pass free-electron lasers. *Phys. Rev. A* **44**, 5178 (1991).
7. Ben-Zvi, I. *et al.* Design of a harmonic generation FEL experiment at BNL. *Nucl. Instruments Methods Phys. Res. Sect. A Accel. Spectrometers, Detect. Assoc. Equip.* **318**, 208 (1992).
8. Lam, R. K. *et al.* Soft X-Ray Second Harmonic Generation as an Interfacial Probe Elettra-Sincrotrone Trieste. *Phys. Rev. Lett.* **120**, 23901 (2018).
9. Taylor, L. A. F. I. S. W. *General principles of small angle scattering*. (springer, 1987).

10. Mafuné, F., Kohno, J.-Y., Takeda, Y. & Kondow, T. Formation of Stable Platinum Nanoparticles by Laser Ablation in Water. *4218 J. Phys. Chem. B* **107**, 4218 (2003).

11. Kim, M., Osone, S., Kim, T., Higashi, H. & Seto, T. Synthesis of Nanoparticles by Laser Ablation: A Review. *KONA Powder Part. J.* **34**, 80 (2016).

12. Kabashin, A. V & Meunier, M. Synthesis of colloidal nanoparticles during femtosecond laser ablation of gold in water. *J. Appl. Phys.* **94**, 7941 (2003).

13. Ashfold, M. N. R., Claeyssens, F., Fuge, G. M. & Henley, S. J. Pulsed laser ablation and deposition of thin films. *Chem. Soc. Rev.* **33**, 23 (2004).

14. Basso, L. *et al.* An all-optical single-step process for production of nanometric-sized fluorescent diamonds. *Nanoscale* **10**, 5738 (2018).

15. Hu, A., Rybachuk, M., Lu, Q. B. & Duley, W. W. Direct synthesis of sp -bonded carbon chains on graphite surface by femtosecond laser irradiation. *Appl. Phys. Lett.* **91**, 1 (2007).

16. Koji Sugioka, Michel Meunier, A. P. *Laser Precision Microfabrication*. (2010).

17. Semaltianos, N. G. Nanoparticles by laser ablation. *Crit. Rev. Solid State Mater. Sci.* **35**, 105 (2010).

18. Besner, S., Kabashin, · A V, Winnik, F. M. & Meunier, · M. Ultrafast laser based & green synthesis of non-toxic nanoparticles in aqueous solutions. *Appl Phys A* **93**, 955 (2008).

19. Amendola, V. & Meneghetti, M. What controls the composition and the structure of nanomaterials generated by laser ablation in liquid solution? *Phys. Chem. Chem. Phys.* **15**, 3027 (2013).

20. Perez, D. & Lewis, L. J. Ablation of solids under femtosecond laser pulses. *Phys. Rev. Lett.* **89**, 255504 (2002).

21. Cavalleri, A., Sokolowski-Tinten, K., Bialkowski, J., Schreiner, M. & Von der Linde, D. Femtosecond melting and ablation of semiconductors studied with time of flight mass spectroscopy. *J. Appl. Phys.* **85**, 3301 (1999).

22. Johnson, S. L. *et al.* Bonding in Liquid Carbon Studied by Time-Resolved X-Ray Absorption Spectroscopy. *Phys. Rev. Lett.* **94**, 57407 (2005).

23. Gamaly, E. G., Rode, A. V., Luther-Davies, B. & Tikhonchuk, V. T. Ablation of solids by femtosecond lasers: Ablation mechanism and ablation thresholds for metals and dielectrics. *Phys. Plasmas* **9**, 949 (2002).

24. Glover, T. E. Hydrodynamics of particle formation following femtosecond laser ablation. *J. Opt. Soc. Am. B-Optical Phys.* **20**, 125 (2003).

25. Noël, S., Hermann, J. & Itina, T. Investigation of nanoparticle generation during femtosecond laser ablation of metals. *Appl. Surf. Sci.* **253**, 6310 (2007).

26. O. Albert, S. Roger, Y. Glinec, J.C. Loulergue, J. Etchepare, C. Boulmer-Leborgne, J. perriere, E. M. Time-resolved spectroscopy measurements of a titanium plasma induced by nanosecond and femtosecond lasers. *Appl. Phys. A* **76**, 319 (2003).

27. S. Amoruso, G. Ausanio, M. Vitiello, X. W. Infrared femtosecond laser ablation of graphite in high vacuum probed by optical emission spectroscopy. *Appl. Phys. A* **81**, 981 (2005).

28. Varel, H., Wähmer, M., Rosenfeld, A., Ashkenasi, D. & Campbell, E. E. B. Femtosecond laser ablation of sapphire: Time-of-flight analysis of ablation plume. *Appl. Surf. Sci.* **127**, 128 (1998).

29. Bulgakov, A. V., Ozerov, I. & Marine, W. Cluster emission under femtosecond laser ablation of silicon. *Thin Solid Films* **453**–**454**, 557 (2004).

30. Ibrahimkutty, S., Wagener, P., Menzel, A., Plech, A. & Barcikowski, S. Nanoparticle formation in a cavitation bubble after pulsed laser ablation in liquid studied with high time resolution small angle x-ray scattering. *Appl. Phys. Lett* **101**, 103104 (2012).

31. Tono, K. *et al.* Beamline, experimental stations and photon beam diagnostics for the hard x-ray free electron laser of SACLA. *New J. Phys.* **15**, 83035 (2013).

32. Owada, S., Togashi, T. & Yabashi, M. X-ray optics for advanced ultrafast pump – probe X-ray experiments at SACLA Tetsuo Katayama , Takashi Hirano , Yuki Morioka , Yasuhisa Sano , Taito. *J. Synchrotron rad.* **26**, 333 (2019).

33. Ishikawa, T. *et al.* A compact X-ray free-electron laser emitting in the sub-ångström region. *Nat. Photonics* **6**, 540 (2012).

34. Henke, B. L., Gullikson, E. M. & Davis, J. C. X-Ray Interactions: Photoabsorption, Scattering, Transmission, and Reflection at E = 50-30,000 eV, Z = 1-92. *At. Data Nucl. Data Tables* **54**, 181 (1993).

35. Kameshima, T. *et al.* Development of an X-ray pixel detector with multi-port charge-coupled device for X-ray free-electron laser experiments. *Rev. Sci. Instrum.* **85**, 33110 (2014).

36. Bagge-Hansen, M. *et al.* all-angle x-ray scattering during detonation of the high explosive hexanitrostilbene. *J. Appl. Phys* **117**, 245902 (2015).

37. Willey, T. M. *et al.* Measurement of carbon condensates using small-angle x-ray scattering during detonation of high explosives. *AIP Conf. Proc.* **1793**, 30012 (2015).

38. Sokolowski-Tinten, K. & Von der Linde, D. Generation of dense electron-hole plasmas in silicon. *Phys. Rev. B* **61**, 2643 (2000).

39. Sokolowski-Tinten, K. *et al.* Transient States of Matter during Short Pulse Laser Ablation. *Phys. Rev. Lett.* **81**, 224 (1998).

40. Cavalleri, A., Sokolowski-Tinten, K., Bialkowski, J., Schreiner, M. & Von der Linde, D. Femtosecond melting and ablation of semiconductors studied with time of flight mass

spectroscopy. *J. Appl. Phys.* **85**, 3301 (1999).

41. Yoo, J. H., Borisov, O. V, Mao, X. & Russo, R. E. Existence of Phase Explosion during Laser Ablation and Its Effects on Inductively Coupled Plasma-Mass Spectroscopy. *Anal. Chem.* **73**, 2288 (2001).

42. Sokolowski-tinten, K. *et al.* Dynamics of femtosecond-laser- induced ablation from solid surfaces. *SPIE* **3343**, 46 (2019).

43. Von der Linde, D., Sokolowski-Tinten, K. & Bialkowski, J. Laser–solid interaction in the femtosecond time regime. *Appl. Surf. Sci.* **109**, 1 (1997).

44. Lam, R. K. *et al.* Two-photon absorption of soft X-ray free electron laser radiation by graphite near the carbon K-absorption edge. *Chem. Phys. Lett.* **703**, 112 (2018).

Chapter 4:

On the Nature of Ions at the Air/Water Interface

4.1 Introduction

The chemistry of ions at the air/water interface has garnered a great deal of interest in the past few decades, driven by its importance in catalysis[1,2], atmospheric chemistry[3–5], biology[6,7], and a host of other contexts. Throughout the 20th century, the behavior of ions near aqueous interfaces was considered a solved problem. Conventional wisdom, deriving from classical electrostatics, held that all ions were depleted from the air/water interface, driven away by unfavorable solvation at the boundary between a high and low dielectric[8]. In the last two decades, however, it has become increasingly apparent that this simple picture of ion interfacial behavior is incomplete, and that ion behavior at interfaces is far more complex than previously assumed. New evidence from experiments[9,10] and simulations[11–13] implies that for some ions there is actually an *enhancement* of ion population at the air/water interface. This new insight has generated a renewed interest in studying the behavior of ions at interfaces to better understand why these ions exhibit an affinity for the surface and what implications it might have for oceanic, atmospheric and biological chemistry.

4.2 Ions at the Interface

4.2.1 Historical perspective

To define the interfacial population of a species, first the location of the interface itself must be established. Liquid interfaces generally do not exhibit abrupt changes in properties as the system transitions from one phase to the next. Instead, there exists a transition region of finite size at the boundary between media, where fundamental properties like density change from the bulk value of one medium to that of the other. A common definition for the location of the interface in this transitional region is the *Gibbs dividing surface(GDS)*, which is positioned so as to have the surface excess for one species in solution, typically the solvent, equal to zero. The surface excess for species i in the system is defined as:

$$\Gamma_i = \frac{N_i - C_i^a V_a - C_i^b V_b}{A} \qquad (4.1)$$

Here, N_i is the total population of species i in the system, C_i^x is the concentration of species i in the bulk of medium x, V_x is the volume for each medium and A is the area of the interface between the two media. With the interface defined so as to set the solvent excess to zero, all

other species in the system will exhibit either a positive or negative surface excess, corresponding to enhancement or depletion at this interface between the respective media.

The surface excess for a given species in solution can be experimentally determined via measurements of the water surface tension. The relationship between surface tension and surface excess can be derived from the thermodynamics of the interface. To do so, we begin with the Gibbs-Duhem equation for the surface:

$$A\partial\gamma + S\partial T + N\partial\mu_i = 0 \quad (4.2)$$

Here, A is again the area of the interface, μ_i and N_i are respectively the chemical potential and surface concentration of species i in the system, and γ is the surface tension. Assuming constant temperature and dividing by the interfacial area, the relationship between the surface tension and surface excess is expressed via the Gibbs adsorption isotherm:

$$\Gamma_i = \frac{-\partial\gamma}{d\mu_i} \quad (4.3)$$

From Equation 4.3, one can see that, for a solute exhibiting a negative surface excess, the surface tension increases upon addition of the species, whereas a positive surface excess results in surface tension decreasing as the solute is added. Experimentally it was observed that when inorganic salts were added to water, there was an increase in the measured surface tension[14,15]. In accordance with Equation 4.3, it was therefore concluded that ions must be depleted from the air/water interface.

To justify why ions tended to avoid the air/water interface, Onsanger and Samaras derived the image charge model for the adsorption using a continuum electrostatics approach[8], building on earlier work by Wagner[16]. The resultant Wagner-Onsager-Samaras (WOS) theory explained the behavior of ions near an interface between dielectric media in terms of image charge forces. Briefly, the image charge model states that as ions of charge q_{ion} in medium 1 with dielectric constant ε_1 approach the interface with a second dielectric of dielectric constant ε_2 the ions experience an image charge of magnitude:

$$q_{image} = \frac{(\varepsilon_1 - \epsilon_2)}{(\varepsilon_1 + \epsilon_2)} q_{ion} \quad (4.4)$$

As can be seen from this equation, if the ion is imbedded in the higher dielectric medium, then the sign of the image charge matches that of the ion and, therefore, the ion experiences

coulombic repulsion from the interface. As bulk water has a dielectric constant of ~80, while the vapor is a very weak dielectric, Equation 4.4 predicts that ions will avoid the air/water interface. While the WOS image charge model provided a simple explanation for the observation of increased surface tension upon addition of salt to solution, it was unable to account for several observed phenomena. Surface tension measurements of salts showed little variation with cation identity, but were found to depend strongly on the identity of the anion [17]. It was also observed for measurements of the water surface potential that addition of halide salts to the solution resulted in the potential becoming more negative, which seemingly implied the ions were accumulating at the interface[17]. For both the variation in surface tension and the surface potential, the ordering of the ions followed the inverse of the Hoffmeister series, a well-known ordering of ions first discovered for their ability to salt proteins into or out of solution. Beyond protein solubility, the Hoffmeister series arises in a variety of other natural phenomena, including enzyme activity[18] and optical rotation of light by chiral molecules[19].

The Hoffmeister series for anions is as follows:

$$F^- \approx SO_4^{2-} > HPO_3^{2-} > acetate > Cl^- > NO_3^- > Br^- > ClO_3^- > I^- > ClO_4^- > SCN^- \quad (4.5)$$

Ions on the left side of the Hoffmeister series which interact strongly with water molecules are known as kosmostropes or structure makers; the weakly solvated ions on the right side are commonly referred to as chaotropes or structure breakers. For these chaotropic ions, the name derives from the assumption that, due to their size and weak solvation energies, the ions heavily disrupted the hydrogen bonding structure of bulk water. The WOS theory was unable to explain why these chaotropic anions showed ion-specific effects on the surface tension and surface potential of water, nor could any of the later extensions or refinements of the WOS theory[20–22]. Despite these shortcomings, the depletion of ions from the air/water interface, as predicted by WOS theory, was generally accepted as fact for the next half century.

4.2.2 Ions and atmospheric chemistry

While the inability to account for the surface tension effects discussed in the previous section had always been a weakness of the WOS theory, it was only when explicit discrepancies were observed in experimental measurements from the atmospheric community that the fundamental assumption of general ion depletion at the air/water interface was called into question. Field campaigns measuring ozone level in the Arctic observed that ozone depletion events were strongly correlated with changes in atmospheric concentration of bromine-containing compounds Br_2 and BrCl. The strong correlation between the molecules made it clear that the observed ozone depletion must be result of ozone reacting with photolyzed bromine, but the source for the bromine molecules in the reaction was unclear. One source proposed for the requisite bromine molecules was bromide ions in sea salt aerosols and artic snow packs[23], which, through oxidation by ozone gas, could yield Br_2. In order to determine whether such a mechanism for bromine generation was important in these ozone depletion events, Hunt et al. performed chamber experiments modeling the kinetics of reactions between sodium bromide

aerosol particles and gaseous ozone[4]. In these experiments, it was observed that the use of bulk-phase kinetic rate constants for the reaction between ozone and the bromide significantly underestimated the rate of bromine production in the chamber, as measured via FTIR and API-MS. To account for this anomalously fast production of bromine, it was proposed that the bromine must originate from heterogenous chemistry taking place at the aerosol surface between gas phase ozone and bromide ions accumulated at the air/water interface [3–5,24]. The presence of such ions near the interface is, of course, a direct contradiction of the predictions from the WOS model. However, the inclusion of interfacial reactions in the kinetics model significantly improved the agreement between the model predictions and the experimentally observed rate of bromine production. Further evidence for the presence of halide anions at the interface was found in a kinetic study of reactions between sodium chloride particles and hydroxyl radicals carried out by Knipping et al. in 2000. Once again, it was found that bulk phase reaction rates were unable to account for the observed production of chlorine gas in the reaction chamber, necessitating the addition of a surface reaction channel in the kinetics model. As with the experiments carried out by Hunt, much better agreement between model and experiment was achieved with the inclusion of these surface reactions. For both experiments described above, the conclusions of the study supported the proposal that halides ions accumulate at the air/water interface and participate in reactions with gaseous species. However, as discussed in earlier section, both the WOS theory and surface tension measurements implied there should be no such interfacial ion population. Simulations from the theoretical community, along with new experimental measurements would soon put this assumption to the test, as we discuss next.

4.3 Simulations of Interfacial Halides

The results from atmospheric studies like those discussed above inspired theorists to reexamine the behavior of ions near the air/water interface. The results of these new studies showed how the simple WOS model was inadequate for describing the newly observed ion behavior at the air/waster interface, necessitating an entirely new theoretical framework.

4.3.1 Cluster simulations

Even before atmospheric chemistry field studies called WOS theory into question, there had already been earlier indications from the modeling community that concentrations of some halides might be enhanced at the interface. Molecular dynamics simulations carried out by Perera et al in 1991 studied the behavior of chloride anions in clusters of up to 14 water molecules[25,26] employing an SPCE/POL model, wherein it was observed that sodium cations stayed in the cluster interior, while chloride anions unexpectedly preferred to reside on the surface of the water clusters. Based on the results of these simulation, Perera concluded that the anion was expelled to the cluster surface to minimize the energetic penalty from disruption of the cluster hydrogen bonding network[25]. In later studies on water clusters of similar size[27], Perera proposed that bromide and iodide should display the same preference for interfacial attachment as had been seen for chloride, based on a rescaling the solvent stabilization energies of bromide, iodide and chloride to fall onto a universal curve. This rescaling behavior implied that similar solvation structures existed for all three anions in small water clusters, although whether

the similarities would persist in larger water clusters or in the bulk was uncertain. In contrast to the larger halides, Perera found fluoride behaved quite differently in the small water cluster simulations[26]. It was found that the fluoride anion preferentially localized at the center of the clusters, similar to previous results for cations, while chloride anions in the same study were once again found to reside on the surface. The authors attributed this difference in the behavior of the two anions to the tendency of water molecules to preserve the tetrahedral hydrogen bonding network in the cluster. It was assumed that, in accordance with the old concept of chaotropic vs. kosmotropic ions, that the larger chloride disrupted the hydrogen bonding inside the cluster and was thus excluded from the interior. However, given that these results were obtained for small water clusters, it was unclear whether the observed interfacial localization of the larger halides extrapolate to more extended water surfaces.

4.3.2 Slab geometry simulations

One of the first experiments to simulate such an extended water surface was the previously discussed study carried out by Knipping et al. in 2000. This experiment provided justification for the inclusion of surface reaction channels in the kinetic model by performing molecular dynamics simulations at the surface of a solution of sodium chloride. The molecular dynamics simulations employed both a non-polarizable model and a model that included the polarizability of both the water and the chloride anion, the results of which provided strong justification for the inclusion of surface reaction channels in the kinetic models. Significant chloride populations were found at the interface for both the non-polarizable and polarizable models, with the surface anion coverage being 3.3% and 11.9% respectively. Meanwhile, for both models, the sodium counterions were observed to be sequestered in the bulk-away from the interface. The difference in the ion behaviors was attributed to the relative size of the cations vs. the anions, as well as differences in the cation and anion polarizability. The observed importance of polarizability in promoting the presence of the chloride at the interface resulted in speculation that other halides, viz. iodide and bromide, with their higher polarizability, might also be present at the interface, as had been implied by the earlier cluster studies of Pererra et al.

The prediction of larger halides having stronger surface affinity was later confirmed in molecular dynamics simulations carried out by Jungwirth and Tobias[28]. They simulated the behavior of a series of sodium halides salts at the air/water interface, with a focus on the ion population density as a function of distance from the surface. In agreement with the earlier cluster studies, fluoride was found to exhibit depletion near the interface, as predicted from WOS theory. In contrast, chloride, bromide and iodide all showed population enhancement at the air/water interface. For these larger anions, the surface propensity was found to follow the same inverse Hoffmeister series that had been observed in earlier surface tension measurements, with the largest anion(iodide) having the greatest surface population, while chloride had the lowest surface affinity. For all of the anions simulated, a sub-surface depletion zone was found to occur below the region of surface enhancement, such that the net ion population in the surface region was depleted relative to the bulk. In this way, the molecular dynamics simulation were found to be consistent with past studies of the surface tension of halide solutions, viz a net increase in surface tension indicating a net decrease in interfacial salt

concentration. As in the previously discussed simulations of chloride, ion size and polarizability were concluded to play the dominant role in determining surface affinity of the ions.

After decades of assuming that all ions were depleted at the air/water interface, based on the WOS theory, the predictions of *ion enhancement* at the interface in the previously described simulations came as a surprise to many. However, given the unresolved discrepancies between experimental measurements of surface tensions of solution and the predictions of the WOS model, it had been clear that the behavior of ions at the surface must be more complex than was previously assumed. Even so, it took unambiguous experimental confirmation of the presence of ions at the air/water interface before it became widely accepted that large polarizable anions like iodide indeed exhibited enhanced surface populations at the air/water interface.

4.4 Experimental Studies of Ions Near the Air/Water Interface

Experimental studies seeking to measure and quantify the populations of ions at the water/vapor interface have historically proved challenging, partly explaining why the mistaken belief that all ion were depleted persisted for so long. Experiments to study the ion population in the nanoscopically thin interfacial region require techniques that can rigorously discriminate between signal coming from the interface and that from the bulk, where significantly more ions reside. As such, only a few experimental techniques are suitable carrying out such studies of interfacial ion populations.

4.4.1 Non-linear optical spectroscopy studies

Second-order nonlinear optics is a powerful tool for the study of interfacial phenomena, owing to the very high sensitivity to the interface and ability to measure sub-monolayer coverages of adsorbant. As previously discussed, the technique's high surface sensitivity results from the fact that χ^2 is necessarily zero in a centrosymmetric medium(in the dipole approximation), such as the bulk of a solution, due to cancellation of dipoles. Hence all signal in experiments employing second order non-linear optic techniques is generated from the interfacial region, where the presence of the interface breaks the centrosymmetry of the medium. Experiments and theory have predicted probe depths of ca. 1 nm for second-order nonlinear optical spectroscopies[29], hence, these methods are usually sensitive to species only in the uppermost few water layers of the solution.

Some of the first experiments to confirm the presence of halide anions at the air/water interface were indirect studies from sum frequency generation spectroscopy(SFG). SFG is a second order non-linear optic technique akin to the previously discussed second harmonic generation. Unlike SHG, in SFG two input electric fields of different fundamental frequencies are incident on the sample interface and the resultant second-order photons are generated at the sum of the two input frequencies. SFG also exhibits resonant enhancement when either of the fundamental frequencies or their sum is resonant with a transition in the investigated solution; usually, one of the input frequencies in SFG experiments is in the IR, and the SFG experiment therefore measures a vibration spectrum of the solution surface.

SFG experiments carried out in 2004 by Raymond et al studied the vibrational modes of interfacial waters in sodium halide solutions[30]. For solutions of the larger halides iodide and bromide, the authors observed an increase in the intensity of the SFG response in the O-H vibrational region near 3000 cm^{-1}, attributed to double layer effects resulting from charge separation at the interface. A blue shift of the O-H stretching vibrations was also observed in the SFG spectra. This was concluded to be a result of structure breaking by the chaotropic iodide and bromide anions, which disrupted the interfacial hydrogen bond network. Given the shallow probe depth of the SFG probe, the observation of these changes in the SFG spectra was taken as evidence for the presence of at least iodide and bromide in the interfacial region of the solution. Further support for the presence of anions at the water surface was obtained from SFG studies carried out by other investigators, which observed similar intensity increases for the vibrational peaks in the SFG spectrum and changes in the O-H bond vibrational frequency in the presence of halide salts[31–33]. The experimental evidence for the presence of halides near the interface provided support for the molecular dynamics simulations discussed previously. However, the changes in the water vibrational spectrum comprise only indirect evidence for the presence of the anions at the water surface. To more directly measure the surface propensity of anions, a different technique was necessary, viz. resonant deep UV second harmonic generation(DUV-SHG).

While the monovalent halide anions lack vibrational chromophores that can serve as tags in SFG studies, they do exhibit strong accessible electronic transitions, albeit in the deep ultraviolet. Peterson et al. exploited the presence of the intense CTTS transition in iodide in an effort to experimentally study the interesting and controversial Jones-Ray Effect in aqueous solutions. The Jones-Ray Effect is an anomalous, small *decrease* in solution surface tension observed for 13 different salts at concentrations near 1 mM. In the DUV_SHG experiment, Peterson et al exploited the strong resonant enhancement of SHG to directly probe the population of iodide at the air/water interface. It was observed that, in the concentration range between 0 and .1 M, there was a change in the measured SHG intensity that the authors attributed to halide adsorption at the interface, providing direct evidence for the existence of iodide anions at the water surface. The interfacial population was found to follow a Langmuir adsorption isotherm. Through fitting of the concentration-dependents SHG signal, the authors were able to extract a free energy of adsorption for iodide of -6.2 kcal/mol. Subsequent papers provided the first experimental evidence for non-halide anions adsorbing at the interface as well. In a study carried out in 2004, the azide population at the interface was measured using the DUV-SHG technique. As with iodide, the adsorption of azide at the interface showed Langmuir isotherm characteristics, and fitting of the concentration dependent SHG signal yielded a free energy of adsorption of -9.9 kJ/mol. This pair of experiments on iodide and azide provided direct experimental evidence for the interfacial enhancement not only of halides but non-halide anions as well. In the decade and a half since these experiments, a wide variety of other anions have also been detected at the air-water interface using the same technique, including thiocyanate[34], nitrate[35], nitrite[36], and bromide[37]. For all of these anions, the interfacial energy minima are shallow, ca. a few kJ/mol for even the most surface active of the ions, like thiocyanate and iodide. Table 4.1 shows the fitted free energies of adsorption for the studied anions.

For the polyatomic anions like thiocyanate that possess vibrational modes, resonant VSFG can be used as a complementary experimental technique, permitting measurement of the ion orientation at the interface. For thiocyanate, Viswanath carried out a study using the CN stretching mode near 2065 cm^{-1} [38]. As in the DUV-SHG studies, the thiocyanate anion was found to exhibit a pronounced population enhancement near the air/water interface. By studying the SFG spectrum and employing a variety of different input and output light polarizations, the authors were able to deduce an orientation about 45° relative to the surface normal for interfacial thiocyanate ions.

Anion	Fit free energy of adsorption	Reference
Iodide (I^-)	-25.9±.8 kJ/mol	39
Azide (N_3^-)	-9.9±.3 kJ/mol	40
Thiocyanate (SCN^-)	-7.53±.13 kJ/mol	34
Bromide (Br^-)	~-3 kJ/mol	37
Nitrite (NO_2^-)	-17.8 ±.3 kJ/mol	36

Table 4.1: Free energy of adsorption for various anions at the air/water interface

SFG can also be used as a tool for the investigation of interfacial *electronic* transitions. Rizzuto et al. applied broadband sum frequency generation in the deep UV to characterize the CTTS transition for iodide at the air/water interface. The CTTS transition is highly sensitive to the details of the surrounding solvent medium, as we discuss further in Chapter 5, and as such allows for characterization of the ion solvation and interactions at the air/water interface. In the experiment it was observed that the j=1/2 and j=3/2 CTTS lines for the iodide ion were significantly narrowed at the interface relative to their width in bulk solution spectra. This observed change in the linewidth was attributed to a possible change in the CTTS state lifetime at the interface. A dramatic difference in the ratio of the 3/2 to 1/2 peaks at the interface relative to bulk was also observed in the surface electronic spectra, which was speculated to be a result of double resonance enhancement for the j=3/2 peak, although additional modeling was deemed necessary to confirm that origin.

Second-order nonlinear optics has proved to be a powerful tool for the study of ions near the air/water interface. The technique has permitted the first direct confirmation that ions do reside in the uppermost water layers of the interface. The principal weakness of SHG and SFG experiments is the poor sensitivity, due to the weakness of the second-order process. An additional complication stems from the fact that direct probing of the ions at the interface requires that a suitable and experimentally accessible spectral transition exist for the target ion. Even when a suitable transition exists, resonant SHG studies often must be carried out in the deep UV, which is inconvenient as these photons are vulnerable to severe absorption losses

,restricting the systems that can be studied with the technique. A complementary tool for studying interfacial ions that transcends these limitations is x-ray photoelectron spectroscopy.

4.4.2 X-ray photoelectron spectroscopy

X-ray photoelectron spectroscopy (XPS) was one of the first tools employed to directly study the interfacial adsorption of ions and continues to be an important technique for characterizing the surface propensity of ions in solution. Surface sensitivity in XPS results from the limited inelastic mean free path of emitted photoelectrons in condensed media, which is dependent on their kinetic energy [41]. The relationship between the mean free path and photoelectron energy is classically described by a "universal curve " [41]. By controlling the energy of the outgoing electron via tuning of the wavelength of the incident x-rays, the probe depth of the technique can be limited to only a few nm[42]. As such, XPS possesses the requisite surface sensitivity for studying ion population in the interfacial region. The technique can also be used for controllable depth profiling of species in the solution.

The first XPS experiment to report the presence of interfacial halide anions at a solution surface was a study by Garrett of the deliquesced NaI and NaBr solutions on salt disks[43]. Rather than monitoring the halide signal alone, the authors monitored the anion/cation signal ratio as a function of the chamber humidity. It was found that when humidity in the chamber was increased above the deliquescence point, there was a significant increase in the relative ratio of I/Na and Br/Na, implying that the halide ions were more abundant at the interface than were the cations. For both iodide and bromide, the measured surface anion concentrations were higher than the solution bulk value, in agreement with the theoretical predictions of a positive surface excess for these larger halides. By studying the ratio as a function of the photoelectron energy, it was determined that the greatest enhancement for the halides was found for the lowest energy photoelectrons, which are derived from the uppermost layers of solution. As the photoelectron energy was increased, the halide/Na ratio returned asymptotically to the bulk values, as would be expected. This was compelling evidence for the accumulation of halide ions at the air/water interface. Similar studies of bromine-doped NaCl crystals found that the bromide was also selectively enhanced at the surface relative to the chloride, in keeping with both the Hoffmeister series and with prior simulations[44]. In the unwetted salt discs used in the experiment, two different bromide doping ratios were studied, 7% and .1%. When humidity in the chamber was increased above the deliquescence point, however, a massive enhancement of the bromide signal over chloride was observed, as predicted. As with the study carried out by Ghosal, the majority of the excess was found at the lowest electron kinetic energies, implying the bromide enhancement was mostly localized at the outermost water layers.

XPS has also been applied to the study of non-halide ions at the air/water interface. In contrast to resonant DUV-SHG studies, XPS experiments on nitrate and nitrite solutions found the population of both anions to be depleted at the air/water interface relative to the bulk[45]. The authors noted, however, that even though there was apparent ion depletion at the interface at all concentrations measured, there were at least some ions residing in the interfacial region at all concentrations. The authors also observed for both the nitrate and nitrite solutions that the interfacial region was unusually deep, with the ion concentration remaining below bulk values up to an electron kinetic energy of 600 eV, analogous to a solution depth of ~3 nm. Alkali halides

measured in earlier experiments returned to bulk solution concentrations significantly faster[43], usually in about 1 nm. The authors attributed this long interfacial region to nitrate and nitrite being polyatomic ions, which have directional solute-solvent interactions which serve to structure water more deeply into the solution than do spherical halide ions.

In general, the findings from x-ray photoelectron spectroscopy provide good support for the results of simulations of ions near the air/water interface. XPS experiments benefit from a larger signal and higher signal to noise than is available from non-linear optics, where the second order process responsible for signal generation is quite weak. However, while the interfacial depth for SHG and SFG have been modeled to be on the order of a nanometer, XPS spectroscopy has a deeper minimum probe depth, and is considered to be *surface sensitive* rather than *surface specific,* as are the second-order optical techniques [46]. As a result, XPS is still somewhat sensitive to the solution bulk, including the subsurface depletion region, and will likely underpredict the interfacial enhancement. To achieve the best understanding possible of the behavior of ions at the interface, a combination of experimental techniques including SHG, SFG, XPS and others must be employed.

4.5 Mechanism for Ion Adsorption at Aqueous Interfaces

As it is now widely accepted that certain ions, namely large and highly polarizable anions like iodide, do exhibit interfacial enhancements, there has been a growing interest in establishing the thermodynamic mechanism that drives these ions to the interface. In trying to understand the stabilization of these ions at the surface, a variety of interconnected factors must be considered viz. ion size, polarizability, solvation energy. Any or all of these properties might play a critical role in determining whether or not a given ion exhibits surface enhancement. To fully understand the physics of ions at interfaces, it is desirable to disentangle the contributions from these effects and derive new universal model that can describe interfacial ion behavior. However, such a model has proven elusive and there remain important questions to be answered regarding the forces that drive ions to adsorb at the interface.

Even from the earliest simulations of ion adsorption at the air/water interface, the role played by ion size has been recognized as important in determining its interfacial affinity. As discussed earlier, it has been argued by many that the large size of chaotropic anions like iodide and bromide resulted in disruption of the water hydrogen bonding network, making it favorable to displace them to the interface, where the energetic penalty in minimized. However, recent experiments are increasingly showing that the division of anions into chaotropic vs. kosmotropic categories is itself an artificial distinction. Pump-probe spectroscopy experiments by Omta et. al. in 2004 on the rotational dynamics of water found that neither chaotropic nor kosmotropic ions in solution had any effect on the hydrogen bonding structure of liquid water. As such, it seems that ions may not participate in either structure making or structure breaking in solution, and changes in the solution hydrogen bond structure cannot be used as a primary rationale for understanding why some ions exhibit surface activity while others do not.

Most early models for interfacial ion adsorption assumed that the adsorption was enthalpically disfavored due to the need to partially strip the ion solvation shell as it moved to the interface. This enthalpic penalty was offset by a favorable entropy increase from the freeing of the solvating water molecules and the reduction of excluded volume by segregating the ion to the interface[47,48]. In this model for ion adsorption, polarizability was important because it allowed the ion electron cloud to be distorted and to shift the charge deeper into solution. This induction effect helped to reduce the energetic cost of placing the negatively charged anion in the vicinity of the air/water interface. This assumption that the adsorption at the interface was entropically driven persisted until simulations by Caleman in 2011 finally recognized the importance of the interfacial water-water contributions in driving anions to the solution surface[49]. In molecular dynamics simulations of the surface of halide solutions, Caleman simulated the potentials of mean force for the anion as it approached the air/water interface, splitting the derived energy it into enthalpic and entropic contributions. Contrary to expectations, Caleman found that the enthalpic contribution for ion adsorption at the air/water interface was in fact negative and favorable. The energetic losses due to the desolvation of the ion as it approached the surface were compensated by inductive effects due to the anion polarization and favorable gains in the water-water energy as the anion approached the surface. However, the smaller cation was found to avoid the interface entirely, due to a combination of lower polarizability and strong solvation, which the water-water energy gains could not overcome. The entropic change in moving an ion to the interface was found to be negative in Caleman's simulations, although the origin of this unfavorable entropic contribution was not discussed in detail.

Experimental validation for the partitioning of the adsorption free energy revealed in Caleman's simulation was provided by the resonant DUV-SHG study carried out by Otten et al. on the thermodynamics of thiocyanate adsorption to the air/water interface[50]. In the study, the free energy of adsorption for the thiocyanate anion was measured as a function of the temperature, allowing for the enthalpic and entropic components of the free energy to be separated. From these experiments, it was determined that the enthalpic component for the adsorption of the anion was favorable, with a value of -11.8±.8 kJ/mol, while the entropic component was negative, having a value of -17±3 J/mol K. The authors of the study employed molecular dynamic simulations to clarify the origin of each of these contributions. It was determined that the favorable enthalpy of adsorption resulted from both the displacement of weakly-interacting interfacial waters as the anion approached the surface, and from the loss of weakly bound solvent molecules as the ion entered the interfacial region. Waters molecules at the interface were found to have high energy relative to those in the bulk, due to lack of hydrogen bonding partners at the outermost water layers. The enthalpic penalty of moving the ion to the interface and partially desolvating it was found to be outweighed by the energy gained via return of these high energy water molecules to the bulk, where they were more fully coordinated. The unfavorable entropic component for anion adsorption resulted from the pinning of surface capillary waves as the ion approached the interface. This experiment and the accompanying simulation provided the clearest understanding yet obtained of the forces resulting in the movement of certain ions to the air/water interface. However, this proposed mechanism is not without controversy, as there has been some argument as to whether the observed pinning of capillary waves in the simulation was real or was instead an artifact of the size of the simulation

box [51,52]. Moreover, the simulation model did not contain counterions. Hence, both additional experimental measurements and additional modelling are needed to further test and validate this proposed mechanism.

Conclusions

It is now well-accepted that certain ions exhibit a pronounced affinity for the air/water interface, in contrast to earlier predictions which stated that all ions were repelled from the boundary. The ions which exhibit surface enhancement share a variety of properties, generally being large, highly polarizable and having low solvation energies. Some debate remains regarding the mechanism that drives these ions to accumulate at the interface, with additional experiments needed to better validate and test models of ion adsorption, particularly including the effects of counterions and ion pairing. Developing a complete understanding of why these ions move to the interface is critical not only for understanding the fundamental physics of ion solvation, but for accurately modeling atmospheric processes, catalysis, and biological systems. Developing a truly universal model for the physics of ions at interfaces requires the combined effort of both experimentalist and theorists. Only by carrying out measurements of ion adsorption at an array of complex and varied interfaces and pairing these measurements with detailed simulations can models for interfacial ion adsorption be validated and a more complete picture of aqueous interfaces emerge.

References:

1. Beattie, J. K., Mcerlean, C. S. P. & Phippen, C. B. W. The Mechanism of On-Water Catalysis. *chem. Euro J* **16**, 8972 (2010).
2. Enami, S., Sakamoto, Y. & Colussi, A. J. Fenton chemistry at aqueous interfaces. *PNAS* **111**, 623 (2014).
3. Spicer, C. W. *et al.* Molecular halogens before and during ozone depletion events in the Arctic at polar sunrise: concentrations and sources. *Atmos. Environ.* **36**, 2721 (2002).
4. Hunt, S. W. *et al.* Formation of Molecular Bromine from the Reaction of Ozone with Deliquesced NaBr Aerosol: Evidence for Interface Chemistry. *J. Phys. Chem. A* **108**, 11559 (2004).
5. Oum, K. W., Lakin, M. J. & Finlayson-Pitts, B. J. Bromine activation in the troposphere by the dark reaction of O3 with seawater ice. *Geophys. Res. Lett.* **25**, 3923 (1998).
6. Rembert, K. B. *et al.* Molecular Mechanisms of Ion-Specific Effects on Proteins. *J. Am. Chem. Soc* **134**, 10039 (2012).
7. Hofmeister, F. Zur Lehre von der Wirkung der Salze. *Arch. für Exp. Pathol. und Pharmakologie* **24**, 247 (1888).

8. Onsager, L. & Samaras, N. N. T. The Surface Tension of Debye-Hückel Electrolytes The Surface Tension of Debye-Huckel Electrolytes. **2**, 528 (1934).

9. Rizzuto, A. M., Irgen-Gioro, S., Eftekhari-Bafrooei, A. & Saykally, R. J. Broadband Deep UV Spectra of Interfacial Aqueous Iodide. *J. Phys. Chem. Lett* **7**, 3885 (2016).

10. Weber, R. *et al.* Photoemission from Aqueous Alkali-Metal-Iodide Salt Solutions Using EUV Synchrotron Radiation. *J. Phys. Chem. B* **108**, 4729 (2004).

11. Ottosson, N. *et al.* The influence of concentration on the molecular surface structure of simple and mixed aqueous electrolytes. *Phys. Chem. Chem. Phys.* **12**, 10637 (2010).

12. Dang, L. X., Rice, J. E., Caldwell, J. & Kollman, P. A. Ion solvation in polarizable water: molecular dynamics simulations. *J. Am. Chem. Soc.* **113**, 2481 (1991).

13. Thomas, J. L., Roeselová, M., Dang, L. X. & Tobias, D. J. Molecular Dynamics Simulations of the Solution-Air Interface of Aqueous Sodium Nitrate. *J. Phys. Chem. A* **111**, 3091 (2007).

14. Heydweiller. Zur Kenntnis der Glaselektrolyse. *Ann. Phys.* **33**, 154 (1910).

15. Jones, G. & Ray, W. A. A Differential Method for Relative Surface Tension The Surface Tension of Solutions of Electrolytes as a Function of the Concentration. I. A Differential Method for Measuring Relative Surface Tension. *A Differ. Method Relat. Surf. Tens.* (1937).

16. Wagner, C. Die Oberflächenspannung verdünnter elektrolytlösungen. *Phys. Z.* **25**, 474 (1924).

17. Levin, Y., Santos, A. P., Diehl, A., Dos Santos, A. P. & Diehl, A. Ions at the Air-Water Interface : An End to a Hundred-Year-Old Mystery ? *Phys. Rev Lett.* **103**, 257802 (2009).

18. Cacac E, M. G., Landa, E. M., Mon, U. & Ramsde N, J. J. The Hofmeister series : salt and solvent effects on interfacial phenomena. *Q. Rev. Biophys.* **25**, 241 (2019).

19. Nostro, P. Lo, Ninham, B. W., Milani, S., Fratoni, L. & Baglioni, P. Specific anion effects on the optical rotation of glucoseand serine. *Biopolymers* **81**, 136 (2006).

20. Dean, D. S. & Horgan, R. R. Field theoretic calculation of the surface tension for a model electrolyte system. *Phys. Rev. E* **69**, 61603 (2004).

21. Nichols, A. L., Pratt, L. R., Iii, A. L. N. & Pratfl, L. R. The Surface Tension of Debye-Hückel Electrolytes The. *Surf. Tens. Ion. Solut. J. Chem. Phys.* **80**, 312 (1984).

22. Levin, Y. Interfacial tension of electrolyte solutions. *J. Chem. Phys* **113**, 9722 (2000).

23. B. J. Finlayson-Pitts, F. E. L. & H. N. B. Ozone destruction and bromine photochemistry at ground level in the Arctic spring. *Nature* **343**, 622 (1990).

24. Hu, J. H. *et al.* Reactive Uptake of Cl2(g) and Br2(g) by Aqueous Surfaces as a Function of Br and I Ion Concentration: The Effect of Chemical Reaction at the Interface. *J. Phys.*

Chem **99**, 8768 (1995).

25. Perera, L. & Berkowitz, M. L. Structure and dynamics of Cl-(H2O)20 clusters: The effect of the polarizability and the charge of the ion. *J. Chem. Phys.* **96**, 3757 (1992).

26. Perera, L. & Berkowitz, M. L. Structures of Cl-(H2O)n and F-(H2O)n (n=2,3,...,15) clusters. Molecular dynamics computer simulations. *J. Chem. Phys.* **100**, 3085 (1994).

27. Perera, L. & Berkowitz, M. L. Stabilization energies of Cl-, Br-, and I- ions in water clusters. *J. Chem. Phys.* **99**, 102321 (1993).

28. Jungwirth, P., Tobias, D. J. & Heyrovsky, J. Molecular Structure of Salt Solutions: A New View of the Interface with Implications for Heterogeneous Atmospheric Chemistry. *J. Phys. Chem. B* **105**, 1 (2001).

29. Raymond, E. A., Tarbuck, T. L., Brown, M. G. & Richmond, G. L. Hydrogen-Bonding Interactions at the Vapor/Water Interface Investigated by Vibrational Sum-Frequency Spectroscopy of HOD/H 2 O/D 2 O Mixtures and Molecular Dynamics Simulations. *J. Phys. Chem. B* **107**, 546 (2003).

30. Raymond, E. A. & Richmond, G. L. Probing the Molecular Structure and Bonding of the Surface of Aqueous Salt Solutions. *J. Phys. Chem. B* **108**, 5051 (2004).

31. Shultz, M. J. *et al.* Sum frequency generation spectroscopy of the aqueous interface : Ionic and soluble molecular solutions. *Int. Rev. Phys. Chem.* **19**, 123 (2000).

32. Shultz, M. J., Baldelli, S., Schnitzer, C. & Simonelli, D. Aqueous Solution/Air Interfaces Probed with Sum Frequency Generation Spectroscopy. *J. Phys. Chem. B* **106**, 5313 (2002).

33. Mucha, M. *et al.* Unified Molecular Picture of the Surfaces of Aqueous Acid, Base, and Salt Solutions. *J. Phys. Chem. B* **109**, 7617 (2005).

34. Petersen, P. B., Saykally, R. J., Mucha, M. & Jungwirth, P. Spectroscopy and MD Simulations of Sodium Thiocyanide. *J. Phys. Chem. B* **109**, 10915 (2005).

35. Otten, D. E., Petersen, P. B. & Saykally, R. J. Observation of nitrate ions at the air/water interface by UV-second harmonic generation. *chem. Phys. Lett.* **449**, 261 (2007).

36. Otten, D. E., Onorato, R., Michaels, R., Goodknight, J. & Saykally, R. J. Strong surface adsorption of aqueous sodium nitrite as an ion pair. *Chem. Phys. Lett.* **519**–**520**, 45 (2012).

37. Onorato, R. M., Otten, D. E. & Saykally, R. J. Measurement of Bromide Ion Affinities for the Air/Water and Dodecanol/Water Interfaces at Molar Concentrations by UV Second Harmonic Generation Spectroscopy. *J. Phys. Chem. C* **114**, 13746 (2010).

38. Viswanath, P. & Motschmann, H. Oriented Thiocyanate Anions at the Air-Electrolyte Interface and Its Implications on Interfacial Water-A Vibrational Sum Frequency Spectroscopy Study. *Phys. Chem. C Lett* **111**, 4484 (2007).

39. Petersen, P. B., Johnson, J. C., Knutsen, K. P. & Saykally, R. J. Direct experimental

validation of the Jones–Ray effect. *Chem. Phys. Lett.* **397**, 46 (2004).

40. Petersen, P. B. & Saykally, R. J. Confirmation of enhanced anion concentration at the liquid water surface. *Chem. Phys. Lett.* **397**, 51 (2004).

41. Powell, C. J. & Jablonski, A. Surface sensitivity of X-ray photoelectron spectroscopy. *Nucl. Instruments Methods Phys. Res. Sect. A Accel. Spectrometers, Detect. Assoc. Equip.* **601**, 54 (2009).

42. Stoerzinger, K. A., Hong, W. T., Crumlin, E. J., Bluhm, H. & Shao-Horn, Y. Insights into Electrochemical Reactions from Ambient Pressure Photoelectron Spectroscopy. *Acc. Chem. Res* **48**, 27 (2015).

43. Garrett, B. C. *et al.* Electron Spectroscopy of Aqueous Solution Interfaces Reveals Surface Enhancement of Halides. *Science (80-.).* **303**, 1146 (2004).

44. Ghosal, S. *et al.* Ion Partitioning at the Liquid/Vapor Interface of a Multicomponent Alkali Halide Solution: A Model for Aqueous Sea Salt Aerosols. *J. Phys. Chem. A* **112**, 12378 (2008).

45. Brown, M. A., Winter, B., Faubel, M. & Hemminger, J. C. Spatial Distribution of Nitrate and Nitrite Anions at the Liquid/Vapor Interface of Aqueous Solutions. *J. Am. Chem. Soc* **131**, 14 (2009).

46. Steffen Oswald. X-ray Photoelectron Spectroscopy in Analysis of Surfaces. in *Encyclopedia of Analytical Chemistry, Online* (John Wiley & Sons, Ltd, 2013).

47. Yagasaki, T., Saito, S. & Ohmine, I. Effects of Nonadditive Interactions on Ion Solvation at the Water/Vapor Interface: A Molecular Dynamics Study. *J. Phys. Chem. A* **114**, 12573 (2010).

48. Archontis, G. & Leontidis, E. Dissecting the stabilization of iodide at the air-water interface into components: A free energy analysis. *Chem. Phys. Lett.* **420**, 199 (2006).

49. Caleman, C., Hub, J. S., Van Maaren, P. J., Van Der Spoel, D. & Levitt, M. Atomistic simulation of ion solvation in water explains surface preference of halides. *PNAS* **108**, (2011).

50. Otten, D. E., Shaffer, P. R., Geissler, P. L. & Saykally, R. J. Elucidating the mechanism of selective ion adsorption to the liquid water surface. **109**, 21 (2012).

51. Dor Ben-Amotz. Interfacial solvation thermodynamics. *J. Phys. Condens. Matter* **28**, 414013 (2016).

52. Wang, Y., Sinha, S., Desai, R., Jing, H. & Das, S. Ion at Air−Water Interface Enhances Capillary Wave Fluctuations: Energetics of Ion Adsorption. *J. Am. Chem. Soc* **140**, 9 (2018).

Chapter 5

Ion Adsorption at Water-Surfactant Interfaces

5.1 Introduction

The discovery that certain anions display a preference for interfacial adsorption has catalyzed a renewed interest in the behavior of ions at aqueous interfaces. A combination of experimental[1–3] and theoretical[4,5] studies over the past two decades have engendered advances beyond the simple Onsager-Samarras picture towards a more nuanced understanding of the physics of ion adsorption at the water surface. While these studies have substantially enhanced our understanding of the interfacial dynamics of ions, a current limitation is their restriction to relatively simple systems. This is a considerable limitation, as relevant systems outside of the laboratory often comprise complex mixtures of organic and inorganic species. Contemporary understanding of ion adsorption physics provides few clues as to how the interactions in these more complicated solutions regulate surface activity of anions. For both fundamental and practical reasons, this knowledge gap must be addressed if we hope to apply knowledge gained from laboratory systems to real-world phenomena.

5.2 Amphiphiles

One class of molecules of substantial fundamental and industrial importance are amphiphiles, or surfactants. As can be seen for the model surfactant shown in Figure 5.1, amphiphilic molecules are typically composed of two portions, a hydrophilic headgroup, charged or uncharged, and a hydrophobic tail, often a long chain alkane. This combination of hydrophilic and hydrophobic regions results in the expulsion of the surfactant molecule to the air/water interface, where the molecule is energetically stabilized by having the head group interacts with the underlying water molecules while the tail points toward the vapor phase. In keeping with the discussion from Chapter 4, the addition of a surfactant to a solution results in a positive surface excess for the amphiphile and a consequent reduction of the water surface tension. Surfactant molecules are abundant in both natural as well as anthropogenic systems. Naturally-occurring surfactants include fatty acids and the phospholipids that make up the boundaries of cells, as well as some proteins. Surfactants are also critical in industrial applications, where they are used as flotation agents in ore refining[6,7], in agriculture[8,9] and in the synthesis of nanostructures, like quantum dots and nanoparticles[10–13]. Surfactants are also important in modern medicine where they are used as tools for drug delivery [14,15].

As we will discuss in the next few sections, there exist compelling reasons to study the interaction of aqueous ions with surfactant-covered interfaces. Understanding how ions interact with amphiphilic films is of critical importance for both extending our understanding of the physics of ion adsorption, as well as furthering our knowledge of chemistry occurring at these interfaces.

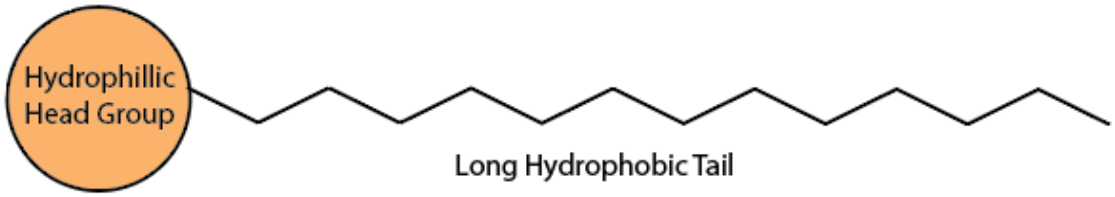

Figure 5.1: Model of a surfactant molecule. The surface activity for the molecule is a result of the hydrophilic head group and hydrophobic tail.

5.2.1 Fundamental rationale for studying ions at surfactant interfaces

The effects of amphiphile monolayers on the adsorption of ion to the interface are of special interest, given recent advances in our understanding of the physics of anion adsorption at the air/water surface. Increasingly, the importance of water-water interactions is being recognized in the thermodynamics of ion adsorption at the interface. In the model developed by Otten et al, there exists a favorable enthalpic component resulting from the return of undercoordinated surface water molecules and weakly-held ion solvent shell molecules to the bulk of solution, which is balanced against a negative entropic contribution, assigned to the pinning of capillary waves as the ion moves to the interface[4]. The energies involved in driving the ion to the interface are thus a delicate balance between the enthalpic and entropic effects, and the resulting free energy minimum for these surface-active ions is shallow, with the net adsorption free energy being favorable by only a few kJ/mol[16–18]. As a main driving force for the ion adsorption in the Otten et al. model is the high energy of the water molecules at the outermost surface water layers, it can be predicted that the addition of surfactant, which will interact with these interfacial waters and potentially alter their energy, might result in changes in the propensity for surface adsorption. Indeed, sum frequency generation studies of water covered with surfactant monolayers show changes in the vibrational peaks in O-H stretching regions, implying strong hydrogen bonding interactions between water molecules and the surfactants at the interface[19,20]. SFG spectra of water in the presence of the negative surfactant SDS, for instance, show complete loss of the free OH peak, which in the neat water spectrum, originates from surface waters with one of their OH bonds pointing out of the solution towards the vapor[19,21]. As such, it can be predicted that the enthalpic driving force that typically drives ions to the interface may be reduced in the presence of a surfactant or perhaps absent entirely. The presence of a surfactant monolayer may also be expected to alter the entropic contribution for anion surface adsorption. Surfactants decrease the surface tension of solution and are known

to increase the damping of capillary waves by altering the viscoelastic properties of the surface[22], although the damping effect has dependence on the homogeneity of the monolayer[23,24]. Experiments measuring the thermodynamics of adsorption at the surfactant-covered interface might then be expected to reveal changes in the thermodynamics of ion adsorption, perhaps even observing the complete suppression of the ion populations at the interface. Such experiments would provide a good test for the surface adsorption model proposed by Otten et al, as well as other models of ion surface affinity. The results would also serve to help resolve the ongoing controversy regarding the pinning or enhancement of capillary waves at the interface[4,25] after anion adsorption. By studying the thermodynamics of adsorption in the presence of the surfactant, we may thus be able to refine our understanding of the forces that affect adsorption of ions at interfaces.

5.2.2 Role of surfactants in atmospheric chemistry

Beyond questions about the fundamental physics of ion adsorption, there are important practical reasons to study the effects of surfactants on adsorption processes. Chief among these is the critical role ions at the interface play in regulating atmospheric chemistry. As has been discussed previously, reactions involving ions residing at aerosol air/water interfaces play an important role in shaping atmospheric chemistry, being essential in processes such as the depletion of ozone at arctic sunrise[26,27] , generation of bromine- and iodine-containing compounds in the atmosphere[2,28], and the reactive uptake of nitric acid[27,29,30]. As such, the heterogenous chemistry that takes place at the air/particle interface has received a great deal of experimental attention in the past few decades.

Surfactants have long been recognized to be of critical importance in regulating chemistry at the surface of aerosol particles. Studies of cloud condensation nuclei have determined that these aerosols contain 10% or more organic compounds by mass, most of them in the form of amphiphilic compounds at the interface[31,32]. Most of these amphiphilic molecules coating the aerosol are of biological origin, resulting from the breakdown of cell-derived fatty acids in the terrestrial oceans[32]. Measurements of the uppermost ocean surface have found that it is highly enriched in these byproducts of biological decomposition[33]. Wave action at the ocean surface results in the fragmentation of these organic enriched layers, generating droplets with large organic fractions. These surfactant-rich aerosols display an inverse micelle-like structure, with a concentrated brine core and thick organic outer shell. Long chain carboxylic acids are a key component of these outer films, with the most common carboxylic acid constituents being stearic and palmitic acid[32]. These organic films play an important role in regulating chemistry occurring at aerosol surfaces. The organic layers affect atmospheric reactions by limiting the diffusion of gas-phase components into aerosols, changing the solubility for atmospheric components, and absorbing UV radiation to regulate photochemistry[30,32,34]. Based on our current understanding of the physics of ion adsorption, we propose that these surfactants may play another role in atmospheric chemistry-by regulating the affinity for ions at the aerosol surface. If the population of ions at the interface of aerosols is affected by the presence or composition of these organic coatings, this could present an important controlling factor in the atmospheric chemistry occurring at the surface of these particles. However, given the fact that ion enhancement at the air/water interface is a relatively new field of study, there have been few

experiments that have characterized the roles of these organic layers on the heterogenous ion chemistry at the aerosol interface. Better understanding of these features is thus critical for better modelling of atmospheric processes.

5.2.3 Ion adsorption to amphiphilic interfaces in biological systems

Interaction between ions and amphiphiles also have important implications in biology, wherein the cell membrane is composed of amphiphilic phospholipids in the form of a bilayer. Both simulations and experiments on anion interaction with lipid membranes have shown Hoffmeister-like effects for the interaction of anions with such lipid bilayer[35–37]. In molecular dynamics simulations carried out on halide interactions with DOPC membranes[35], it was found that the penetration depth for the various halides increased with increasing anion size, with iodide found to approach closest to the membrane for the three anions studied. The authors of the study speculated that the mechanism that drives this ordering might be akin to that which causes the anions to adsorb to the air/water interface. However, unlike at the air/water interface, none of the anions simulated in the study showed a surface enhancement relative to bulk. It is possible this lack of surface enhancement was a result of the non-polarizable model used in the simulation. In a second set of molecular dynamics simulations carried out to study the interaction of halides with phosphatidylcholine membranes, more definite evidence for ion-specific effects was found[36]. In that simulation, the chloride anion demonstrated only an electrostatic attraction to the water/membrane interface as a result of the surface-bound sodium counterions. When the counterion was changed to potassium or cesium, both of which exhibit lower binding affinities to the membrane, the surface affinity of the chloride was lost. In contrast, Iodide was found to bind to the membrane in the presence of all simulated cations, implying an ion-specific interaction between the larger halide and the head groups of the membrane. The authors attributed the ion-specific effects to a combination of differences in anion size, polarizability and pairing effects with the choline groups of the membrane. Lipid lamella have also been found to show specific ion effects which follow the Hofmeister-like trends. Petrache et al. carried out small-angle x-ray scattering experiments characterizing the swelling of DLPC lamella in the presence of chloride and bromide anions. In the experiments, additional swelling of the lamellar structure was observed in bromide solutions as compared to chloride[38]. This additional swelling was attributed to ion-specific binding of the bromide to the phospholipid/water interface, which results in greater electrostatic repulsion between the lamellar layers. The findings of these experiments and simulations suggest that better understanding of the ion-specific interactions between amphiphiles and ions in solution could be very important for better understanding cellular biology and transport phenomena.

5.2.4 Previous experimental studies

As was previously discussed, current understanding of the physics of ion adsorption at interfaces implies that surfactants could alter the thermodynamics of surface adsorption via their ability to form hydrogen bonds at the interface and their ability to alter water surface tension. These effects serve to influences both the enthalpic and entropic components of free energy of adsorption, potentially lowering the surface affinity of the anions and limiting their availability for reaction at the air/water interface. Only a few experiments have set out to measure the impact of surfactant monolayers on the adsorption of ions at the air/water interface, and the

results of these studies show discrepancies that make the role played by the surfactant unclear. Onorato et al. characterized the adsorption of the thiocyanate anion to an air/water interface coated with a monolayer of dodecanol via resonant second harmonic generation. By fitting the resultant isotherms with a Langmuir isotherm model, these authors were able to extract the free energy of adsorption for the anion, which was found to be identical to that for adsorption to the neat air/water interface. This result implied that the addition of the alcohol to the solution surface had little impact on the surface thermodynamics of the thiocyanate adsorption[16]. it remains unclear why so drastic a change at the interface should have so little effect.

In contrast, ambient pressure x-ray photoelectron spectroscopy experiments carried out by Krisch et al. to study iodide at the butanol-coated air/water interface found the alcohol to have a significant effect on the surface concentration of the anion[39]. In the absence of the surfactant, an enhancement in the I/Na signal ratio was observed in the XPS spectra. In previous XPS studies of halides at the air/water interface, such enhancements have been interpreted as evidence for preferential interface adsorption of the anion. When a butanol monolayer was added to the salt solution, the enhancement of the iodide relative to the counterion was suppressed, although the absolute signal levels still showed that significant amounts of the anion resided on the surface. Molecular dynamics studies of this system found that addition of the alcohol resulted in the flattening of both the surface population peak for the iodide and the subsurface population of sodium, with both ions having a surface concentration similar to their concentrations in the bulk. The change in the surface population was attributed to direct interaction between the ions and the hydroxyl head of the surfactant, which was buried in the solution. As can be seen by the conflicting results of these two studies, the role of surfactants in regulating ion surface populations remains unclear.

5.3 Resonant Second Harmonic Generation at the Surfactant Interface

To better understand the effects of adding surfactant to the air/water interface, we carried out a series of experiments employing resonant second harmonic generation spectroscopy to directly probe ion adsorption at the air/water interface covered by the three representative surfactants: stearic acid, dodecanol and cetyltrimethylammonium bromide, the structures of which are shown in Figure 5.2. Second harmonic generation is ideal for this experiment, as it offers unparalleled interface specificity, with a penetration depth predicted to be ca. 10 Å[40]. Furthermore, by exploiting the strong CTTS transition of the thiocyanate anion, the experiment can directly probe the ion population at the solution interface. Measurement of the SHG signal intensity of the SHG response from the sample solution as a function of bulk anion concentration and the application of a Langmuir adsorption model permits the thermodynamics of ion adsorption to the surfactant covered interface to be extracted from the data.

5.3.1 The CTTS transition

To use second harmonic generation as a direct probe of the ion in solution, we exploit the property of resonant enhancement in the SHG process. As noted previously, the intensity of the

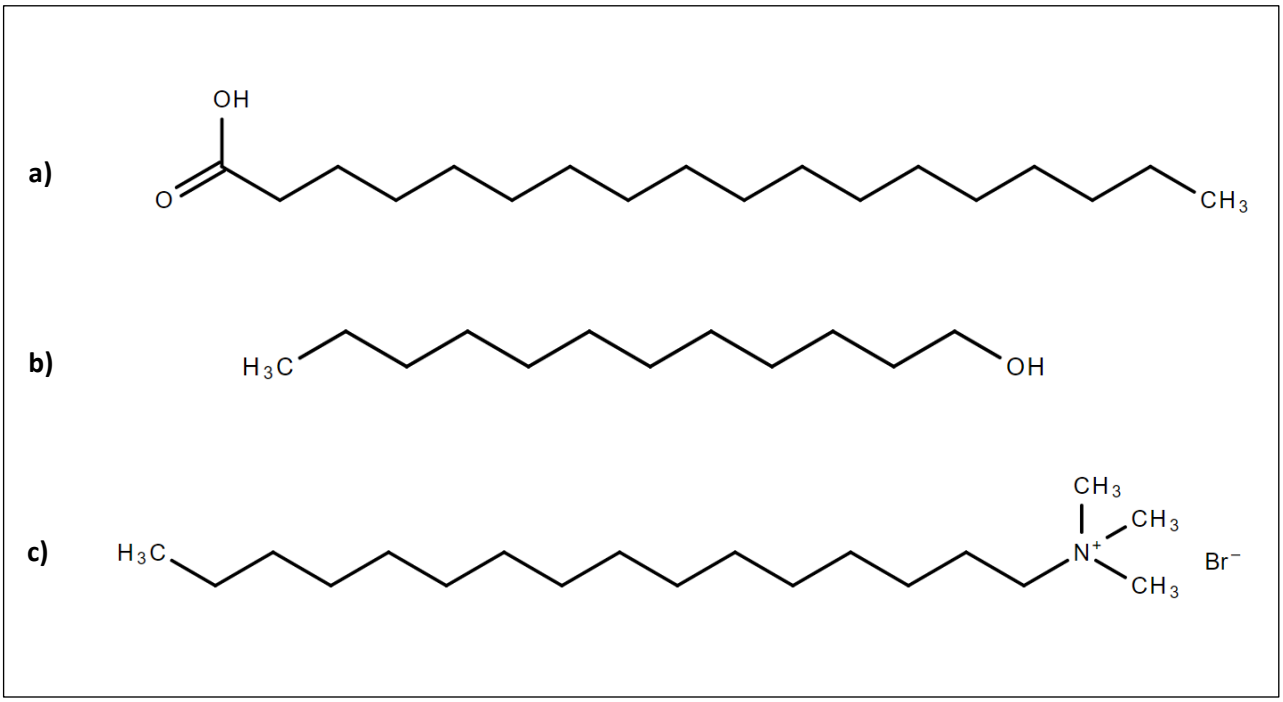

Figure 5.2: Structures of the three surfactants employed in this study **a)** Stearic acid **b)** Dodecanol and **c)** Cetyltrimethylammonium bromide

measured second harmonic is dependent on the square of the input laser intensity and to the $\chi^{(2)}$ second order susceptibility, which can be written as:

$$\chi^{(2)} \propto \frac{\mu_{gb}\mu_{be}\mu_{eg}}{(\omega_{eg} - \omega_1 - i\Gamma)(\omega_{eg} - 2\omega_1 - i\Gamma)} \qquad (5.1)$$

Here the values in the numerator are the transition dipoles for the transitions between the ground, intermediate and final states, ω_{eg} is the frequency of an electronic transition in the anion, Γ is related to the state lifetime, and ω_1 and $2\omega_1$ are the fundamental and second harmonic frequencies respectively. As can be seen in Equation 5.1, when either the fundamental wavelength or its second harmonic is resonant with a transition in the molecule, the denominator approaches zero and consequently the value of $\chi^{(2)}$ increases in magnitude. The measured second harmonic intensity is therefore greatly enhanced whenever this resonance condition is fulfilled. We can exploit this property to not only increase the measured second harmonic intensity in the experiment, but to directly probe the ion at the interface by tuning either the

fundamental or second harmonic to be resonant with a transition in the ion of interest. The relationship between $\chi^{(2)}$ and the ion population can alternatively be written as:

$$\chi^{(2)} = N\beta \qquad (5.2)$$

Here N is the number of ions in the optical probe spot and β is the molecular hyperpolarizability for the ion of interest. As such, by exploiting the resonant enhancement, we can directly probe the population of the species of interest at the sample interface. For this reason, the resonant approach to the analysis of ion population is greatly preferred over other non-linear optical approaches, e.g. electric field induced second harmonic, wherein the interfacial population for the ions must be inferred from modelling of the changes in the non-resonant water signal.

The principal anion used in the present study is thiocyanate, the structure of which is depicted in Figure 5.3. For the thiocyanate anion, the chosen transition is the charge transfer to solvent (CTTS) band, which occurs in the deep UV at wavelengths near 200 nm.

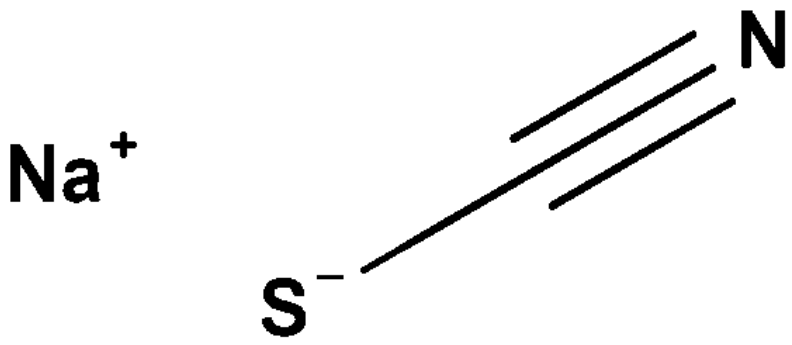

Figure 5.3: Structure of sodium thiocyanate, the primary salt used in the SHG experiments described in this chapter

Figure 5.4 shows the bulk UV/visible spectrum for a sodium thiocyanate solution. The CTTS transition is a broad, intense and featureless transition that involves the ejection of an electron from the anion to the surrounding solvent shell. As such, the transition is highly sensitive to the dynamics and structure of the nearby solvent. In past non-linear optics experiments this sensitivity to the surrounding has even been exploited as a probe of the solvation environment at the interface[41]. In the experiments discussed in this chapter, as we measure at only a single input wavelength, we choose to use the CTTS transition simply to exploit the exceptional strength

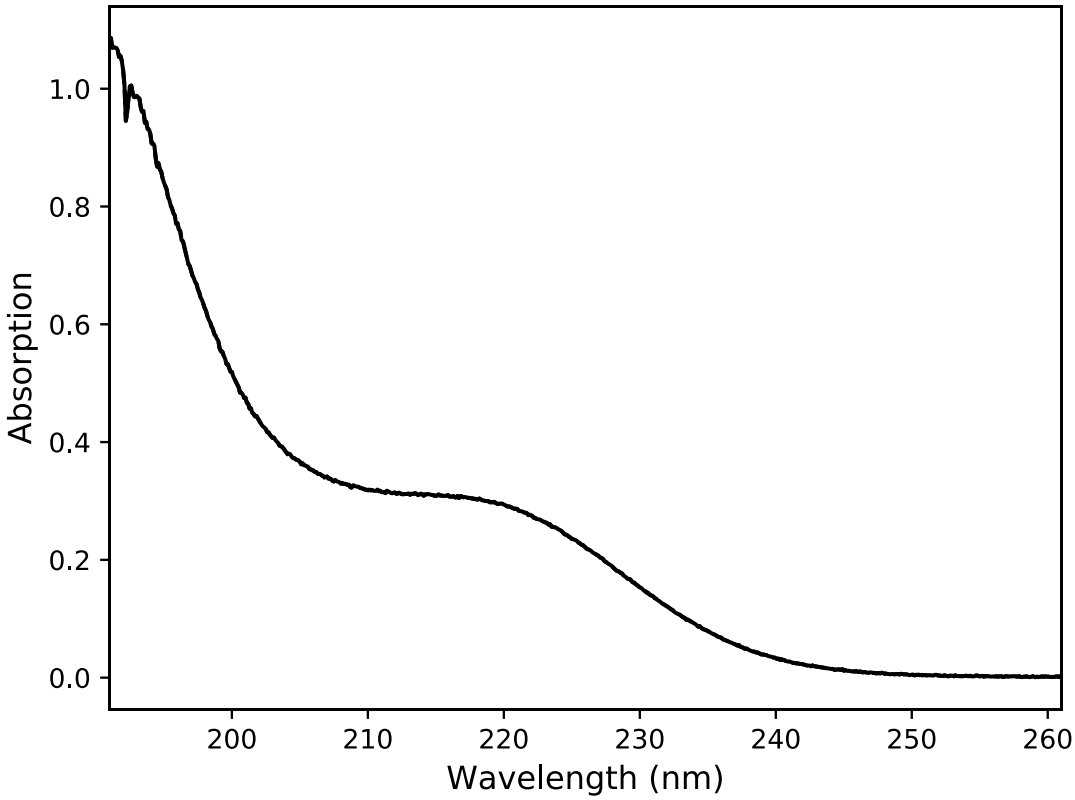

Figure 5.4: CTTS transition for bulk thiocyanate. The increase in absorption below 240 nm is the onset of the transition.

of the transition. As is detailed in Equation 5.1, the value of $\chi^{(2)}$ under resonant conditions is related to the transition dipole for the electronic transition, hence, resonance with a more intense transition result in a larger resonant enhancement effect.

Because the equilibrium ion population at the surface is dependent on the bulk concentration, the SHG signal increases as the anion bulk concentration grows. By observing the changes in the signal as a function of the solution concentration, an adsorption isotherm for the anion can be constructed and the free energy of adsorption to the interface can be obtained. We discuss our adsorption model and how the thermodynamics of the adsorption are extracted in the next section.

5.3.2 Langmuir isotherm fitting model

In our resonant SHG experiments, we measured adsorption of the anion by observing the second harmonic signal intensity from the interfacial ions as a function of the bulk concentration of the thiocyanate. The thermodynamics of anion adsorption are derived from fitting of the

resulting isotherm. The relationship between the measured SHG signal and the free energy of adsorption at the interface for the anion can be derived in the following manner[42]. We start with the expression for the intensity of the second harmonic response, which can be written as:

$$I_{SHG} \propto \left|\chi^{(2)}\right|^2 I^2 \qquad (5.3)$$

Here $\chi^{(2)}$ is the effective second order susceptibility for the sample and I is the input intensity of the fundamental laser pulse. $\chi^{(2)}$, the effective susceptibility for the system, can itself can be expanded as:

$$\chi^{(2)} = N_{water}\beta_{water} + N_{ion}\beta_{ion} \qquad (5.4)$$

Here we have separated out the contributions from the water from those from the anions. The β_i terms are the hyperpolarizabilities of the respective species in solution and N_i is the number density of each species at the interface. The hyperpolarizability for the thiocyanate can be further split into real and imaginary components due to the resonance condition with the CTTS transition in the anion:

$$\beta_{ion} = \beta_{real,ion} + i\beta_{im,ion} \qquad (5.5)$$

Combining Equations 5.3,5.4, and 5.5, it can be seen that the measured SHG signal is dependent on the number of ions at the interface as follows:

$$\frac{I_{SHG}}{I^2} \propto \left|N_{water}\beta_{water} + N_{ion}(\beta_{real,ion} + i\beta_{im,ion})\right|^2 \qquad (5.6)$$

$$\frac{I_{SHG}}{I^2} \propto \left(N_{water}\beta_{water} + N_{ion}\beta_{ion,real}\right)^2 + \left(N_{ion}\beta_{ion,im}\right)^2 \qquad (5.7)$$

All that remains is to relate the surface population for the ion, N_{ion}, to the bulk concentration of the solution. We do so through application of the Langmuir isotherm. We begin by assuming equilibrium between ions in the bulk and ions at the interface, described by equilibrium constant K as follows:

$$SCN_{bulk} + water_{surf} \leftrightarrow SCN_{surf} + water_{bulk} \quad (5.8)$$

$$K = \frac{SCN_{surf} water_{bulk}}{SCN_{bulk} water_{surf}} \quad (5.9)$$

Assuming $SCN_{surf} + water_{surf} = N_{max}$, some maximum number of available surface adsorption sites at the interface, the equilibrium in Equation 5.9 can be rewritten as:

$$K = \frac{SCN_{surf} water_{bulk}}{SCN_{bulk}(N_{max} - SCN_{surf})} \quad (5.10)$$

Rearranging to isolate SCN_{surf}, we find:

$$SCN_{surf} = N_{max} \frac{SCN_{bulk}}{water_{bulk} K^{-1} + SCN_{bulk}} \quad (5.11)$$

Finally, we use the relationship between the equilibrium constant K and the Gibbs free energy of adsorption at the interface:

$$K = e^{\frac{-\Delta G_{ads}}{RT}} \quad (5.12)$$

Substituting the relation for SCN_{surf} back into the expression for the SHG intensity Equation 5.7, we find that the relationship between the second harmonic intensity and the bulk concentration can be written as:

$$\frac{I_{SHG}}{I^2} = \left(A + B \frac{SCN_{bulk}}{water_{bulk}\, e^{\frac{\Delta G_{ads}}{RT}} + SCN_{bulk}} \right)^2 + \left(C \frac{SCN_{bulk}}{water_{bulk} e^{\frac{\Delta G_{ads}}{RT}} + SCN_{bulk}} \right)^2 \quad (5.13)$$

Here we have introduced constants A,B, and C describing proportionality between the concentration and the observed signal intensity. In introducing A, we have assumed that the water concentration at the interface does not appreciably change as the thiocyanate ions adsorb. As the signal from water is an order of magnitude lower than the signal from the SCN, due to the resonance with the CTTS transition, even if this assumption were invalid it should not have much impact on the resulting interpretation. By fitting the experimentally-derived adsorption isotherm to this four-parameter fitting model, the free energy of adsorption ΔG_{ads} can be extracted for the thiocyanate anion.

5.3.3 Experimental design

The experimental design of the second harmonic generation experiments is depicted in Figures 2.5 and 2.6. Ultrafast 800 nm 100 fs laser pulses were first generated by a Mai Tai titanium:sapphire oscillator operating at an 80 MHz pulse repetition rate. The output pulses from the oscillator were then used to seed a Spitfire chirped pulse regenerative amplifier, which produced amplified 800 nm, 130 fs laser pulses with a repetition rate of 1 kHz. Pulses exiting the regenerative amplifier passed into a TOPAS optical parametric amplifier (OPA), which allowed for tuning of the probe to the desired experimental wavelengths. For all the experiments described in this chapter, the SHG probe wavelength was set to 386 nm so that the second harmonic, located at 193 nm, coincided with the CTTS transition for the thiocyanate anion. As the position of the CTTS transition is sensitive to the solvation shell of the ion, which differs at the interface relative to the bulk, the absorption spectrum at the interface can differ from that of the bulk[41]. The 193 nm wavelength utilized in the experiment was chosen because it corresponds to high laser output power from the OPA and because in previous experiments it has been shown to yield a strong second harmonic signal[16,43].

After exiting the OPA, the maximum power of the 386 nm laser pulses was adjusted by directing the pulse through a set of neutral density filters. Maximum laser pulse power was decreased as the bulk solution concentration rose due to an increased propensity to form laser-induced photoproducts at high thiocyanate concentrations. After transmission through the static N.D. filters, the probe laser pulses passed through a motorized variable neutral density filter. As the filter wheel rotated, the probe laser power was continuously modulated between zero and the power maximum set by the static N.D. filters. Measurement of the SHG intensity across the entire range of powers facilitated more accurate measurement of the SHG signal. The pulse power after the rotating N.D. was then measured for every laser shot using a 1% beam splitter and photodiode. An example input pulse power trace resulting from modulation of the input power is depicted in Figure 5.7. After power measurement, the input beam was focused onto the sample surface using a 100 mm focal length CaF_2 lens, producing an on-sample spot size of ~100 μm in diameter.

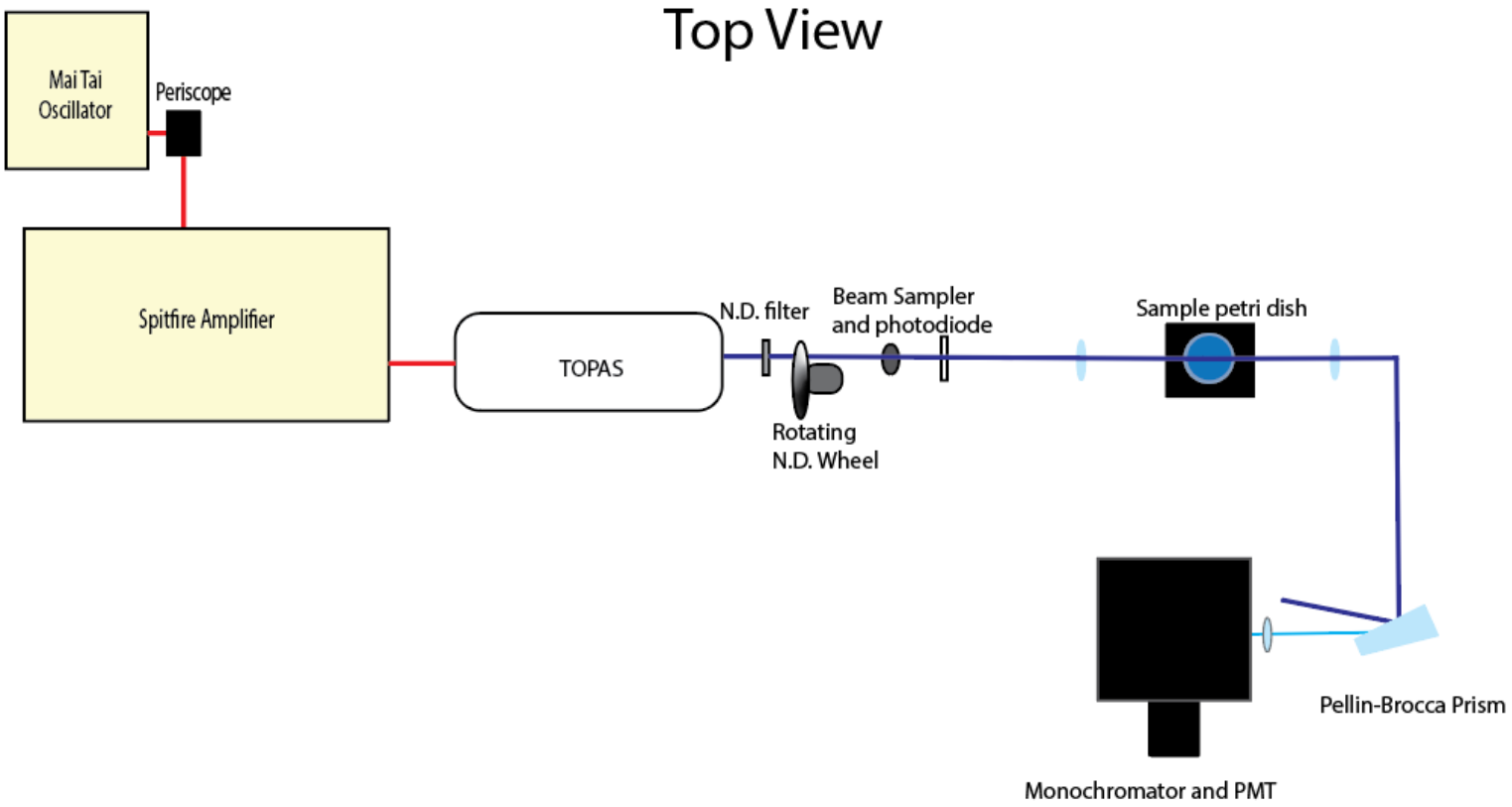

Figure 5.5: Top view of experimental set-up for SHG experiments

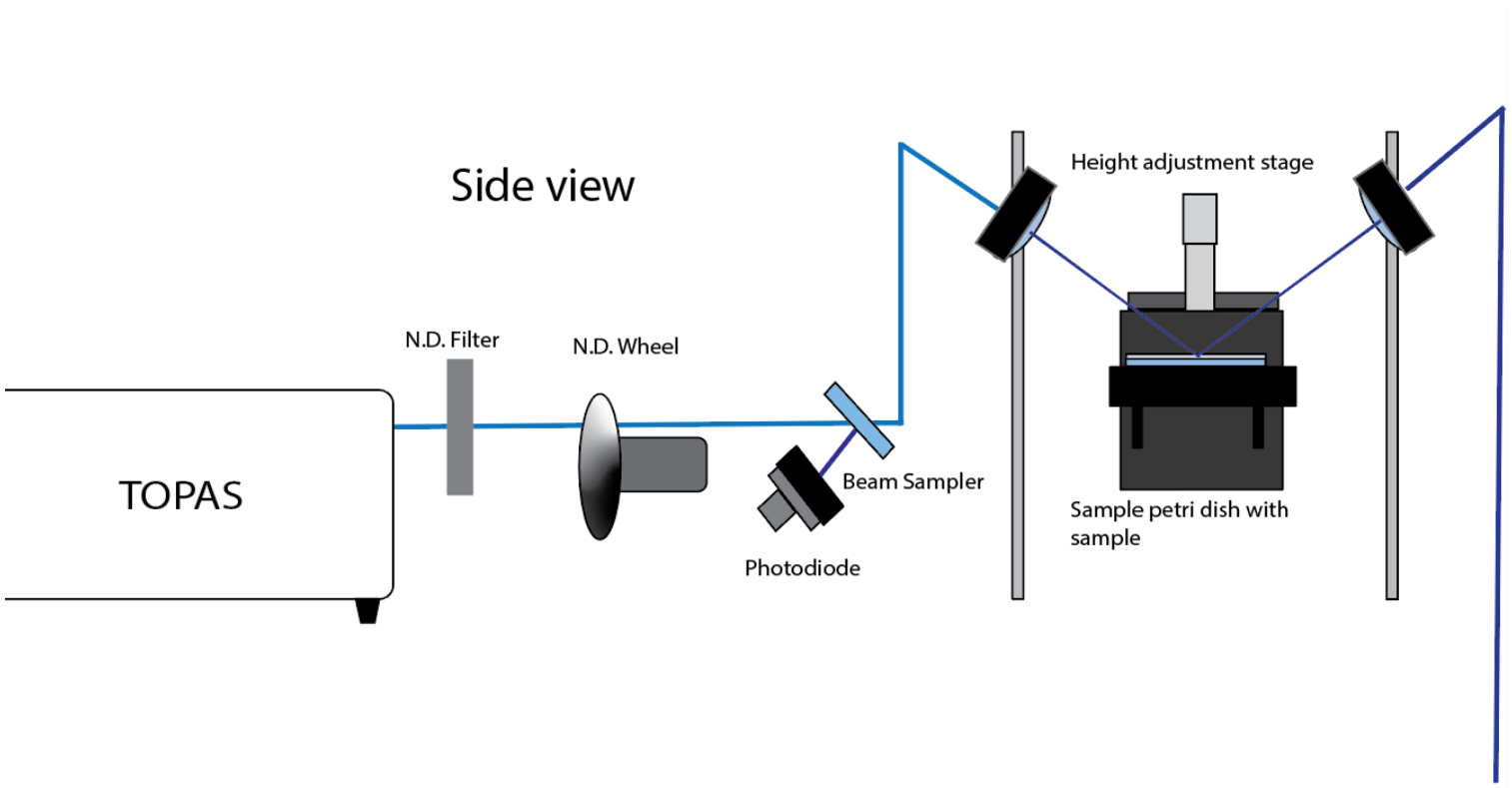

Figure 5.6: Side view of experimental set-up for SHG experiments

.

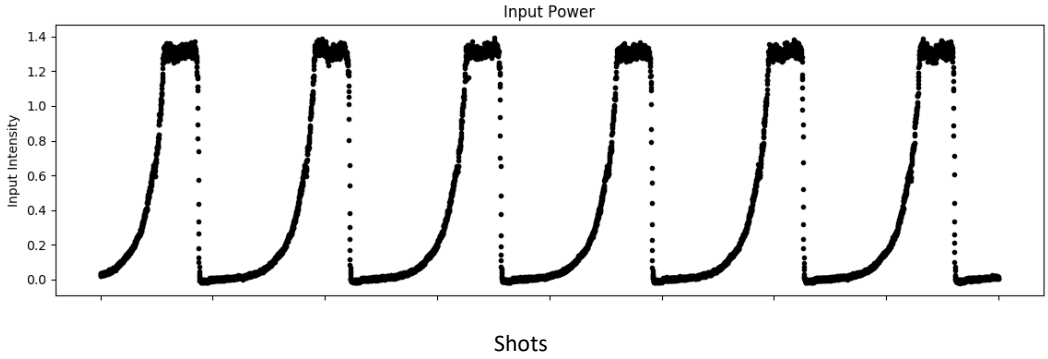

Figure 5.7: Signal trace from the photodiode, showing the modulation of the input power. As the motorized filter rotates, it modulates the input laser power between the set maximum and zero.

The samples themselves were solutions of sodium thiocyanate prepared in Pyrex glass petri dishes with concentrations ranging from 0.1 - 3M. A vertical translation stage under the sample dish permitted the sample height to be adjusted to ensure that the solution surface was always in the beam focus.

The SHG intensity measurements were carried out in reflection geometry, as shown in the figure. After reflecting from the sample surface, the beam was recollimated by a second 100 mm focal length CaF_2 lens. The fundamental and colinearly propagating second harmonic were then spatially separated via a Pellin-Brocca prism, with the fundamental beam directed into a beam dump while the second harmonic photons were focused into a monochromator and PMT for measurement. The intensity of the second harmonic signal for each concentration was measured using custom-written software. The measured signal was binned according to the input intensity and a line was fit to a plot of signal intensity vs input power squared. The slope of this fit line is proportional to $\chi^{(2)}$ and was taken as the intensity for each measured concentration. The second harmonic intensity for each concentration was normalized to the signal from pure water with a monolayer of the respective surfactant studied, which allowed for day to day fluctuations in the power and laser system alignment to be normalized out. The analysis procedure for the second harmonic intensity is detailed further in Appendix A. The sodium thiocyanate salt used in the experiment was supplied by J.T. Baker and was of reagent grade to ensure maximum purity. Sodium iodide and sodium bromide salts were also used in the experiment and were both 99% reagent grade purity supplied by Sigma Aldritch. All salts employed in the experiment were baked in an oven overnight at 200° C before solutions were made to remove any adsorbed organics which might obfuscate the experiment. The three surfactants used in the present experiments (stearic acid, dodecanol, and

Cetyltrimethylammonium bromide) were also supplied by Sigma Aldritch and were of reagent grade, 98% purity or better. High-purity water for preparing the solutions was supplied by a Millipore Milli-Q system and had a measured resistivity of 18 MΩ and total organic carbon content below 4 ppb. As contamination can significantly affect the results of resonant second harmonic experiments, great care was taken to remove all organic contaminants from the glassware used in the measurements. The Petri dishes, beakers and other implements employed in the experiment were all thoroughly cleaned by soaking overnight in a Nochromix/sulfuric acid solution, a strong oxidizing agent which served to remove all potential organic contaminants.

5.3.4 Formation of the surfactant monolayers

Stearic acid

Stearic acid monolayers were created via two different methods. In the first, following examples from the literature,[44] the stearic acid was initially dissolved in pentane to create a saturated oil/acid solution. Thiocyanate solution was added to the sample Petri dish, and then 45 microliters of the oil/acid solution was spread onto the thiocyanate solution surface using a micropipette. The sample was then allowed to equilibrate for five minutes, which allowed the pentane to evaporate and leave behind a monolayer of the stearic acid at the surface of the solution. A volume of 45 µL was chosen because it was the point at which lensing was seen on the solution surface upon the addition of more stearic acid solution, indicating successful formation of a full monolayer. The second method for forming the monolayers in the experiment involved simply adding a small piece of stearic acid crystal directly to the Petri dish after it had been filled with NaSCN solution. This second method was used as a control experiment, as we will discuss later; it remains unclear whether monolayers were successfully formed in this approach.

Dodecanol

For the formation of the dodecanol monolayers, we again used a procedure taken from the literature.[16] For each experiment, a small piece of solid dodecanol was added to the prepared thiocyanate solution and five minute were allowed to elapse while the alcohol spread on the surface. A variety of different waiting times, from 3-15 minutes, were tested and the results were not found to depend on waiting time; as such, five minutes was deemed to be sufficient for the experiments.

Cetyltrimethylammonium bromide

For the preparation of cetyltrimethylammonium bromide (CTAB) monolayers, the CTAB was co-dissolved with the thiocyanate in the solution flask. Due to the low solubility of CTAB in water, the solution flasks were sonicated for one minute after the surfactant was added to ensure complete dissolution of the CTAB. The concentration of CTAB in the experiments was kept to 10 µM to ensure that it remained below the critical micelle concentration of 1 mM[45]. The prepared NaSCN/CTAB solutions were added to the sample petri dishes and the SHG signal was measured after a few minutes to allow for the monolayer to equilibrate.

5.4 Effects of Surfactants on Thiocyanate Adsorption

5.4.1 Stearic acid

As previously discussed, carboxylic acids like stearic acid are known to be important contributors to the organic shells of aerosol particles in the atmosphere. In order to better understand the effects of such organic shells on interfacial chemistry, we begin our study by examining the impact that the addition of stearic acid has on the adsorption of thiocyanate anions. Figure 5.8 shows both the input laser intensity and SHG signal traces for a 1 M solution of sodium thiocyanate in the absence of a stearic acid monolayer. The data presented in the traces are typical for a thiocyanate solution of intermediate concentration. The bottom trace shows the variation in the input power due to the modulation by the motorized N.D. filter, while the top trace shows the corresponding second harmonic signal intensity. Each spot on the SHG signal trace represent the arrival of a second harmonic photon at the detector. As would be expected, the arrival of signal photons at the detector corresponds to periods of high input intensity for the laser.

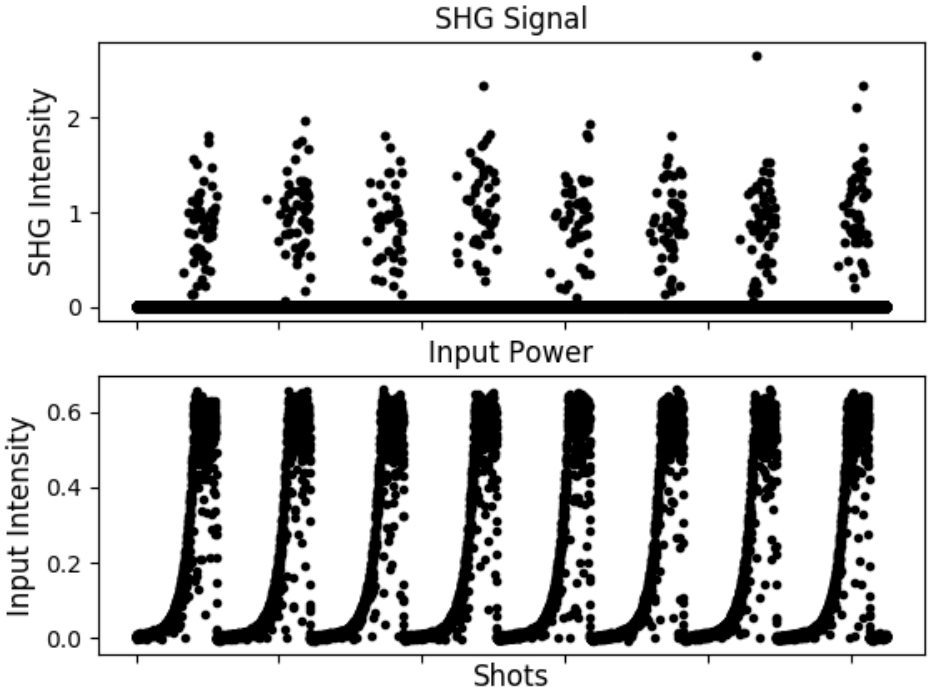

Figure 5.8: Input power and SHG intensity traces for a 1M NaSCN solution in the absence of a stearic acid monolayer. Data shown comprise the first 10000 shots of the 60000 total shot experiment. The data trace in the figure is typical for thiocyanate at 1M concentration.

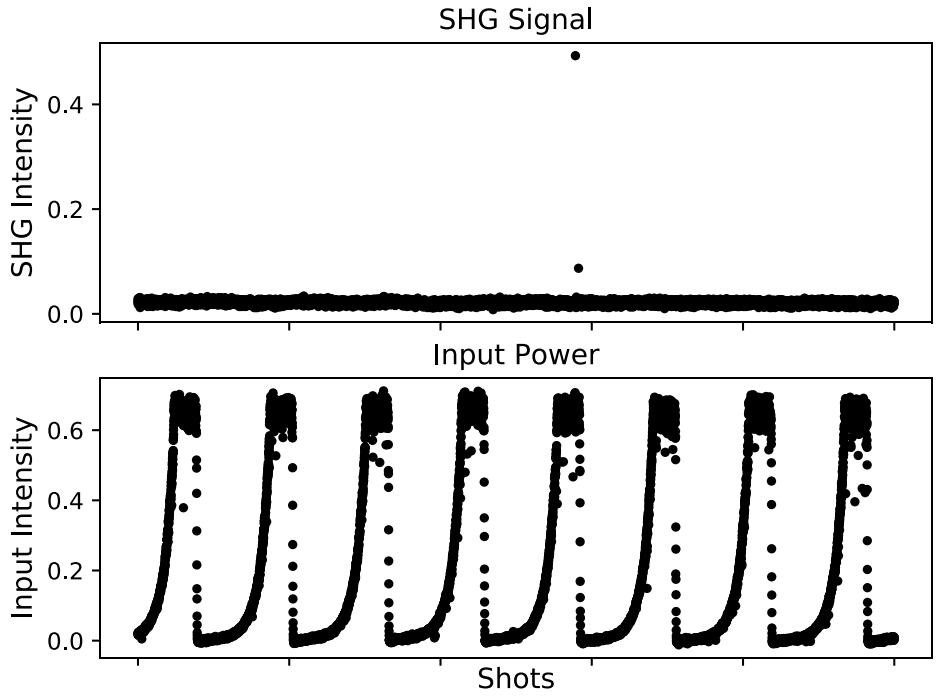

Figure 5.9: SHG and reference traces for 1M NaSCN in the presence of a stearic acid monolayer. As can be seen, the presence of stearic acid completely suppresses the second harmonic signal generated from the thiocyanate anions.

In contrast, Figure 5.9 shows the same results for a 1 M solution after the addition of a monolayer of stearic acid. While the input laser intensity is the same for both Figure 5.8 and Figure 5.9, the derived second harmonic signal is nearly entirely suppressed after the formation of the stearic acid monolayer. In the experiments with the added stearic acid, only a few photons are measured to reach the detector, and from power studies of the arriving signal it is clear that most of this signal can be attributed to either noise or stray light. Even when the maximum power of the probe was increased, there was no detectable second harmonic intensity from the solutions with added stearic acid. As discussed previously, the resonant SHG signal in the experiment is directly related to the surface population of the thiocyanate anions. Therefore, the observed loss of signal implies that the presence of stearic acid resulted in the thiocyanate ions being driven away from the interface, rendering them invisible to the SHG probe.

To further explore this apparent loss of thiocyanate population at the surface, the SHG signal from the solution was measured as a function of the added stearic acid. By systematically varying the amount of the oil/stearic acid solution added to the sample, the effect of the stearic acid on thiocyanate adsorption at sub-monolayer coverage could be quantitively assessed. Figure 5.10 shows the second harmonic signal as a function of the amount of stearic acid solution added to the interface. For each point in the figure, the signal intensity is normalized to the intensity in the absence of the stearic acid monolayer. At sub-monolayer surface coverages, the strength of the second harmonic signal from SCN^- at the interface was found to be highly variable, as can be seen from the large error bars in Figure 5.10.

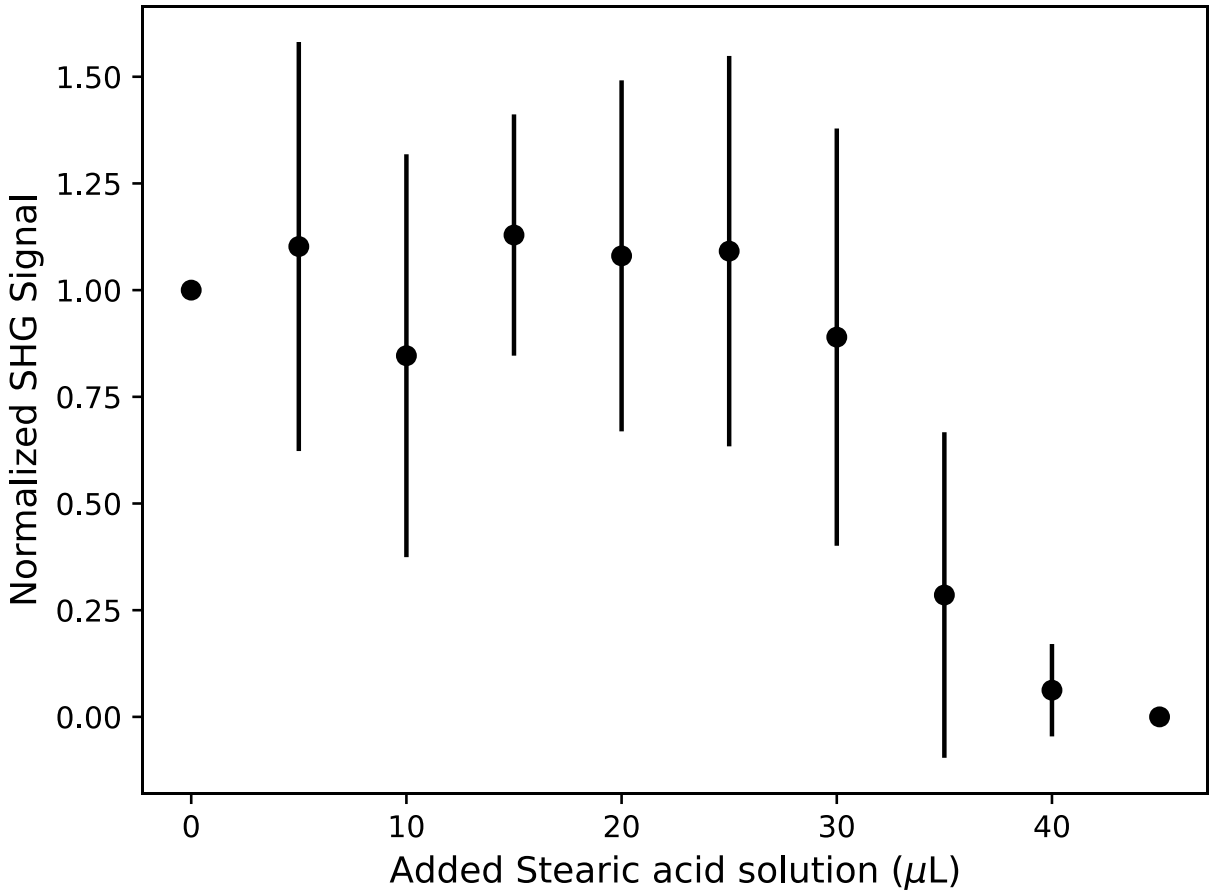

Figure 5.10: SHG intensity as a function of the amount of stearic acid added. As can be seen, there is significant error for values below 35 µL. The trace exhibits a simple on/off behavior. For added oil solution below ~35 µL the measured signal is near that of the surface without stearic acid on average. After the addition of 35 µL, however, a rapid loss of SHG signal intensity is observed. 35 µL of added oil corresponds to formation of a complete monolayer, as observed by lensing at the solution surface.

Looking just at the signal average, as coverage increases, the SHG intensity shows a simple on/off behavior for thiocyanate in the presence of stearic acid at the interface. For added stearic acid solution below 35 µL, the average normalized SHG signal intensity is near 1, identical to that of the neat solution. As previously noted, SHG intensity in this low coverage regime displayed an unusually large uncertainty. The same amount of stearic acid added sometimes decreased the measured SHG signal by only a few percent, while other experiments resulted in the almost complete quenching of the measured signal. For added stearic acid of 35µL or more, there was consistently an abrupt drop in SHG intensity to zero. The abrupt change in the signal intensity coincides with the visual appearance of lensing as more stearic acid is added, signaling complete monolayer coverage

This uncertainty in the SHG signal combined with the on/off behavior, made it difficult to quantitively study the system at sub-monolayer coverages and provided little insight into the origin of the loss of thiocyanate SHG signal in the presence of the acid. It is likely that the origin of this inconsistency in the SHG intensity at sub-monolayer coverage results from the structure of the stearic acid monolayer on the solution surface. Electron microscopy studies of stearic acid films have shown that it has a patchwork-like nature composed of two-dimensional stearic acid aggregates separated by empty space[46]. It is therefore likely that, rather than spreading uniformly, the surfactant is instead forming small islands on the solution surface. If these islands, which slowly diffuse across the sample surface, have a domain size on the order of the laser spot size, then it would explain the inconsistency observed for sub-monolayer coverage, viz. the measured SHG intensity would be dependent on whether one of these stearic acid islands was present in the beam spot at the time of measurement. To test this hypothesis, experiments were performed wherein the same sample dish was measured at time points several minutes apart after the addition of the acid. From these experiments, it was observed that the measured signal did sometimes exhibit large fluctuations as a function of waiting time, randomly increasing or decreasing in intensity. The same changes in intensity changes were also seen when the sample dish was manually agitated between measurements. As such, the uncertainty in the sub-monolayer SHG intensity was very likely a result of the random motion of surfactant islands on the sample surface.

We next investigated the origin of the signal loss in the presence of the surfactant. To ensure that the loss of signal observed in the experiment was not a result of the acid monolayer absorbing the outgoing SHG photons, the signal from pure water was measured with and without the addition of a stearic acid monolayer. In these experiments with water, the presence of the stearic acid monolayer resulted in a modest *increase* in the water SHG signal. The observed rise is likely an electric field induced second harmonic (EFISH) effect resulting from a small population of carboxylate anions in the monolayer. The presence of a DC field at the interface, like that generated by a charged surfactant, serves to break the centrosymmetric in the solution bulk on a length scale of the solution screening length. This results in a deeper probe depth for the SHG experiment[47,48]. As the probe depth increases, more water molecules begin to contribute to the SHG process and consequently a small intensity increase is observed. In any case, for pure water

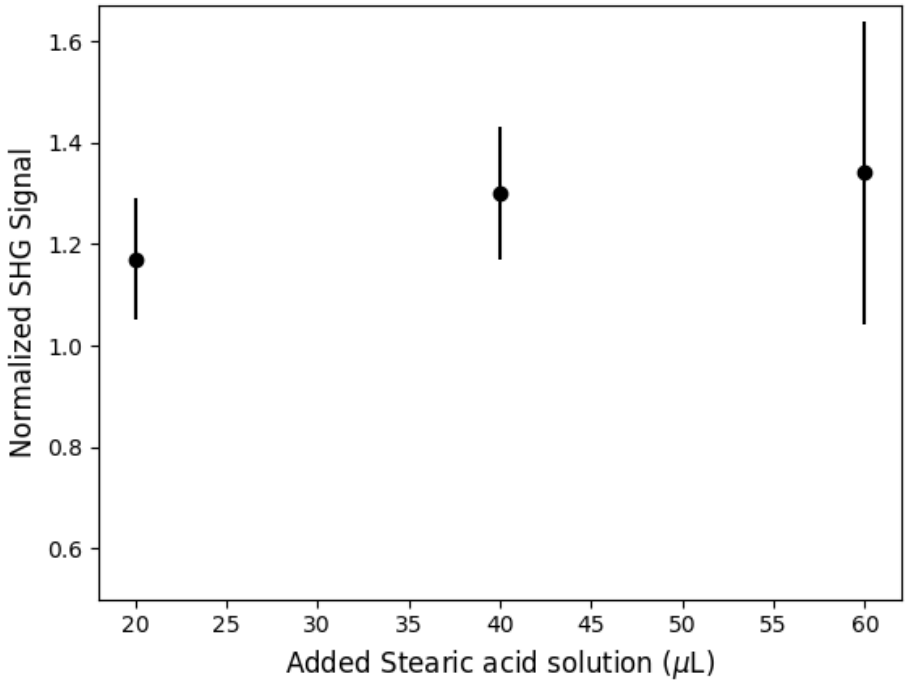

Figure 5.11: SHG intensity from pure water in the presence of differing amounts of stearic acid. The addition of stearic acid to the water surface increases signal by ~20-30% due to an EFISH effect.

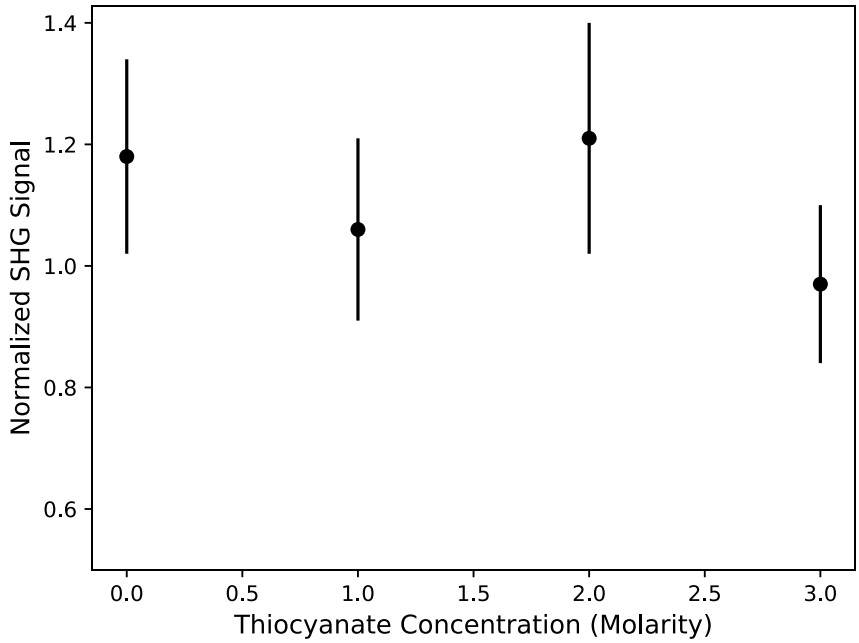

Figure 5.12: SHG signal from thiocyanate solutions of varying concentrations after the addition of 35 µL pentane. Data normalized to SHG intensity in the absence of pentane. The effect of the oil on the SHG signal is a modest increase.

with a stearic acid monolayer we find no evidence for a decrease in the SHG intensity that might be associated with absorption of the outgoing SHG photons by the surfactant. As such, absorption of the UV second harmonic photons by the stearic acid monolayer can be ruled out as source for the observed loss of signal from the thiocyanate solutions.

As a second control, the effect of the pentane used as a spreading agent for the stearic acid was also investigated. In these experiments, the oil without any dissolved stearic acid was spread on sodium thiocyanate solutions and the effect on the measured SHG intensity was observed. Figure 5.12 shows the SHG signal, normalized to its value in the absence of the oil, for three different thiocyanate concentrations of 1,2, and 3 M after 45 µL of pure pentane was spread on the surface. As can be seen, the effect of pentane on the signal intensity is modest, and while there is some uncertainty in the measured values, we do not observe complete loss of the SHG signal when the oil is added to the interface. From this control experiment, it was clear that the observed loss of signal when the stearic acid solution was spread on the surface was almost certainly a result of the presence of the carboxylic acid. We now discuss the possible mechanisms through which the ions might be excluded from the interfacial region in the presence of the carboxylic acid monolayer.

One likely possibility for the depletion of the thiocyanate from the interface in the presence of stearic acid is simple electrostatic repulsion. Some fraction of the stearic acid molecules residing at the surface will be in their deprotonated carboxylate form. Therefore, it should be expected that the interface acquires some degree of negative charge, which would serve to repel the like-charged thiocyanate ions. Indeed, the modest increase seen in the signal from pure water seems to imply at least some degree of surface charging occurs upon addition of the acid. However, one can argue that this mechanism cannot account for the complete loss of signal observed in the experiment. Previous studies have demonstrated that for short chain carboxylic acids, the neutral form of the acid is preferentially adsorbed at the surface over the carboxylate, due to the high energetic cost of placing a charged group in the vicinity of the interface[49]. Additionally, molecular dynamics simulations, as well as non-linear optics experiments , have found consistent evidence for the air/water interface being acidic[50–52]. As a result of these effects, the acid/base equilibrium near the interface should favor the protonated form over the carboxylate and the degree of surface charging should expected to be relatively small, although obviously non-zero. Finally, any charging that did occur at the interface should be screened out relatively quickly. The screening length for a 1M solution can be estimated from the Debye length as ~1 nm, about the probe depth of the SHG experiment. Therefore, the thiocyanate anions are still expected to reside near the surface, even in the presence of some interfacial charge, and signal from these should thus be measurable. In light of these considerations, it seems likely that effects other than simple electrostatic repulsion are involved in the observed complete loss of SHG signal from the thiocyanate solutions. Some of the change might certainly be due to the previously discussed thermodynamic effects resulting from changes in the surface water energy. To disentangle the electrostatic contribution from the thermodynamic effects, we measured the effect on the SHG signal of the uncharged surfactant-dodecanol.

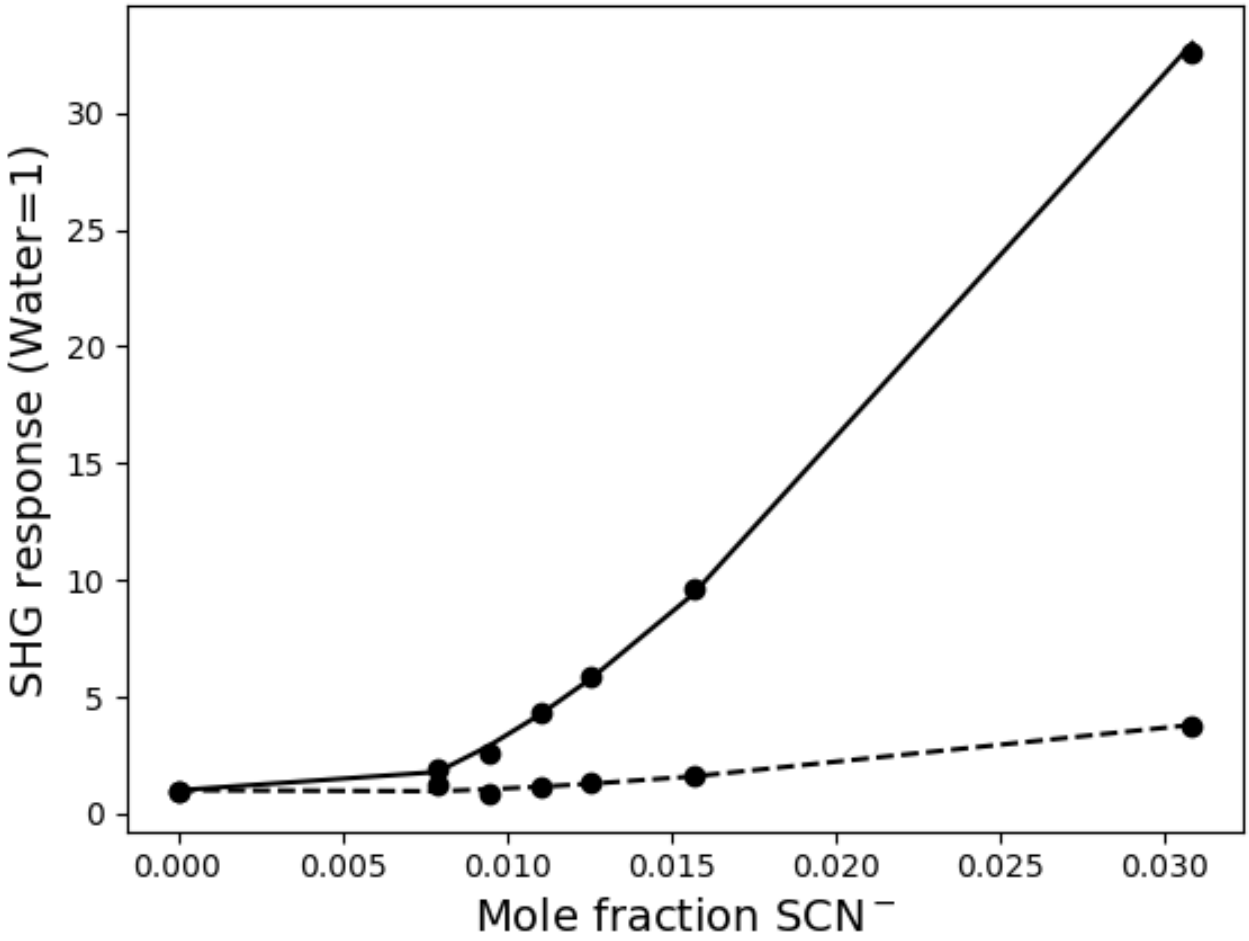

Figure 5.13: SHG intensity as a function of concentration for dodecanol solution. Solid line is the value in the absence of dodecanol while the dashed line shows the signal intensity after the addition of the alcohol. As can be seen, the addition of the dodecanol results in a significant decrease in the observed SHG intensity.

5.4.2 Dodecanol

To better understand the impacts of the surfactant head group's charge on the surface affinity of the thiocyanate, a second set of experiments was carried out using the long chain alcohol dodecanol as the surfactant. Unlike in the experiments with stearic acid, second harmonic signal from the thiocyanate remained at a measurable level even in the presence of the dodecanol monolayer. Figure 5.13 shows the adsorption isotherm for SCN with (dashed line) and without (solid line) a monolayer of dodecanol at the interface. For each concentration point in the isotherm the solution was run twice, once in the absence of the surfactant and then again after the long chain alcohol was added. This allowed for a direct comparison of the effect of the alcohol on the signal intensity. Control experiment in which a surfactant-free solution was run twice showed no significant differences between runs and we expect no artifacts in the data as a result of using the same sample twice in the experiment. As can be seen from Figure 5.13, the measured SHG intensity was seen to decreases dramatically after addition of the dodecanol layer.

As with the stearic acid, the possibility that the signal decrease was a result of absorption by the monolayer was tested by measuring the SHG signal from water with an added dodecanol. In these experiments there was no observed change in the signal from the water, implying the intensity loss seen in the experiments with thiocyanate is not a result of absorption of the SHG photons. As such, the loss in SHG signal intensity must result from a decrease in the SCN population at the surface in the presence of the alcohol. Despite the obvious change in the surface population after the addition of the alcohol, the free energies of adsorption derived from the Langmuir model fits were found to be identical for the thiocyanate in both the presence and absence of the added alcohol. The best fit free energies for the adsorption isotherm in the absence of dodecanol was found to be -6.0±.42 kJ/mol while for the solutions with the dodecanol monolayer a fit adsorption free energy of -6.2±.50 kJ/mol was measured. The free energy of adsorption for thiocyanate adsorption to the dodecanol interface found in this study was in good is in agreement with that measured in previous resonant SHG studies[16], as can be seen in Table 5.1.

Experiment	ΔG_{ads} for thiocyanate
This study (no dodecanol)	-6.0±.42 kJ/mol
This study (dodecanol added)	-6.2±.5 kJ/mol
Literature (Reference 53)	-6.7±1.1 kJ/mol

Table 5.1: Value for free energy of adsorption to the dodecanol coated interface

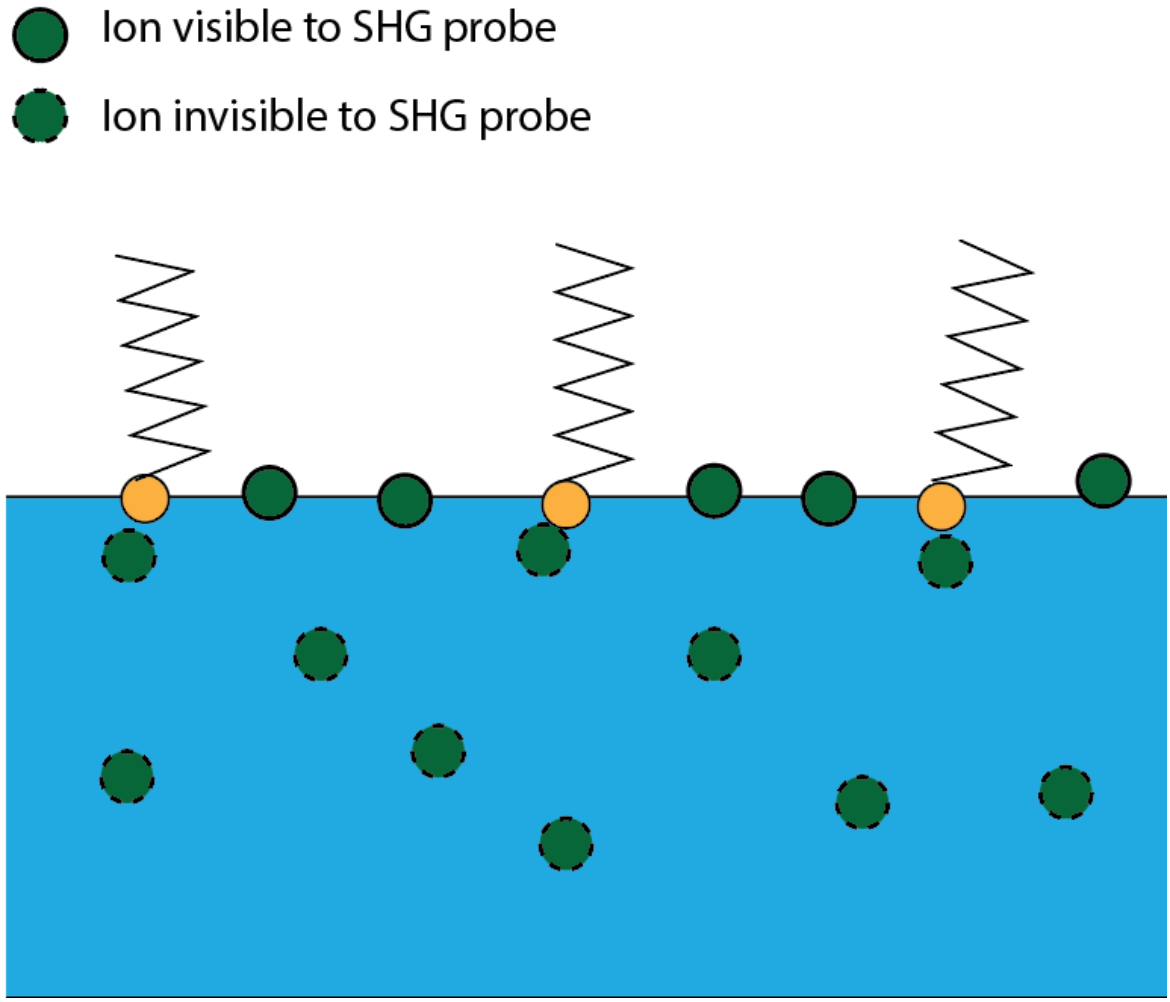

Figure 5.14: Mechanism for surface population loss without change in the adsorption free energy. The surfactant molecules serve to block adsorption sites at the interface. Ions in the solution bulk or those interacting with the surfactant head groups (dashed) are buried deeper into the solution and are rendered invisible to the probe. Ions at unblocked sites at the interface (solid) do not interact with the surfactant and adsorb in the same manner as they do in the absence of the alcohol. For these unblocked sites the free energy of adsorption is identical to that for the neat water surface.

The finding that the fit free energy remains unchanged after the addition of an amphiphilic alcohol agrees with previous SHG studies of ion adsorption to dodecanol monolayers but is seemingly at odds with the results obtained by Krisch et al. in their ambient pressure XPS experiment. As discussed previously, experiments carried out by Krisch et al. found significant changes in both the iodide surface population and the surface structure of the ions after the addition of a long chain alcohol to the air/water interface. In the model proposed in the Krisch, the presence of the alcohol resulted in the migration of the iodide deeper into the solution, where it could directly interact with the head groups of the alcohol. While we do observe a loss of thiocyanate population at the interface in this study, we do not observe any difference in the free energy in the presence or absence of the alcohol, implying the adsorption mechanism for the thiocyanate visible to the SHG probe remains unchanged after the surfactant is added. The fact that we observe no change in the surface adsorption thermodynamics may be a result of a mismatch between the 'site' density for ion adsorption at the interface and the packing density of the dodecanol monolayer. Given the measured surface density of dodecanol at saturation is ~$1x10^{-9}$ mol/cm^2 [53], the surface density for the dodecanol at maximum coverage is ~1 molecule/nm^2. As such, even if there is direct interaction between the thiocyanate anion and the alcohol head group, there still remain open surface sites where thiocyanate anions can adsorb in the same manner as in the absence of the surfactant, as is shown in Figure 5.14. To test this theory, it would be helpful in the future to conduct studies in a Langmuir trough, where the exact packing density of the surfactant at the interface can be controlled. If the difference in site density is indeed an important factor in determining the ion interfacial population, the SHG intensity should vary as the monolayer is compressed. This is something we hope to further investigate in the future.

As a final control, the impact of the monolayer formation method on the anion surface affinity was tested. To do so we attempted to form stearic acid monolayers using the same method as employed in the formation of the dodecanol monolayers, adding small crystals of the stearic acid to the thiocyanate solution and allowing time for the acid to spread and equilibrate. Curiously, the samples prepared in this manner did not display the same loss of signal as was observed in the more traditional manner of stearic acid monolayer preparation discussed earlier. SHG signal intensity from the thiocyanate was still detectable and an adsorption isotherm for the anion was successfully measured, as displayed in Figure 5.15. The free energy derived from the Langmuir isotherm fit, shown in Table 5.2, of -7.15±.31 kJ/mol is typical for a stearic acid solution in the absence of a surfactant, again implying there are no changes in the energetics on addition of the dodecanol. However, for this manner of monolayer formation it remains unclear whether an actual monolayer of the acid was successfully formed. A search of the literature found no precedent for forming stearic acid monolayers in this way. We hope to take surface tension measurements in the future to determine whether the acid forms a monolayer when added to the solution in such a manner.

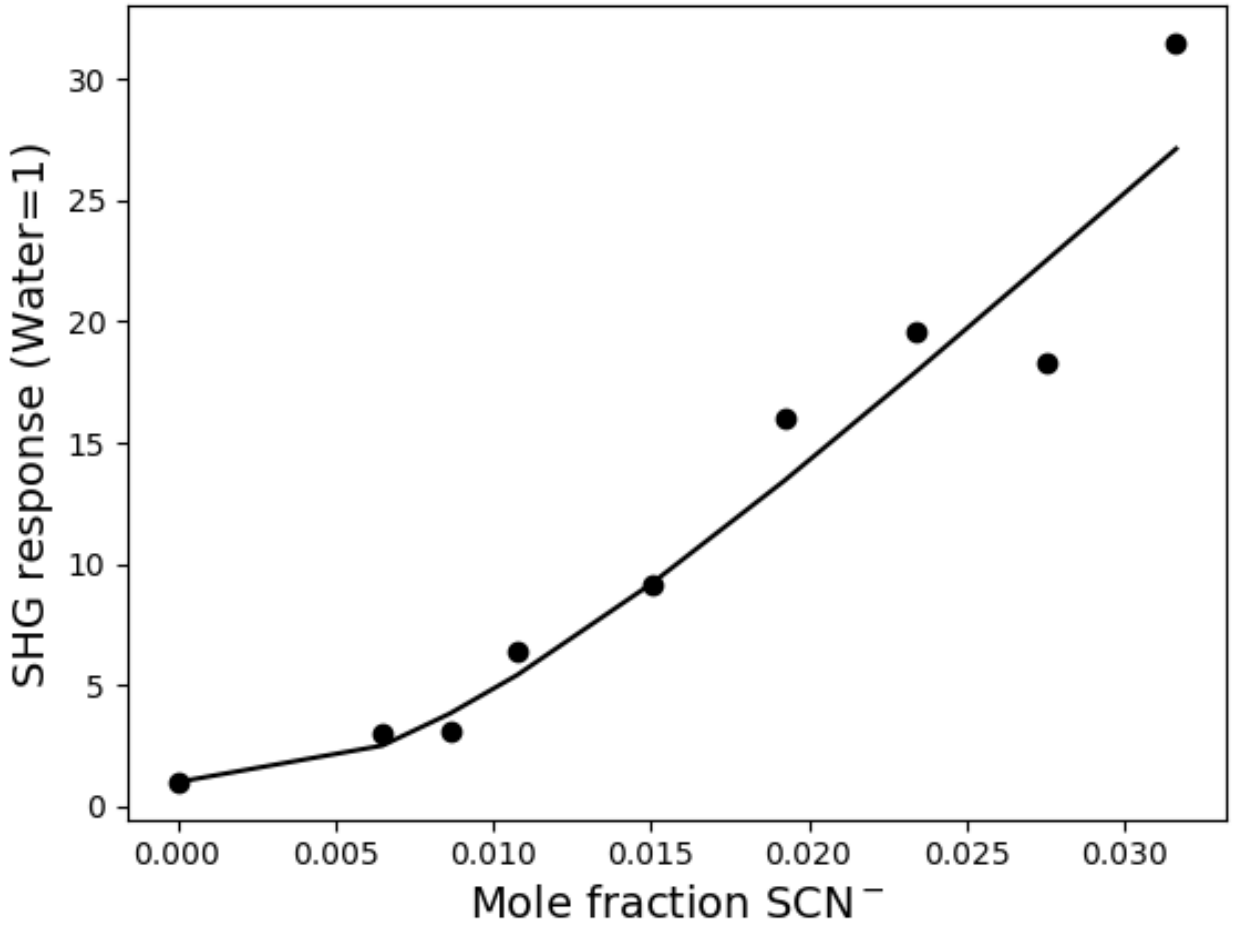

Figure 5.15: SHG intensity as a function of concentration for stearic acid layers formed by the addition of a stearic acid crystal to the sample solution. The measured free energy of -7.15±.31 kJ/mol is typical for that of thiocyanate adsorption to the bare air/water interface. It is unclear in this system, however, whether a stearic acid monolayer was formed successfully.

System	Fit free energy
NaSCN/Stearic acid	-7.15±.31 kJ/mol
Neat SCN (Ref. 17)	-7.53±.13 kJ/mol

Table 5.2: Free energy for Stearic acid monolayer vs. the neat interface

To conclude, the effects of stearic acid vs. dodecanol on thiocyanate adsorption to the interface are markedly different. The addition of a dodecanol monolayer acts to reduce the total amount of thiocyanate bound at the surface but seems to have no impact on the thermodynamics of the ion adsorption. This is likely a result of the dodecanol monolayer failing to block all the available adsorption sites at the air/water interface even at full monolayer coverage. In contrast, the addition of stearic acid monolayers results in complete suppression of the surface activity of the thiocyanate ions. It is likely the more complete suppression of ion adsorption seen for the stearic acid stems from an additional electrostatic contribution from deprotonated carboxylate anions at the surface. This results in a coulombic repulsion term which serves as an additional barrier for the approach of the negatively charged thiocyanate to the interface. To further explore the site blocking effects of the dodecanol it will helpful to conduct future studies using a Langmuir trough, where the surface structure of the surfactant can be more fully controlled. However, the impact of the surface charge at the interface can be further investigated by carrying out SHG experiments using a surfactant of known charge, as we will discuss next.

5.4.3 Cetyltrimethylammonium bromide

To further explore the role of charge at the interface and its effect on ion adsorption affinity, we carried out another set of experiments with monolayers of the positively charged surfactant Cetyltrimethylammonium bromide (CTAB). Given the positive charge of the CTAB amide head group, if electrostatic effects were strongly affecting the ion adsorption, a large enhancement of the thiocyanate SHG signal should be observed after the addition of the surfactant. Figure 5.16 shows the measured SHG signal from a 100 μM sodium thiocyanate/CTAB solution. As can be seen in the figure, there is indeed a very large second harmonic signal seen in the data trace. Such strong signal from the thiocyanate at micromolar concentrations is highly unusual given that, in the absence of the positively charged surfactant, the experiment usually requires thiocyanate concentrations on the order of 1M to observe measurable second harmonic intensity. The unusually large signal from these low concentration solutions was initially attributed the electrostatic attraction of thiocyanate to the now positively charged interface. However, it was found that the second harmonic signal enhancement from the CTAB/thiocyanate solutions showed no dependence on the thiocyanate bulk concentration in the solution. It was also observed that when the bulk thiocyanate concentrations approached ~1M a precipitate was formed in solution after the addition of the CTAB to the sample flask.

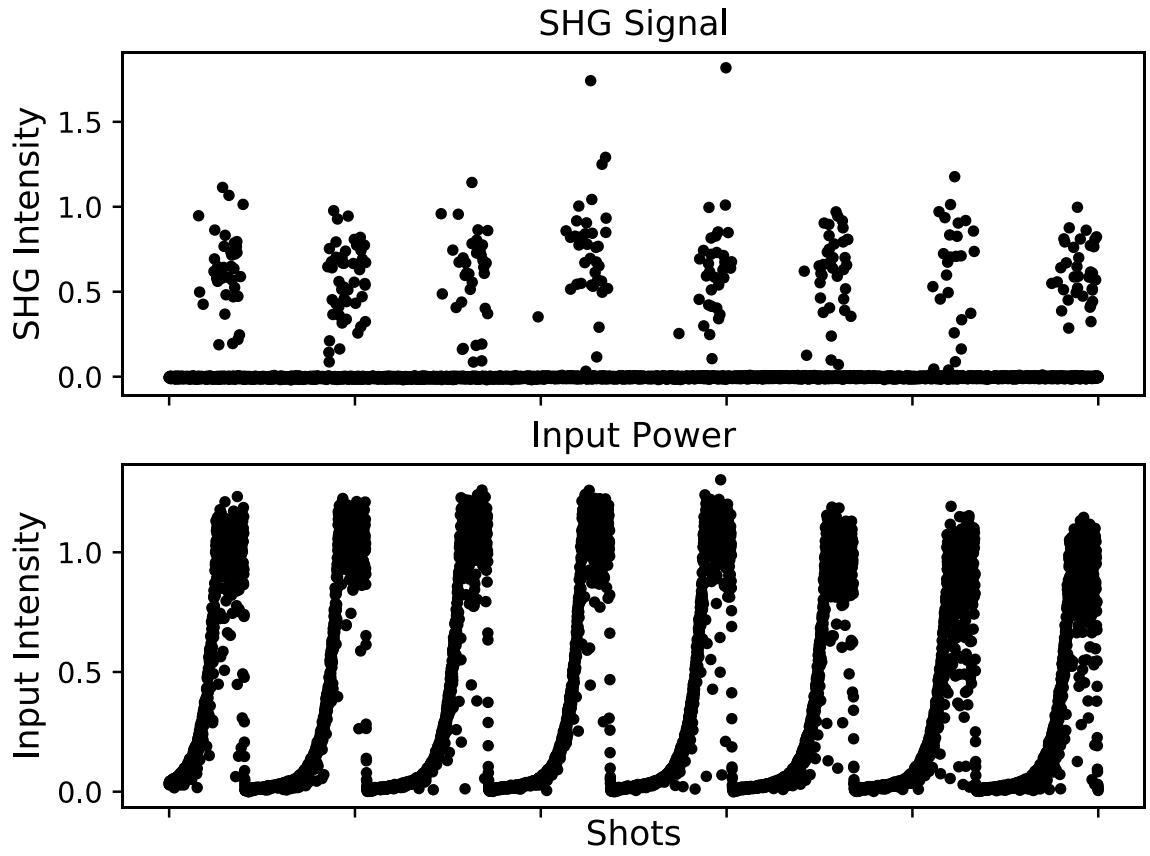

Figure 5.16: SHG signal from a solution of 100 µM NaSCN co-dissolved with 10 µM CTAB. The strong signal seen in the trace is unusual for such a low solution concentration. The strong signal is a result of ion paring between SCN^- and CTA^+.

A search of the literature revealed that CTASCN salts are known to have very low solubility in water and that CTA^+ and SCN^- have a strong affinity for forming ion pairs in solution[54]. As such, it was hypothesized that the large signal increase observed stemmed not from electrostatic effects as initially assumed but was instead a result of the formation of CTA^+ and SCN^- ion pairs, which were then localized to the interface due to the hydrophobic tail of the CTA^+ cation. To test this theory the SHG intensity of solutions of sodium iodide and sodium bromide with added CTAB was measured. If the observed enhancement of SCN at the interface was a result of coulombic attraction of the anion to the positively charged interface, then both bromide and iodide should show the same behavior as all three anions bear the same charge. However, if ion pairing is the dominant contribution to the enhanced thiocyanate surface population, then the behavior of the bromide should differ from that of the iodide and thiocyanate. Like thiocyanate, iodide is known to show significant ion pairing with the CTA cation. Thiocyanate and iodide have been predicted to be 30% and 50% paired with CTA^+ in solution respectively[54]. Conversely, bromide shows little

propensity for pairing with the CTA^+ cations, which is why it is typically used as the counterion in water soluble CTA^+ salts. Figure 5.17 and 5.18 show the results of adding 10 µM CTAB to 200 µM sodium iodide and 3M sodium bromide solutions respectively. As can be seen in Figure 5.17 iodide indeed shows the same strong signal enhancement seen for the SCN anion in the presence of CTAB, resulting in very strong SHG signals even at micromolar concentrations.

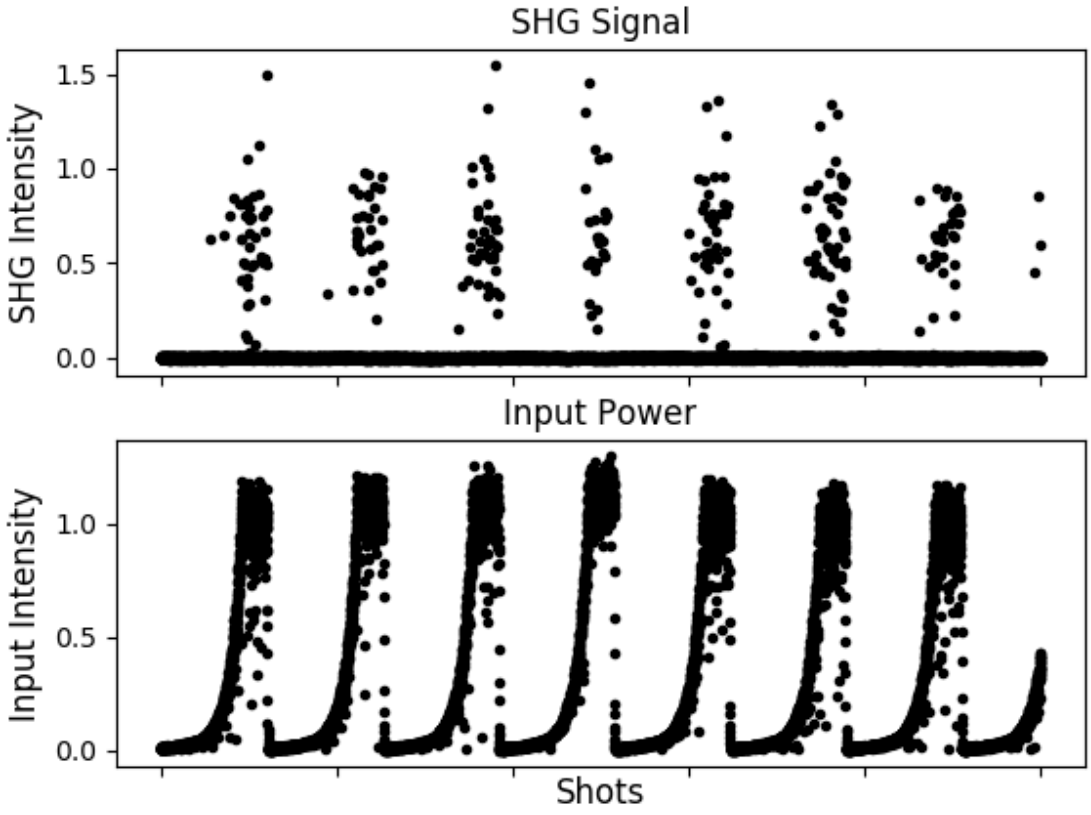

Figure 5.17: Signal from a 200 µM solution of NaI co-dissolved with 10 µM CTAB. As with the thiocyanate/CTAB solutions a large SHG signal is seen even at micromolar NaI concentrations.

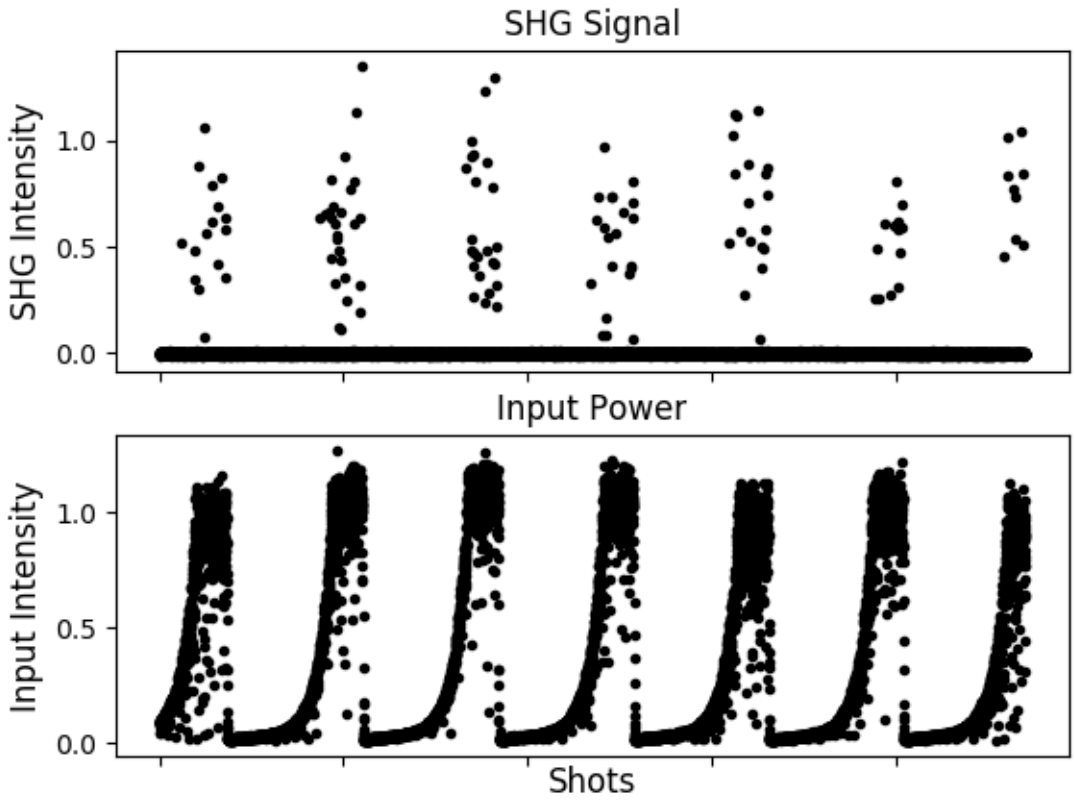

Figure 5.18: SHG signal from a 3M solution of NaBr with 10 µM CTAB. Note that it takes considerably higher bromide concentration to yield a measurable SHG signal levels as compared to SCN^- and I^- ions. This is due to weak ion pairing between bromide and the CTA^+ cation.

Conversely, the bromide solution yielded no signal at micromolar concentrations and even at a higher concentration of 3 M the measured signal from the bromide solution was only modest. As such, it can be reasonably assumed that the signal enhancement seen for both the thiocyanate and iodide salts is likely due to ion pairing rather than electrostatics effects. As the thiocyanate signal appears to be largely independent of bulk anion concentration down to micromolar concentrations, the data cannot be fit with a Langmuir isotherm to extract the adsorption free energy for the ion pairs. However, even though the thermodynamics could not be extracted in the current experiment, the CTA/SCN system may still be useful in future experiments as a model for studying ion pairing near the interface.

Conclusions

Study of ion adsorption to surfactant covered air/water interfaces is critical not only for better modelling of atmospheric reaction kinetics and industrial processes, but also for developing better understand the fundamental forces that drive ions to the interface in the absence of a surfactant. Employing resonant second harmonic generation we directly measured the thermodynamics of adsorption of thiocyanate to water surface terminated by a series of different surfactants with differing charges on the headgroup. It was observed that the addition of even an uncharged surfactant to the air/water interface resulted in the suppression of the surface population of thiocyanate ions bound at the surface. This is the result that would be expected based on our understanding of the physics of ion adsorption at the interface as described by the Otten model. The presence of the surfactant serves to lower the energy of the waters, which lessen the thermodynamic driving force for ion adsorption. However, even at monolayer coverage some ions were still observed to be bound at the interface, with an adsorption free energy unchanged from that of the neat surface. This is likely due to the fact that even at maximum packing density for the dodecanol, there still exist interfacial 'sites' not blocked by the surfactant and where adsorption can take place as normal. In the case of the atmospherically relevant surfactant stearic acid, we found that the thiocyanate's surface affinity was entirely quenched when a monolayer of the carboxylic acid was added. This finding has important implications for atmospheric chemistry occurring at the surface of aerosol particles, which are known to be coated with organic layers which include carboxylic acids. It's likely that the organic shell on these aerosols may play a more important role than was previously recognized in regulating reactions involving ions at the aerosol/air interface. Future experiments using mixed monolayers at the interface, which better mimic relevant atmospheric systems may serve to help clarify these effects and what role they play in controlling reactions at aerosol interfaces. For the positive surfactant CTAB ion pairing was observed to be the dominant effect in the solution was ion pairing, with the formed CTA/SCN ion pairs being driven to the surface by the amphiphilic nature of the CTA^+ cation. While the dominance of the ion pairing made it difficult to come to any conclusions regarding the effects of charge at the interface on the adsorption thermodynamics of anions, in the future this system may be useful for characterizing the effects of ion pairing at the interface. To better clarify the impact of charge at the interface on ion adsorption, future experiments will measure adsorption isotherms using bromide, which has a significantly lower propensity for ion pairing with the CTA^+ cation. For experiments with thiocyanate it also might be helpful to try a surfactant with a permanent negative charge, SDS for example, to help clarify the role of electrostatics in the surface affinity for the surfactant covered interface.

References:

1. Petersen, P. B. & Saykally, R. J. Evidence for an Enhanced Hydronium Concentration at the Liquid Water Surface. *7976 J. Phys. Chem. B* **109**, 7976 (2005).

2. Liu, D., Ma, G., Levering, L. M. & Allen, H. C. Vibrational Spectroscopy of Aqueous Sodium Halide Solutions and Air-Liquid Interfaces: Observation of Increased Interfacial Depth. *J. Phys. Chem. B*

108, 2252 (2004).

3. Garrett, B. C. *et al.* Electron Spectroscopy of Aqueous Solution Interfaces Reveals Surface Enhancement of Halides. *Science (80-.).* **303**, 1146 (2004).

4. Otten, D. E., Shaffer, P. R., Geissler, P. L. & Saykally, R. J. Elucidating the mechanism of selective ion adsorption to the liquid water surface. **109**, 21 (2012).

5. Jungwirth, P. & Tobias, D. J. Specific Ion Effects at the Air/Water Interface. *Chem. Rev* **106**, 1259 (2006).

6. Weng, X., Mei, G., Zhao, T. & Zhu, Y. Utilization of novel ester-containing quaternary ammonium surfactant as cationic collector for iron ore flotation. *Sep. Purif. Technol.* **103**, 187 (2013).

7. Sis, H. & Chander, S. Reagents used in the flotation of phosphate ores: a critical review. *Miner. Eng.* **16**, 577 (2003).

8. Sachdev, D. P. & Cameotra, S. S. MINI-REVIEW Biosurfactants in agriculture. *Appl Microbiol Biotechnol* **97**, 1005 (2013).

9. Castro, M. J. L., Ojeda, C. & Cirelli, A. F. *Surfactants in Agriculture*. (Springer, Dordrecht, 2013).

10. Ha, T. H., Koo, H.-J. & Chung, B. H. Shape-Controlled Syntheses of Gold Nanoprisms and Nanorods Influenced by Specific Adsorption of Halide Ions. *J. Phys. Chem. C* **111**, 1123 (2007).

11. Schramm, L. L. & Wassmuth, F. *Foams: Fundamentals and Applications in the Petroleum Industry*. (American Chemical Society, 1994).

12. Shah, S. K., Bhattarai, A. & Chatterjee, S. K. Applications of Surfactants in modern Science and Technology. *Mod. Trends Sci. Technol.* **1**, 147 (2013).

13. Bonn, D., Eggers, J., Indekeu, J. & Meunier, J. Wetting and spreading. *Rev. Mod. Phys.* **81**, 739 (2009).

14. Singh Sekhon, B. Surfactants: Pharmaceutical and Medicinal Aspects. *J. Pharm. Technol.* **1**, 43 (2013).

15. Prabhjot Kaur, Tarun Garg, Goutam Rath, R. S. R. M. & A. K. G. Drug Delivery Surfactant-based drug delivery systems for treating drug-resistant lung cancer. *Drug Deliv* **23**, 717 (2014).

16. Onorato, R. M., Otten, D. E. & Saykally, R. J. Adsorption of thiocyanate ions to the dodecanol/water interface characterized by UV second harmonic generation. *PNAS* **106**, 15176 (2009).

17. Petersen, P. B., Saykally, R. J., Mucha, M. & Jungwirth, P. Spectroscopy and MD Simulations of Sodium Thiocyanide. *J. Phys. Chem. B* **109**, 10915 (2005).

18. Petersen, P. B. & Saykally, R. J. On The Nature Of Ions At The Liquid Water Surface. *Annu. Rev. Phys. Chem* **57**, 333 (2006).

19. Truong, V. N. T., Wang, X., Dang, L. X. & Miller, J. D. Interfacial Water Features at Air−Water Interfaces as Influenced by Charged Surfactants. *J. Phys. Chem. B* **123**, 18 (2019).

20. Miranda, P. B., Du, Q. & Shen, Y. R. Interaction of water with a fatty acid Langmuir film. *Chem. Phys. Lett.* **286**, 1 (1998).

21. Satoshi Nihonyanagi, Shoichi Yamaguchi, and T. T. Direct evidence for orientational flip-flop of water molecules at charged interfaces: A heterodyne-detected vibrational sum frequency generation study. *J. Chem. Phys.* **130**, 204704 (2009).

22. Lucassen-Reynders, E. H. & Lucassen, J. Properties of capillary waves. *Adv. Colloid Interface Sci.* **2**, 347 (1970).

23. Wang, Q., Feder, A. & Mazur, E. Capillary Wave Damping in Heterogeneous Monolayers. *J. Phys. Chem* **98**, 12720 (1994).

24. Chou, T., Lucas, S. K. & Stone, H. A. Capillary wave scattering from a surfactant domain. *Phys. Fluids* **7**, 1872 (1995).

25. Wang, Y., Sinha, S., Desai, R., Jing, H. & Das, S. Ion at Air−Water Interface Enhances Capillary Wave Fluctuations: Energetics of Ion Adsorption. *J. Am. Chem. Soc* **140**, 9 (2018).

26. Spicer, C. W. *et al.* Molecular halogens before and during ozone depletion events in the Arctic at polar sunrise: concentrations and sources. *Atmos. Environ.* **36**, 2721 (2002).

27. Hunt, S. W. *et al.* Formation of Molecular Bromine from the Reaction of Ozone with Deliquesced NaBr Aerosol: Evidence for Interface Chemistry. *J. Phys. Chem. A* **108**, 11559 (2004).

28. Bernal-Uruchurtu, M. I., Kerenskaya, G. & Janda, K. C. Structure, spectroscopy and dynamics of halogen molecules interacting with water. *Int. Rev. Phys. Chem.* **28**, 223 (2009).

29. Oum, K. W., Lakin, M. J. & Finlayson-Pitts, B. J. Bromine activation in the troposphere by the dark reaction of O3 with seawater ice. *Geophys. Res. Lett.* **25**, 3923 (1998).

30. Stemmler, K., Vlasenko, A., Guimbaud, C. & Ammann, M. The effect of fatty acid surfactants on the uptake of nitric acid to deliquesced NaCl aerosol. *Atmos. Chem. Phys* **8**, 5127 (2008).

31. Li, Z., Williams, A. L. & Rood, M. J. Influence of Soluble Surfactant Properties on the Activation of Aerosol Particles Containing Inorganic Solute. *J. Atmos. Sci.* **55**, 1859 (1998).

32. Ellison, G. B., Tuck, A. F. & Vaida, V. Atmospheric processing of organic aerosols. *J. Geophys. Res.* **104**, 633 (1999).

33. Quinn, P. K. *et al.* Contribution of sea surface carbon pool to organic matter enrichment in sea spray aerosol. *Nat. Geosci.* **7**, 2228 (2014).

34. Latif, M, Brimblecombe, P. Surfactants in Atmospheric Aerosols. *Environ. Sci. Technol* **38**, 6501 (2004).

35. Vácha, R. *et al.* Effects of Alkali Cations and Halide Anions on the DOPC Lipid Membrane. *J. Phys. Chem. A* **113**, 7235 (2009).

36. Vácha, R. *et al.* Mechanism of Interaction of Monovalent Ions with Phosphatidylcholine Lipid Membranes. *J. Phys. Chem. B* **114**, 9504 (2010).

37. Clarke, R. J. & Lü, C. Influence of Anions and Cations on the Dipole Potential of Phosphatidylcholine Vesicles: A Basis for the Hofmeister Effect. *Biophys. J.* **76**, 2614 (1999).

38. Petrache, H. I., Zemb, T., Belloni, L. & Parsegian, V. A. Salt screening and specific ion adsorption determine neutral-lipid membrane interactions. *PNAS* **103**, 7982 (2006).

39. Krisch, M. J. *et al.* The Effect of an Organic Surfactant on the Liquid-Vapor Interface of an Electrolyte Solution. *J. Phys. Chem. C* **111**, 13497 (2007).

40. Raymond, E. A., Tarbuck, T. L., Brown, M. G. & Richmond, G. L. Hydrogen-Bonding Interactions at the Vapor/Water Interface Investigated by Vibrational Sum-Frequency Spectroscopy of HOD/H 2 O/D 2 O Mixtures and Molecular Dynamics Simulations. *J. Phys. Chem. B* **107**, 546 (2003).

41. Rizzuto, A. M., Irgen-Gioro, S., Eftekhari-Bafrooei, A. & Saykally, R. J. Broadband Deep UV Spectra of Interfacial Aqueous Iodide. *J. Phys. Chem. Lett* **7**, 3885 (2016).

42. Petersen, P. B. & Saykally, R. J. Confirmation of enhanced anion concentration at the liquid water surface. *Chem. Phys. Lett.* **397**, 51 (2004).

43. Petersen, P. B., Saykally, R. J., Mucha, M. & Jungwirth, P. Enhanced Concentration of Polarizable Anions at the Liquid Water Surface: SHG Spectroscopy and MD Simulations of Sodium Thiocyanide. *J. Phys. Chem. B* **109**, 10915 (2005).

44. Chamberlain, J. R. & Pemberton, J. E. Raman Spectroscopy of Langmuir Monolayers at the Air-Water Interface. *Langmuir* **13**, 3074 (1997).

45. Chattopadhyay, A. & London, E. Fluorimetric determination of critical micelle concentration avoiding interference from detergent charge. *Anal. Biochem.* **139**, 408 (1984).

46. Robin, I. *et al.* Holes in a stearic acid monolayer observed by dark-field electron microscopy. *Nature* **327**, 319 (1987).

47. Miranda, P. B. & Shen, Y. R. Liquid Interfaces : A Study by Sum-Frequency Vibrational Spectroscopy. *3292 J. Phys. Chem. B* **103**, 3292 (1999).

48. Schnitzer, C., Baldelli, S. & Shultz, M. J. Sum Frequency Generation of Water on NaCl, NaNO 3 , KHSO 4 , HCl, HNO 3 , and H 2 SO 4 Aqueous Solutions. *J. Phys. Chem. B* **104**, 585 (2000).

49. Enami, S., Fujii, T., Sakamoto, Y., Hama, T. & Kajii, Y. Carboxylate Ion Availability at the Air−Water Interface. *J. Phys. Chem. A* **120**, 22 (2016).

50. Zimmermann, R., Freudenberg, U., Schweiß, R., Küttner, D. & Werner, C. Hydroxide and hydronium ion adsorption — A survey. *Curr. Opin. Colloid Interface Sci.* **15**, 196 (2010).

51. Tse, Y.-L. S., Chen, C., Lindberg, G. E., Kumar, R. & Voth, G. A. Propensity of Hydrated Excess Protons and Hydroxide Anions for the Air−Water Interface. *J. Am. Chem. Soc* **22**, 5 (2015).

52. Petersen, P. B. & Saykally, R. J. Is the liquid water surface basic or acidic ? Macroscopic vs . molecular-scale investigations. *chem. Phys. Lett.* **458**, 255 (2008).

53. Tsay, R.-Y., Wu, T.-F. & Lin, S.-Y. Observation of G-LE and LE-LC Phase Transitions of Adsorbed 1-Dodecanol Monolayer from Dynamic Surface-Tension Profiles. *J. Phys. Chem. B* **108**, 18623 (2004).

54. Gamboa, I. C., Rios, H., Barraza, R. & Sanhueza, P. Behavior of Low-Solubility Detergents. *J. Colloid Interface Sci.* **152**, 230 (1992).

Chapter 6

Ion Adsorption from Mixed Salt Solutions

6.1 Introduction

Given the prevalence of water on the surface of the planet, it has been long understood that the air/water interface must play an important role in shaping atmospheric and aerosol chemistry[1,2]. Terrestrial oceans are one of the largest sources of aerosols on the planet, accounting for nearly $1.5x10^4$ Tg yr^{-1} of emitted sea salt aerosols[3]. These emitted aerosol particles have major importance in regulating atmospheric chemistry, acting as cloud condensation nuclei and catalyzing atmospheric chemistry through reaction occurring at their interface. Only in the past two decades has it been recognized that these particles influence atmospheric chemistry in another manner, viz. by providing a substrate for heterogenous chemistry between the gas phase molecules and ions adsorbed at the particle air/water interface. For a long time it was assumed that all ions were depleted at the air/water interface[4,5], pushed away by image charge repulsion[6]. However, it has become widely accepted over the past two decade that certain ions, namely large and highly polarizable anions like iodide or bromide, exhibit a positive surface excess, in opposition to previous understanding[7,8]. This finding has inspired a great number of experiments trying to better characterize and understand the physics that drive these anions to the interface. However, it remains uncertain how applicable these results are in understanding chemistry at the interface of atmospheric aerosols. While the composition of sea salt aerosols is a complex mixture of salts, proteins and organics, laboratory experiments have long focused on simpler single salt systems. Whereas these experiments have served to advance understanding of the fundamental physics of ion adsorption at the air/water interface, there remains a critical lack of knowledge regarding how interactions among constituents in solution and competition for surface adsorption sites might influence the interfacial behavior of ions. This question must be addressed if we are to attain a more complete understanding of the physics of ions at complex interfaces- like those of sea salt aerosols.

6.2 Motivations for Studying Mixed Salt Systems

Numerous field studies have observed that the depletion of ozone measured at Arctic sunrise is strongly correlated with a rise in bromine-containing compounds, particularly Br_2, which are thought to be initially generated from reactions of interfacially solvated bromide anions. That bromide specifically has been found to be the most important ion for the observed loss of artic ozone is unexpected, given the relatively low abundance of the anion in ocean waters. Bromide has an average concentration in the oceans of only .065 g/Kg water[9]. In contrast, the chloride ion has an oceanic concentration of ~19 g/kg, orders of magnitude larger than that of bromide, and is also known to exhibit modest surface activity. However, detection of Cl_2 in artic ozone depletion events is typically very low[10,11], implying that bromide dominates at the aerosol interface-even in the presence of significantly higher chloride concentrations. At present

however, details of the physics regarding this selective adsorption of Br^- anions remains largely uncharacterized. While the thermodynamics of simple solutions containing only a single salt have received a great deal of experimental attention[12–15], there has been little interest in studying the behavior of ions in mixed salt solutions, where the ions must compete for a limited number of surface sites. The surface affinity of ions at the interface can be heavily influenced by the presence of other species in solution, including organics and surfactants[14,16]. The role that other ions in solution may play in shaping ion surface populations, and even ion adsorption thermodynamics, is presently unclear. Results from previous studies of interfacial ion dynamics imply that these ion-ion interactions may be, in some cases, of significant importance in controlling ion surface activity. Studies of sodium nitrite[17] and magnesium acetate[18] at the interface have indicated that ion pairing may play an important role in these two systems. As such, in order to formulate a better fundamental description of the thermodynamics of ion near the solution/air interface, it is critical to investigate how the physics in simple mixtures may differ from those of single salt solutions. If the presence of other salts in solution does have a modulating effect on the surface activity of surface-active ions, it has important implications for atmospheric chemistry, catalysis and biology. From the standpoint of understanding the fundamental physics of ion adsorption at the air/water interface, this question is also of interest. Our understanding of the physics that cause selected ions to adsorb preferentially to the interface is still evolving, with several competing explanations found in the literature. Polarizability[19], size[5,19], and capillary waves[15] have all been identified by different authors as playing important roles in determining whether or not an ion exhibits a positive surface excess. Under some proposed mechanisms for ion adsorption at the air/water interface, it has been argued that it is solely the ion/water energetics that drive surface segregation[20], whereas other studies have found that water/water interactions are the most critical[15,21]. Investigation of mixed salt systems can help to validate models for ion surface affinity and better illustrate the mechanisms whereby some specific ions are preferentially adsorbed at the interface.

6.3 Past Experiments on Mixed Salt Systems

Few experiments have attempted to experimentally characterize the parallel interactions of salt mixtures on the adsorption of ions at the air/water interface. The lack of focus on these salt mixtures and their influence on ion surface activity is unsurprising, given that understanding of the thermodynamics of ion interfacial migration in even simple single salt systems is still in its infancy. Even so, as we will discuss in this section, a few studies carried out using ambient pressure x-ray photoelectron spectroscopy have provided some insights into the physics of mixed salt solutions.

6.3.1 XPS studies and simulations of mixed salt solutions

Experiments by Ottoson et al in 2010 used ambient pressure x-ray photoelectron spectroscopy (XPS) to study interfacial adsorption from solutions of NaBr and NaI[22] salt mixtures. In the resultant XPS spectra, both bromide and iodide anions were observed to be present at the interface, with iodide having a much higher surface affinity, in agreement with the predictions from the Hoffmeister series and previous simulations[8,23]. The authors then measured the

photoelectron spectra for mixed Br^-/Cl^- solutions, at a constant $Br^-:Cl^-$ ratio of 7:100, to determine if the interfacial behavior for the bromide changed in the presence of excess chloride. In these mixed salt experiments, the Br^-/Na^+ photoelectron intensity ratio was measured as a function of the total solution concentration. For a pure NaBr solution, the ratio was largely independent of the solution concentration, remaining slightly over 1 at all measured data points. However, in the mixed NaCl/NaBr salt solutions, the Br^-/Na^+ ratio was observed to increase as the total solution concentration rose. The observed increase in the ratio was then taken as evidence for the bromide being preferentially adsorbed at the interface, gradually displacing interface-bound chloride ions. The authors argued that because the bromide anions were replacing identically charged chloride at the surface, the electric field generated by the anions at the interface remained unchanged as the solution concentration rose. As a result of this static field, the sodium counterions remained at a constant distance from the interface, and thus yielded a constant photoelectron intensity as the surface bromide concentration increased. Supporting molecular dynamics simulation carried out by the authors agreed with this assessment, finding that as the bromide concentration in solution increased, the bromide anions gradually displaced chloride from the interface. The authors attributed this gradual replacement of the chloride by bromide ions to a salting out effect wherein, due to the high concentration used in the experiments (up to 6M), the halide anions competed for solvating waters in the solution bulk. This competition led to the more weakly solvated bromide being excluded to the interface so that the water molecules could preferentially solvate the bulk chloride anions. However, there was no experimental validation for this proposed mechanism of preferential bromide adsorption. Lack of suitable photoelectron transitions for the chloride ion meant that the chloride concentration could not be measured at the interface, and it could not be experimentally confirmed that the increase in bromide signal was correlated with a loss of chloride signal. The experiment also measured only a few concentration points in the mixed salt system, which precluded a complete description of the chloride/bromide interaction in the interfacial region.

A second XPS study carried out by Ghosal et al. also studied the mixed Br^-/Cl^- system, this time looking at solutions formed via deliquescence on mixed bromide/chloride salt crystals[12]. In the experiments, two different bromide doping ratios were tested, 7% and .1%, with the second being close to the natural bromide abundance in seawater, as discussed earlier. The results of the experiment were ultimately found to be independent of the bromide doping ratio in the salt crystal. For relative humidity below the deliquescence point, the Br^-/Cl^- ratio measured in the XPS spectra showed good agreement with the ratio for the bulk crystal. However, when the chamber humidity exceeded the deliquescence point and saturated salt solutions were formed on the surface of the salt disks, it was observed that the Br^-/Cl^- signal ratio increased by over an order of magnitude. This was taken as an indication that bromide was approaching the surface more closely than was the chloride. The authors attributed this change to preferential surface adsorption of the bromide in the mixed salt system. Further support for this conclusion was obtained from depth-resolved XPS studies of the mixed salt solutions. Those experiments showed that the greatest bromide enrichment was observed at the lowest measured photoelectron kinetic energy, corresponding to the highest surface sensitivity for the XPS experiment. As the energy of the photoelectrons was increased and the experiment probed deeper into the solution, the Br^-/Cl^- ratio was observed to decay back to its bulk value. The results of this experiment

provided compelling evidence for the preferential adsorption of bromide at the air/water interface even in the presence of excess chloride anions. However, due to the use of deliquescence for the formation of the salt solutions, the study could not control the solution concentration or determine how total solution salt concentration might impact the interaction of the two halides in solution.

The qualitative picture emerging from these paired XPS experiments is one of bromide being favored at the interface over chloride. This conclusion agrees well with molecular dynamics simulations for pure salt solutions, where it is found that larger halides are more surface active than their smaller counterparts[8,24]. However, these XPS studies were unable to measure the thermodynamics for ion adsorption in the mixed salt systems and therefore were unable to address the mechanism for the selective adsorption of bromide over chloride. The results of the two XPS studies are also hindered by the relatively poor interfacial resolution of photoelectron spectroscopy, which has a probe depth on the order of a few nanometers[25]. This makes the interpretation more difficult, as some of the measured signal in the photoelectron spectra must result from the sub-surface depletion layer. To gain a more accurate picture of the population at the outermost water layer and assess the mechanism of preferential anion adsorption, additional measurements are needed. Here we study the thermodynamics of surface adsorption in a mixed NaSCN/NaCl system via resonant deep-UV second harmonic generation(DUV-SHG) spectroscopy experiments. Exploiting the resonant enhancement property of the second-order nonlinear process allows for direct probing of the thiocyanate concentration at the solution surface in the presence of chloride. Modelling of the resultant adsorption isotherm subsequently permits the free energy of adsorption for thiocyanate in the mixed salt systems to be determined.

6.4 Thiocyanate Surface Adsorption in the Presence of NaCl

To attain a better understanding of the thermodynamics of ion adsorption in simple mixtures, we carried out a series of resonant DUV-SHG experiments on mixed solutions of sodium thiocyanate and sodium chloride at two different sodium chloride concentrations, .5 and 1 M. Second harmonic generation (SHG) is a second order non-linear optical process and all second harmonic photons measured are generated only from the air/water interface, giving the technique unmatched surface specificity. Sodium chloride was chosen as the second salt due to its large abundance in ocean water and due to its presence in sea salt aerosols, which are of current importance in atmospheric chemistry. We exploit the intense CTTS transition of the thiocyanate anion to directly probe the population of this ion at the air/water interface. By fitting the isotherm with a Langmuir model, the free energy of adsorption for the anion in the presence of the chloride background can be determined. The measured energetics for the adsorption of the thiocyanate at the interface provide important clues as to the mechanism of adsorption for the anion in the mixed salt system.

6.4.1 Experimental design

The experimental set-up used in these experiments was identical to that employed to study ion adsorption to surfactant interfaces discussed in the previous chapter. Briefly, the

output from an 800 nm 100 fs Ti:Sapphire oscillator was used to seed a chirped pulse amplifier, which ultimately output 100 fs 800 nm laser pulses a 1kHz repetition rate. The 800 nm pulses were passed into an optical parametric amplifier, which allowed for the wavelength of the femtosecond pulses to be tuned. In all experiments described here the probe wavelength was 386 nm, chosen so the second harmonic at 193 nm was resonant with the charge transfer to solvent band of the sodium thiocyanate. The chloride anion also exhibits a CTTS transition but very deep in the UV near 170 nm[26], inaccessible for the present experiments. Because the chloride CTTS is significantly off-resonance with the second harmonic of the input, which is centered at 193 nm, the 386 nm probe employed in the experiment was not sensitive to the near-surface chloride population.

After exiting the OPA, the wavelength-shifted pulse was passed through a motorized rotating neutral density filter, which allowed for continuous modulation of the laser input power. The laser power after the neutral density was measured for each shot using a 1% beam pickoff and photodiode, while the laser pulse was focused onto the sample with a 100 mm focal length MgF_2 lens.

The samples in the experiment were Pyrex petri dishes containing ~18 ml of the solution. All glassware used in the experiment was carefully cleaned using NOCHROMIX/sulfuric acid solution. The thiocyanate used in the experiment was supplied by J.T. Baker and was of reagent grade to ensure the highest purity. The NaCl was provided by Alfa Aesar and was also of 99% reagent grade quality. All solutions were made with 18 MΩ resistivity water having total organic carbon content of 3 ppb or less from a Millipore Milli-Q system. Before each experiment, the salts were baked in an oven overnight at 200^{o}C to drive off any adsorbed organics.

After reflection from the sample surface, the second harmonic light was separated from the colinear fundamental via transmission through a Pellin-Broca prism. The SHG was then focused into a monochromator and PMT, where the signal was recorded. Custom-written Python software was used to analyze the signal intensity as a function of NaSCN concentration. Using a Langmuir isotherm model, the free energy of adsorption for the SCN^- was extracted for the mixed salt system and compared to that of a pure sodium thiocyanate solution.

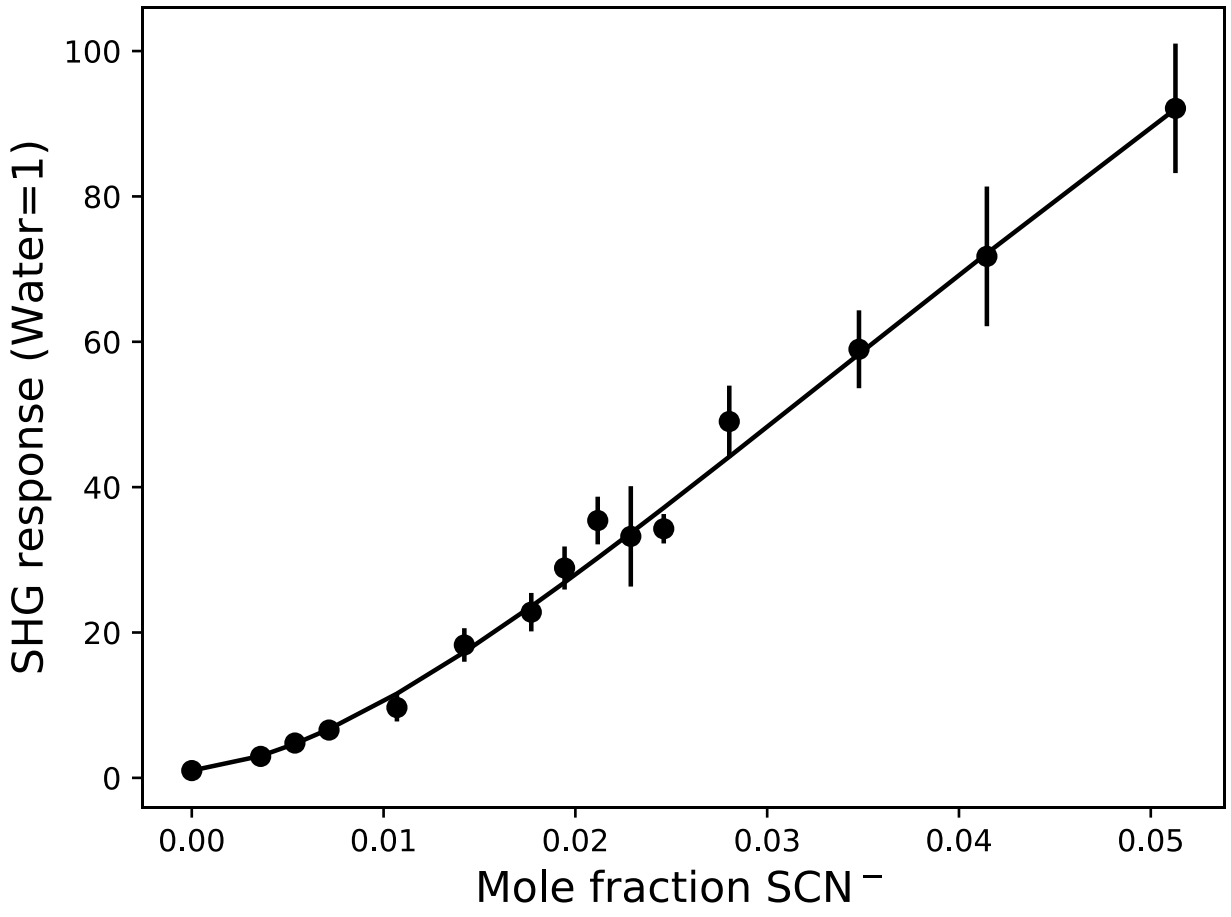

Figure 6.1: Measured adsorption isotherm for the thiocyanate anion in the presence of 1 M NaCl. The solid line is the best fit to a Langmuir isotherm model., which yields a Gibbs free energy of adsorption of -6.6 ±.6 kJ/mol. This value is lower than that measured for a pure thiocyanate solution of -7.53±.13 kJ/mol, showing that there is a small change in the adsorption thermodynamics as a result of the addition of chloride to the solution.

6.4.2 Results and discussion

Figure 6.1 shows the measured adsorption isotherm for sodium thiocyanate in the presence of a constant 1 M NaCl background. In the plot, the measured signal intensity at each concentration is normalized to the signal from a pure 1M NaCl solution. The fit of the experimental data to the Langmuir isotherm model yields a free energy of adsorption for the thiocyanate in the mixed salt solution of -6.6 ±.6 kJ/mol. Table 1 shows show the free energies of adsorption for thiocyanate in the presence of NaCl, compared to the previously measured literature value for a pure SCN solution. As evident in the table, the free energy obtained for adsorption in the mixed salt system is measured to be lower than the value of -7.53±.13 kJ/mol measured in the absence of a competing salt[27]. To confirm that this observed difference in the free energy of adsorption was real, we made an identical measurement of the adsorption free energy for pure thiocyanate at the air/water interface. The resulting isotherm and fitted free energy are displayed in Figure 6.2 and Table 1, respectively. Our fit produced a value for the pure sodium thiocyanate solution of -8.6±1.3 kJ/mol. This measured value for the energy of adsorption value is higher than, but within error of, the literature value for thiocyanate. The large uncertainty in the adsorption energy is a result of the large errors in the signal intensity values for the pure SCN solutions at some of the measured concentrations.

System	ΔG_{ads} for thiocyanate
NaSCN with 1M NaCl (this study)	-6.6 ±.6 kJ/mol
Pure NaSCN(this study)	-8.6±1.3 kJ/mol
Pure NaSCN (Ref. 27)	-7.53±.13 kJ/mol

Table 6.1: Values of ΔG_{ads} obtained from the Langmuir isotherm fit for thiocyanate in the presence and absence of NaCl

Why SHG intensity from these solutions displayed such large errors relative to the mixed salt solutions is currently uncertain and in the future some of these data will be retaken to improve the fit statistics. Regardless of the large error bars, it is clear, from both the literature value and our own measurements, that the measured free energy of adsorption from solutions containing 1M NaCl is lower than that of the pure thiocyanate. These results imply that the presence of the NaCl in solution slightly lowers the thermodynamic surface affinity of the thiocyanate anion. Another difference between the isotherms with and without the NaCl are the SHG intensities at each concentration. The normalized signal values for the mixed salt solution and pure thiocyanate solution are similar for thiocyanate concentrations below 1 M, but at higher thiocyanate concentrations, second harmonic intensity is higher for the mixed salt solution than from the pure thiocyanate, as evident in Figure 6.3. As the signal intensity is related to the surface population of the resonant ion, the observed increase in SHG signal implies that in the mixed salt solution there is more thiocyanate at the interface than is present in the pure solution.

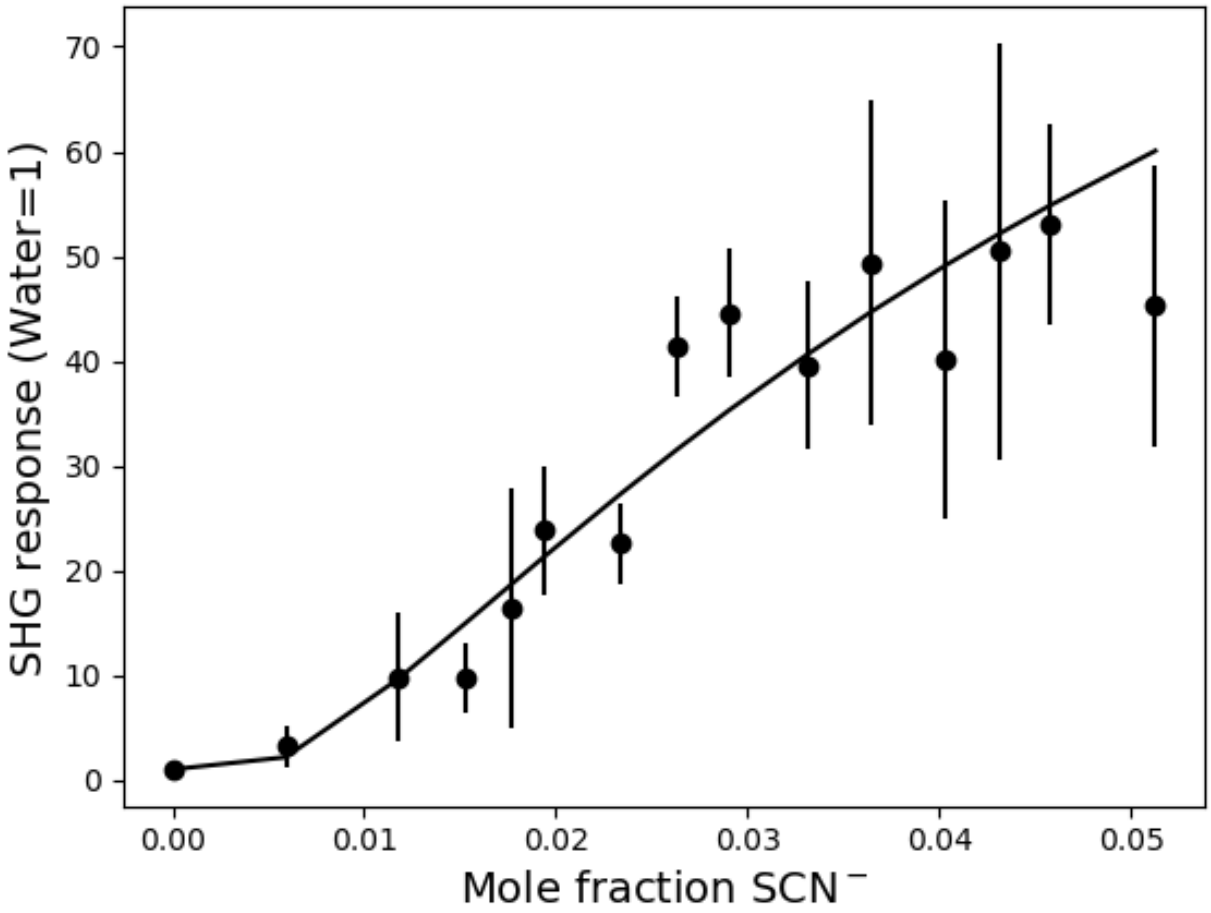

Figure 6.2: Adsorption isotherm for thiocyanate anion in solutions of pure NaSCN. The solid line is the best fit to a Langmuir isotherm model, which yields a free energy of adsorption for the thiocyanate of -8.6 ±1.3 kJ/mol. The large uncertainty in some of the measured data points resulted in the correspondingly large error in the fitted free energy.

To assess the effects of changing the NaCl concentration on the measured SCN surface affinity, a second set of experiments was conducted wherein the NaCl concentration was reduced to .5 M, half the previous value. The resulting adsorption isotherm, shown in Figure 6.4, was again fit to the Langmuir isotherm model to yield a free energy for the SCN adsorptions. The fitted free energy of adsorption of -6.4±.6 kJ/mol in the .5 M NaCl experiments was nearly identical to that measured for 1M NaCl, as can be seen in Table 6.2. Once again, the measured free energy in the mixed salt solution is lower than that measured for pure thiocyanate solution. As with the 1M NaCl experiments, there may also be an increase in the normalized second harmonic intensity for the .5M NaCl solution, although the difference is less certain in the .5 M case, as the relative errors are larger than in the 1M experiments. In conclusion, the behavior of thiocyanate is observed to be identical for the 1M vs. .5m NaCl background salt concentrations, with no difference in the signal intensity or fit free energy of adsorption. However, there are observed differences between the behavior of the thiocyanate anions in the solutions with and without the NaCl, namely that the free energies of adsorption are lower in the presence of chloride and the measured SHG intensities are higher. We will discuss possible origins for both of these differences in the following sections.

NaCl concentration	Fit free energy
0 (pure thiocyanate solution)	-8.83±1.3 kJ/mol
.5 M	-6.4±.6 kJ/mol
1 M	-6.6±.6 kJ/mol

Table 6.2: Values of ΔG_{ads} obtained from the Langmuir fitting isotherm for thiocyanate in the presence of different concentrations of NaCl.

First, we address the change in the free energy of adsorption observed for thiocyanate in the mixed salt solution. In accordance with previous studies of mixed salt solutions, the most likely origin for the minor decrease in the adsorption free energy observed in the experiment is competitive adsorption between the Cl^- and SCN^- anions at the air/water interface. As Cl^- ions are predicted to be near-neutral with regard to their surface affinity[28], for a pure solution of 1M NaCl the native state is one in which some of the chloride anions will be adsorbed to the solution interface, likely at sub-monolayer coverage. As NaSCN concentration increases in the solution, it will also begin to adsorb to the interface. Since the free energy of adsorption for the SCN^- is more favorable than that of Cl^-, there exists a driving force for the gradual replacement of chloride by thiocyanate at the interface as the surface sites approach saturation. The replacement of the interfacially bound chloride ions by thiocyanate anions from the solution bulk can be written as follows:

$$SCN^-_{bulk} + Cl^-_{surf} \rightarrow SCN^-_{surf} + Cl^-_{bulk} \qquad (6.1)$$

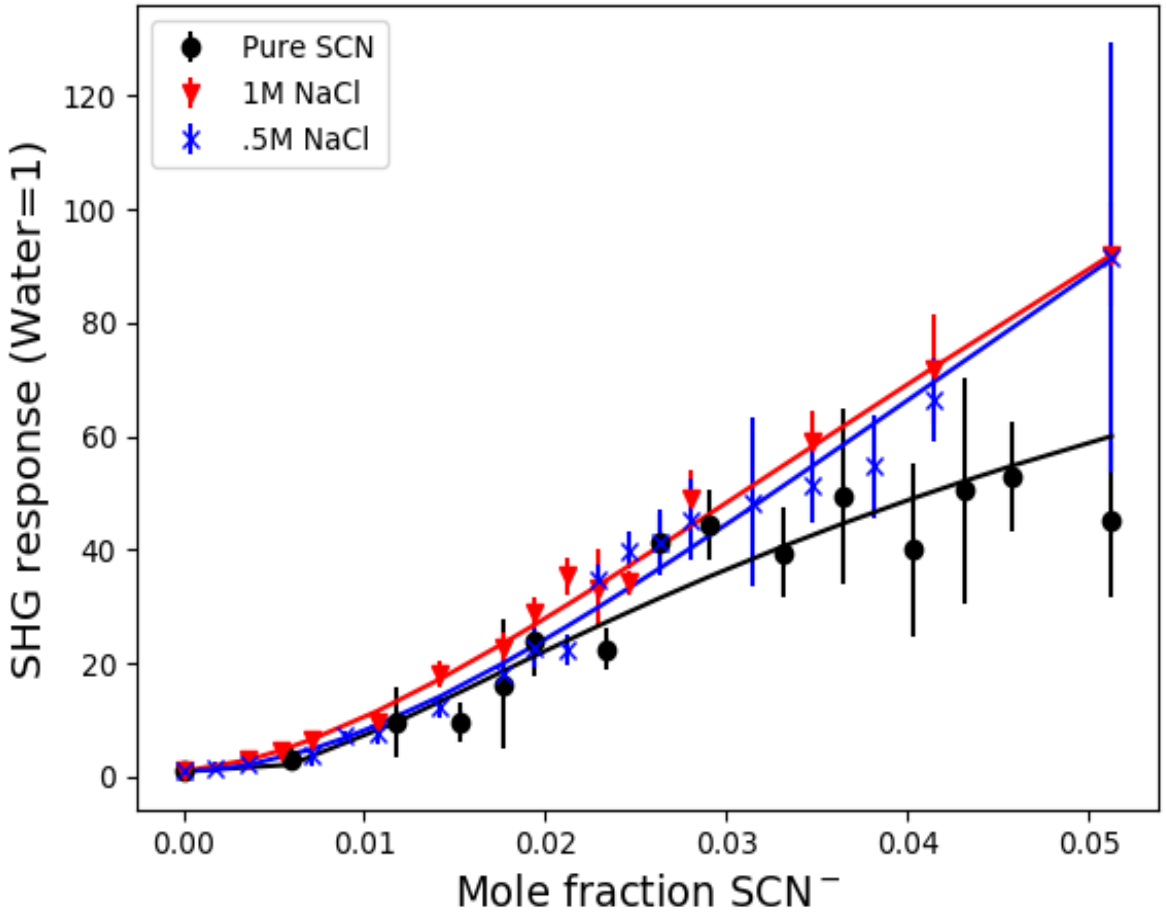

Figure 6.3: Adsorption isotherms and best fit lines for the thiocyanate anion in 0, .5M and 1 M NaCl solutions. The addition of NaCl results in a lowering of the free energy of adsorption for thiocyanate relative to its value in pure NaSCN solutions. The normalized SHG intensity is also found to increase with the addition of the NaCl.

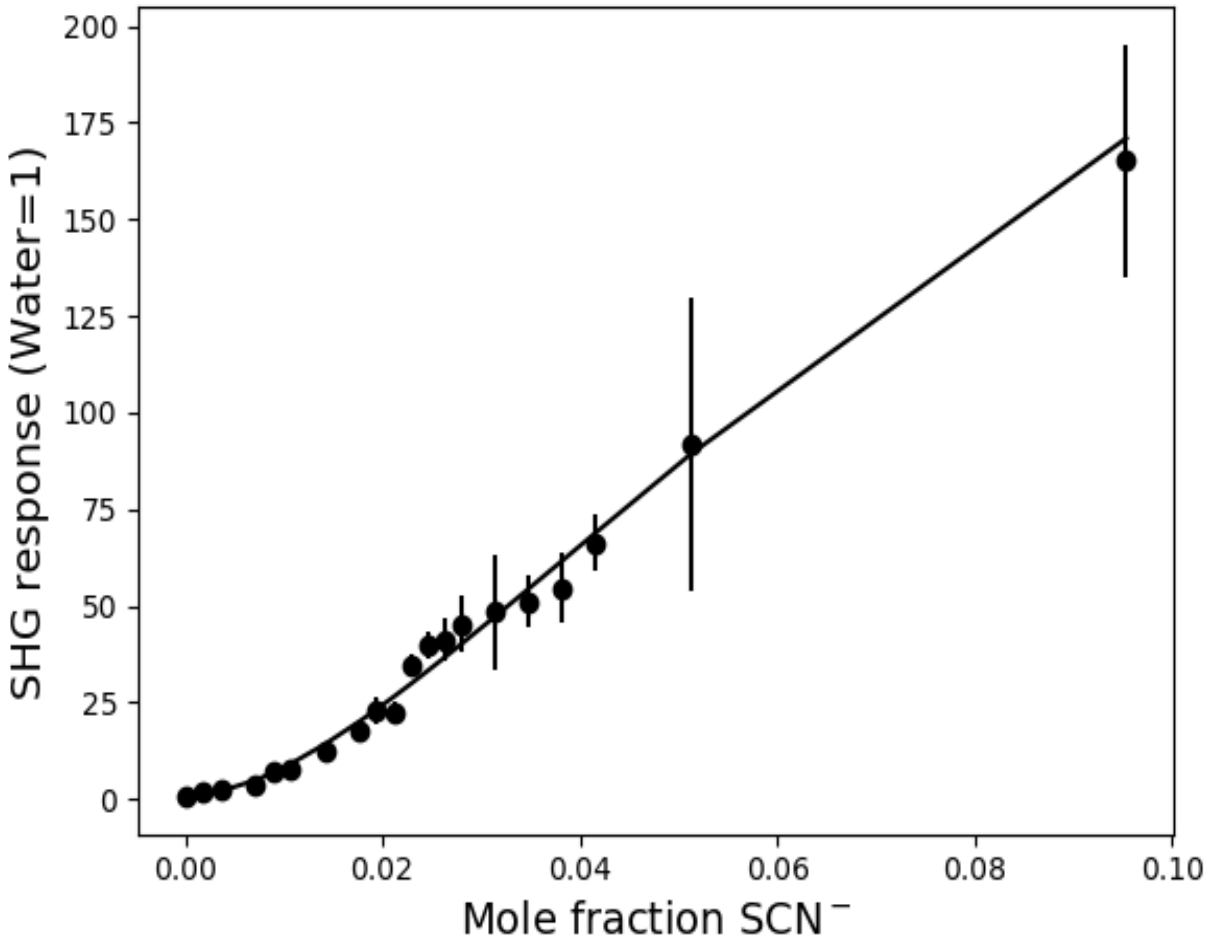

Figure 6.4: Adsorption isotherm for thiocyanate anion in mixed solution with 0.5 M NaCl. The fit to the Langmuir isotherm model yields a free energy of adsorption for the thiocyanate of -6.4 ±.6 kJ/mol. This value is nearly identical to that for the 1M NaCl solutions and is lower than that measured for pure NaSCN

The expected change in the free energy for this interfacial replacement process can expressed as:

$$\Delta G_{ads,mixed} = \Delta G_{ads,SCN} - \Delta G_{ads,Cl} \qquad (6.2)$$

Here $\Delta G_{ads,mixed}$ is the experimentally measured free energy of adsorption in the mixed salt solution and $\Delta G_{ads,i}$ are the free energies of adsorption for the individual ions from pure solutions. From Equation 6.2 and our measurement of the free energy of adsorption for a pure thiocyanate solution, a small favorable free energy of adsorption of between 0.4 and 3 kJ/mol can be predicted for the chloride ion at the air/water interface. Previous calculations of the free energy of adsorption for chloride at the air/water interface have predicted it to be near-neutral with regard to adsorption at the air/water interface[28]. Therefore, our measurements are in line with theoretical predictions, at least at the lower bound. We can confirm that this proposed replacement mechanism is real by carrying out future experiments wherein we directly probe the chloride ion at the interface. By tuning the input wavelength for the SHG measurement to ~340 nm so that the second harmonic lies on the chloride CTTS transition near 170 nm[26] we could directly observe the replacement of chloride at the interface. As an additional benefit, such experiments would also allow for the direct measurement of the adsorption free energy for the chloride anion at the air/water interface. However, this would require a more sophisticated detection system than employed in the present studies.

It is also important to consider the thermodynamic forces that drive the SCN^- to displace the chloride anions at the interface. As discussed earlier, XPS experiments carried out by Ottoson et al. on mixed salt systems ascribed the replacement of chloride by bromide to a salting-out effect due to differences in the solvation energies of the two anions. In that proposed mechanism, it was argued that, due to competition for solvating waters, the less favorably hydrated ion is driven to the interface so its solvating waters can be liberated to hydrate is competitor. We observe no evidence for the existence of this salting-out effect in the SHG measurements here, at least at the concentrations range studied. Normally, when an ion moves to the interface, its solvating water molecules are returned to the solution bulk, where they can participate in energetically favorable hydrogen bond formation with other water molecules.[29] If the demixing mechanism described by Ottoson were active in driving thiocyanate to replace chloride at the interface, the released water would instead transfer to solvate a chloride ion. The energy resulting from the transfer of this water molecule between anions should manifest itself as an increased favorability in the driving force for surface segregation of the thiocyanate. Assuming the transfer of a single water from thiocyanate to a chloride, the free energy of adsorption should show an additional driving force of:

$$\Delta H_{exp} = E_{H2O,Cl} - E_{H20,SCN} - E_{H-bond} \quad (6.3)$$

Here ΔH_{exp} is the change in the enthalpy of adsorption in the mixed salt system assuming that the transfer of a water, $E_{H20,i}$ is the water-ion interaction energy for each respective ion and $E_{H\text{-}bond}$ is the energy of a hydrogen bond in the water bulk. The water hydrogen bond energy in Equation 6.3 can be taken to be ~25 kJ/mol, a typical energy for a hydrogen bond in water. For the spherical chloride anion, we can predict the water-ion interaction energy by dividing the chloride solvation enthalpy by its coordination number of 6 water molecules to obtain a value of -60 kJ/mol[30]. As thiocyanate is a polyatomic anion, the same simple approach is not appropriate. However, simulations have predicted the bond energy for hydrogen bonding to the S terminus of thiocyanate to be ~-20 kJ/mol and to the N terminus to be ~-54 kJ/mol[31]. Thus, from Equation 6.3, the transfer of a water molecule from thiocyanate to chloride should change the enthalpy component of the measured free energy of adsorption at the interface by ~-15 kJ/mol, assuming that water loss is at the sulfur rather than nitrogen terminus of SCN. Our measured free energy difference does not show such a significant change in the energetics of adsorption. In fact, in the presence of the chloride, we observe a minor *decrease* in the favorability of thiocyanate adsorption energies. As such, the preferential adsorption for the thiocyanate cannot be explained via a simple difference in solvation energies. To explain the difference in the surface propensity of the two ions, a more complex model must be invoked, one that takes into account not just the ion/water interaction but also polarizability, ion size and entropic effects as well.

The difference in the normalized SHG intensities for the pure vs. NaCl systems is more difficult to explain. As the observed free energy is lowered in the presence of NaCl, it does not result from an increase in the propensity of adsorption for the thiocyanate ion. Figure 6.5 shows the square root of the SHG signal intensity vs the bulk sodium thiocyanate concentration for the pure thiocyanate solution vs. the 1 M NaCl/NaSCN solutions. As this value is directly proportional to the number of surface-bound thiocyanate anions, this plot better displays the difference in the relative surface thiocyanate population in the two traces. As can be seen, at a thiocyanate concentration of 3M, there are about 30-50% more thiocyanate anions interacting with the probe beam in the mixed salt experiments relative to the pure thiocyanate solution. To explain this difference, it must be determined how these additional anions are being accommodated at the surface, if indeed they are bound at the interface.

A likely explanation for the observed change in the detectable thiocyanate population upon the addition of NaCl is electrostatic effects from changes in the screening length of the solution. In simulations of anion adsorption at the air/water interface, the adsorption of ions at the surface eventually displays a saturation effect, wherein additional ions are no longer able to be accommodated at the surface. A key contributor to the saturation of the solution surface is charge-charge repulsion from the like-charged anions bound at the air/water interface[8,32]. In the mixed salt experiments, at all measured thiocyanate concentrations there exist additional ions in solution, relative to the pure SCN experiments, due to the presence of the NaCl. This increase in the ionic strength as a result of the presence of the second salt should alter the charge screening

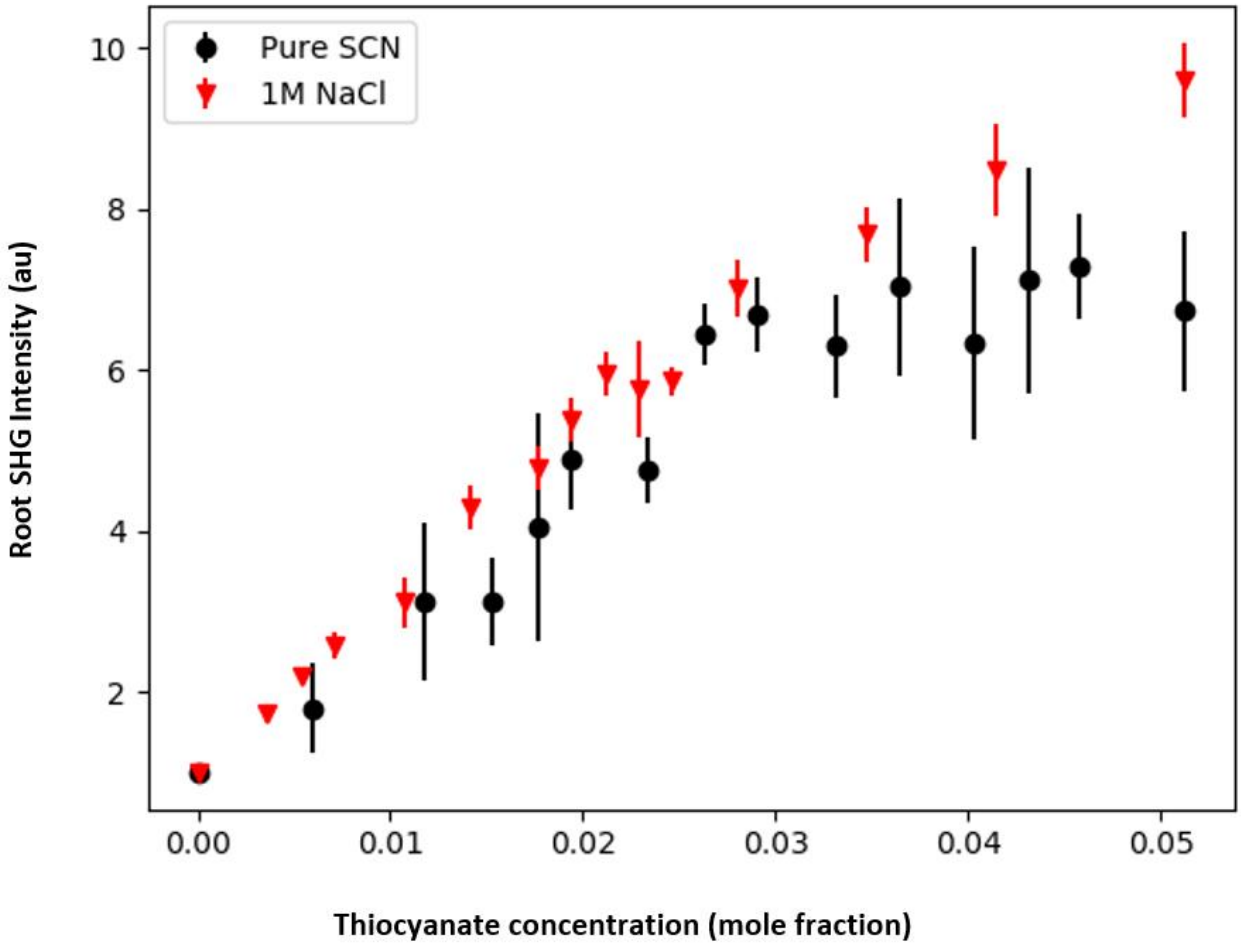

Figure 6.5: Square root of the second harmonic signal intensity for the pure thiocyanate solutions and 1M NaCl/NaSCN mixed salt solutions. As the second harmonic intensity is related to the square of the interfacial population, the figure depicts how the interfacial population of SCN changes with total bulk concentration in each system.

in the solution, which will ultimately affect the effective interfacial 'size' of a given thiocyanate anion at the interface by influencing the distance over which the ion negative charge is screened. From the Debye-Huckel theory of charge screening, the electric field in solution decays exponentially with the decay constant κ given by the expression:

$$\kappa^{-1} = \sqrt{\frac{\varepsilon_0 \epsilon_r kT}{\sum_i c_i z_i e^2}} \quad (6.4)$$

Here ε_0 and ε_r are the permittivity of free space and the dielectric constant for the medium, respectively, k is the Boltzmann constant and the denominator is a sum over all species in solution, with c_i and z_i being the concentration and charge of each species. As can be seen from Equation 6.4, the screening length decreases as the concentration of ions in solution increases. This implies that the electrostatic repulsion between thiocyanate ions at the interface should be decreased in the presence of the NaCl background and that, as a consequence, the interface should be able to accommodate additional thiocyanate anions. However, the simple picture of electrostatic screening given by Debye-Huckel theory is only valid in the dilute limit. At high solution concentrations, the assumption of uncorrelated ions breaks down and Equation 6.4 is no longer valid. For the experiment detailed herein, the total salt concentrations in the sample solutions ranged from 1M up to 4 M. It has been observed in experiments that at solution concentration greater than ~1M, the effective screening length can actually *increase* with increasing concentration[33,34]. In the mixed salt solution, this would result in an increase in the electrostatic repulsion between anions at the interface and a decrease the surface population at the outermost boundary of the solution. However, it is still possible that an increase in the screening length might account for the observed increase in second harmonic signal seen from the mixed salt solutions. In this case, the intensity increase would be a result of the double layer structure of ions adsorbed at the air/water interface. To compensate the charge of the thiocyanate anions bound at the water surface, the sodium counterions form a subsurface enhancement layer directly underneath the interface bound anions. The resultant double layer generates an electric field, which then propagates into the solution to depths on the order of the solution screening length, breaking the inversion symmetry in the region where the DC field exists. As a result of this broken inversion symmetry, some of the bulk solution becomes visible to the nonlinear probe laser. This double layer electric field effect is well-documented in experiments employing sum frequency generation, wherein signal from the water molecules is traditionally found to increase upon the addition of a surface-active salt due to the resultant electric field[35,36]. In the case of the resonant second harmonic generation experiments discussed here, if the presence of the sodium chloride in solution resulted in an increase of the solution screening length, the electric field will penetrate deeper into the solution and increase the amount of thiocyanate visible to the probe. For very highly concentrated solutions, the screening length can be as high as several nm, allowing for DC electric field propagation well into the bulk of the solution[34].

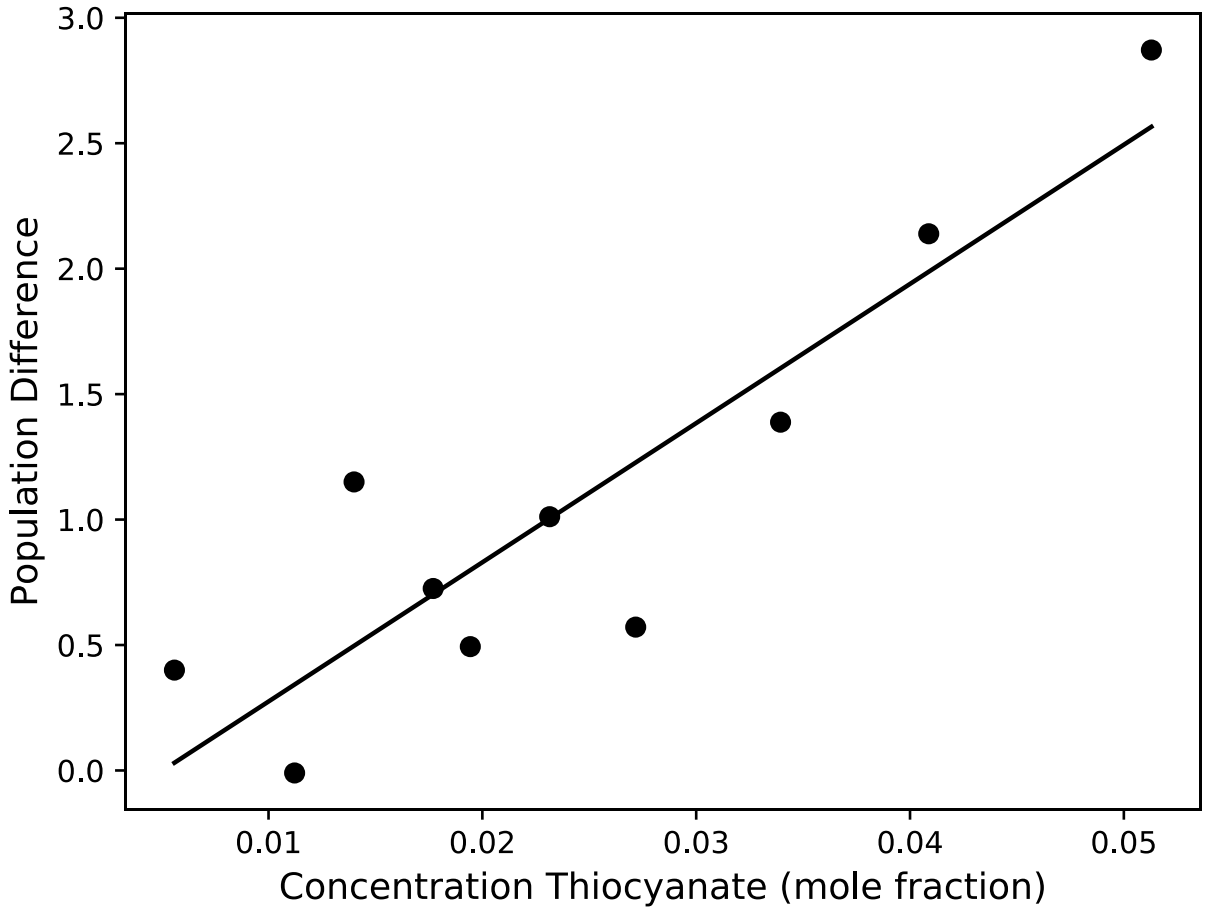

Figure 6.6: Population difference between pure SCN and 1M mixed salt solution as a function of solution thiocyanate concentration. The population difference grows roughly linearly with solution concentration.

Figure 6.6 shows the difference in detectable thiocyanate population for the 1M salt solution vs. the pure thiocyanate solution as a function of thiocyanate concentration. In the figure, the plotted line is simply a guide for the eye. As can be seen, the population scales linearly with the bulk thiocyanate concentration. This linearity in the scaling is good evidence for the difference in observed signal resulting from an increase in the effective screening length in the solution. According to a study by Lee et al[33] , the screening length in a concentrated solution should scale roughly linearly with the solution concentration. As the screening length increases, more of the bulk solution is detected by the probe beam, resulting in a linear scaling in the visible thiocyanate population.

It should be noted that, due to changes in the screening length, the population of thiocyanate bound at the outermost layers of the solution would be expected to decrease due to enhanced electrostatic repulsion at the interface. However, this would not be expected to be an important contributor to the change in total SHG signal observed in the experiment. This is because the bulk solution, which become increasingly visible to the probe as the screening length increases, contains significantly more anions than does the interfacial layer. Therefore, any signal loss due to changes in the thiocyanate surface population should be negligible compared to the signal increase stemming from an increase in visible bulk phase thiocyanate ions. Experimentally untangling the impact of these two effects, interfacial coulombic repulsion and the increase in the experimental probe depth, is difficult. One manner of addressing the problem would be to measure the adsorption isotherms as a function of ionic strength of the solution by varying the ratio of thiocyanate and a background salt, like NaCl. Differences in the shape of the measured isotherms may provide some insight into the structure of the ions near the interface. It should also be noted that this change in solution screening length may also affect the adsorption free energy for the thiocyanate via increases in the Coulombic repulsion between interfacially--bound ions. As it is unclear from the resonant SHG experiments at what bulk concentration the surface thiocyanate population saturates, it is difficult to predict how important such charge-charge repulsion is in determining the measured free energy values. We do note, however, that the fact that we obtain the same fitted free energy for both the 0.5 and 1 M NaCl solutions seems to imply that the competitive adsorption effect dominates over electrostatic effects in determining the free energy of adsorption. Proper decoupling of competitive ion adsorption effects and electrostatics might be achieved in future experiments through use of a background salt with known low surface propensity, such as fluoride, which will allow for isolation of the electrostatic effects. The importance of electrostatic effects could also be assessed by switching to a divalent ion, such as sulfate, as the electrostatic effect should scale as the square of the ionic charge.

The results presented here have significant implications for the use of resonant second harmonic generation as a tool for probing the populations of ions adsorbed at the interface. If increases in the probe depth are indeed playing an important role in the experiment, as is implied by the results of this study, then the technique is significantly more bulk-sensitive than has previously been assumed. To assess the importance of this bulk concentration effect, the SHG signal from a non-surface active resonant salt should be measured as a function of added NaCl. If the bulk contributions are important, the signal should show an increase as a function of added NaCl due to greater penetration depth into solution. The adsorption isotherms for pure thiocyanate solutions could also be measured in different concentration regimes (i.e. 0.1-1M, 1-

2M, etc.) to assess what impact total salt concentration has on the apparent free energy of adsorption.

Conclusions

The addition of a background salt to the solution of interfacially active ions has only a modest effect on the energetics of adsorption, the change likely due to a combination of increased electrostatic repulsion at the interface and energetic penalties resulting from desorption of chloride from interface sites. However, the mixture of electrostatic and ion-specific effects is difficult to untangle in the current experiment. Probably, both play a role in establishing the energetics of movement of thiocyanate anions from the solution bulk to the interface. More interesting from a practical viewpoint is the role the background salt plays in determining the number of ions at the interface, which has implications for atmospheric aerosol reaction kinetics. In the measured thiocyanate signal it is difficult to quantify this potential effect, as it is convoluted with changes in the experimental probe depth. Further experiments are needed to decouple the different effects. Theoretical modeling would also help to decouple the various contributions to the signals in the experiment.

References:

1. Goldacre, R. J. Surface Films on Natural Bodies of Water. *J. Anim. Ecol.* **18**, 36 (1949).
2. Chalmers, J. M., Pasquill, F. & Chalmers, J. A. The potential difference at an air-water interface. *London, Edinburgh, Dublin Philos. Mag. J. Sci.* **Series 7 V**, 88
3. Mcneill, V. F. Atmospheric Aerosols: Clouds, Chemistry, and Climate. *Annu. Rev. Chem. Biomol. Eng* **8**, 427 (2017).
4. Jones, G. & Ray, W. A. A Differential Method for Relative Surface Tension The Surface Tension of Solutions of Electrolytes as a Function of the Concentration. I. A Differential Method for Measuring Relative Surface Tension. *A Differ. Method Relat. Surf. Tens.* (1937).
5. Levin, Y., Santos, A. P., Diehl, A., Dos Santos, A. P. & Diehl, A. Ions at the Air-Water Interface : An End to a Hundred-Year-Old Mystery ? *Phys. Rev Lett.* **103**, 257802 (2009).
6. Onsager, L. & Samaras, N. N. T. The Surface Tension of Debye-Hückel Electrolytes The Surface Tension of Debye-Huckel Electrolytes. **2**, 528 (1934).
7. Petersen, P. B. & Saykally, R. J. On The Nature Of Ions At The Liquid Water Surface. *Annu. Rev. Phys. Chem.* **57**, 333 (2006).
8. Jungwirth, P. & Tobias, D. J. Specific Ion Effects at the Air/Water Interface. *Chem. Rev* **106**, 1259 (2006).
9. Garrison, T. S. *Oceanography: An Invitation to Marine Science*. (Brooks Cole).

10. Spicer, C. W. *et al.* Molecular halogens before and during ozone depletion events in the Arctic at polar sunrise: concentrations and sources. *Atmos. Environ.* **36**, 2721 (2002).

11. Krishna L. Foster, Robert A. Plastridge, J. W. B., Paul B. Shepson, B. J. F.-P. & Chester W. Spicer. The Role of Br2 and BrCl in Surface Ozone Destruction at Polar Sunrise. *Science* **288**, 301 (2000).

12. Ghosal, S. *et al.* Ion Partitioning at the Liquid/Vapor Interface of a Multicomponent Alkali Halide Solution: A Model for Aqueous Sea Salt Aerosols. *J. Phys. Chem. A* **112**, 12378 (2008).

13. Liu, D., Ma, G., Levering, L. M. & Allen, H. C. Vibrational Spectroscopy of Aqueous Sodium Halide Solutions and Air-Liquid Interfaces: Observation of Increased Interfacial Depth. *J. Phys. Chem. B* **108**, 2252 (2004).

14. Onorato, R. M., Otten, D. E. & Saykally, R. J. Adsorption of thiocyanate ions to the dodecanol/water interface characterized by UV second harmonic generation. *PNAS* **106**, 15176 (2009).

15. Otten, D. E., Shaffer, P. R., Geissler, P. L., Saykally, R. J. & Dale E. Otten, Patrick R. Shaffer, Phillip L. Geissler, and R. J. S. Elucidating the mechanism of selective ion adsorption to the liquid water surface. *PNAS* **109**, 21 (2012).

16. Krisch, M. J. *et al.* The Effect of an Organic Surfactant on the Liquid-Vapor Interface of an Electrolyte Solution. *J. Phys. Chem. C* **111**, 13497 (2007).

17. Otten, D. E., Onorato, R., Michaels, R., Goodknight, J. & Saykally, R. J. Strong surface adsorption of aqueous sodium nitrite as an ion pair. *Chem. Phys. Lett.* **519**–**520**, 45 (2012).

18. Minofar, B. *et al.* Propensity for the Air/Water Interface and Ion Pairing in Magnesium Acetate vs Magnesium Nitrate Solutions: Molecular Dynamics Simulations and Surface Tension Measurements. *J. Phys. Chem. B* **110**, 15939 (2006).

19. Levin, Y. Polarizable Ions at Interfaces. *Phys. Rev Lett.* **102**, 147803 (2009).

20. Yagasaki, T., Saito, S. & Ohmine, I. Effects of Nonadditive Interactions on Ion Solvation at the Water/Vapor Interface: A Molecular Dynamics Study. *J. Phys. Chem. A* **114**, 12573 (2010).

21. Caleman, C., Hub, J. S., Van Maaren, P. J., Van Der Spoel, D. & Levitt, M. Atomistic simulation of ion solvation in water explains surface preference of halides. *PNAS* **108**, (2011).

22. Ottosson, N. *et al.* The influence of concentration on the molecular surface structure of simple and mixed aqueous electrolytes. *Phys. Chem. Chem. Phys.* **12**, 10637 (2010).

23. Tobias, D. J., Stern, A. C., Baer, M. D., Levin, Y. & Mundy, C. J. Simulation and Theory of Ions at Atmospherically Relevant Aqueous Liquid-Air Interfaces. *Annu. Rev. Phys. Chem* **64**, 339 (2013).

24. Jungwirth, P. & Cremer, P. S. Beyond Hofmeister. *Nat. Publ. Gr.* **6**, 261–263 (2014).

25. Stoerzinger, K. A., Hong, W. T., Crumlin, E. J., Bluhm, H. & Shao-Horn, Y. Insights into Electrochemical Reactions from Ambient Pressure Photoelectron Spectroscopy. *Acc. Chem. Res* **48**, 27 (2015).

26. Fox, M. F., Barker, B. E. & Hayon, E. Far-Ultraviolet Solution Spectroscopy of Chloride Ion. *J. Chem. Soc. Faraday Trans. 1* **12**, 1776 (1977).

27. Petersen, P. B., Saykally, R. J., Mucha, M. & Jungwirth, P. Spectroscopy and MD Simulations of Sodium Thiocyanide. *J. Phys. Chem. B* **109**, 10915 (2005).

28. Baer, M. D., Kuo, I.-F. W., Bluhm, H. & Ghosal, S. Interfacial Behavior of Perchlorate versus Chloride Ions in Aqueous Solutions. *J. Phys. Chem. B 2009,* **113**, 15843 (2009).

29. Otten, D. E., Shaffer, P. R., Geissler, P. L. & Saykally, R. J. Elucidating the mechanism of selective ion adsorption to the liquid water surface. **109**, 21 (2012).

30. Powell, D. H., Barnes, A. C., Enderby, J. E., Neilson, G. W. & Salmon, P. S. The Hydration Structure around Chloride Ions in Aqueous Solution. *Faraday Discuss. Chem. SOC* **85**, 137 (1988).

31. Lommerse, J. P. M. & Cole, J. C. Hydrogen Bonding to Thiocyanate Anions: Statistical and Quantum-Chemical Analyses. *Acta Cryst* **54**, 316 (1998).

32. Petersen, P. B. & Saykally, R. J. Confirmation of enhanced anion concentration at the liquid water surface. *Chem. Phys. Lett.* **397**, 51 (2004).

33. Lee, A. A., Perez-Martinez, C. S., Smith, A. M., Perkin, S. & Paulson, J. A. Scaling Analysis of the Screening Length in Concentrated Electrolytes. *Phys. Rev. Lett* **119**, 26002 (2017).

34. Smith, A. M., Lee, A. A. & Perkin, S. The Electrostatic Screening Length in Concentrated Electrolytes Increases with Concentration. *Phys. Chem. Lett.* **7**, 2157 (2016).

35. Mucha, M. *et al.* Unified Molecular Picture of the Surfaces of Aqueous Acid, Base, and Salt Solutions. *J. Phys. Chem. B* **109**, 7617 (2005).

36. Shultz, M. J., Baldelli, S., Schnitzer, C. & Simonelli, D. Aqueous Solution/Air Interfaces Probed with Sum Frequency Generation Spectroscopy. *J. Phys. Chem. B* **106**, 5313 (2002).

Appendix A

SHG Data analysis

A typical second harmonic generation (SHG) experiment collected 60000-180000 laser shots at a laser repetition rate of 1 kHz. For each shot incident on the sample two values were measured. The first was the input laser power, referred to from now on as the input power and the second was the intensity of the resultant second harmonic radiation, from now on referred to as the signal. Figure A1 shows a schematic of the signal processing scheme for the SHG experiments. As can be seen in the figure, the reference signal was recorded via a photodiode located just after the rotating neutral density filter, while the signal was measured via a photomultiplier tube after the sample. The signal from both detectors was passed to a pair of boxcar integrators, which integrated the resultant voltage profile from each detector. Due to the modulation of the laser power during the experiment, no averaging was done in either the signal or reference boxcars, only voltage integration. The integrated value from the boxcar was then passed into a DAQ, where it was digitized for data analysis in the computer.

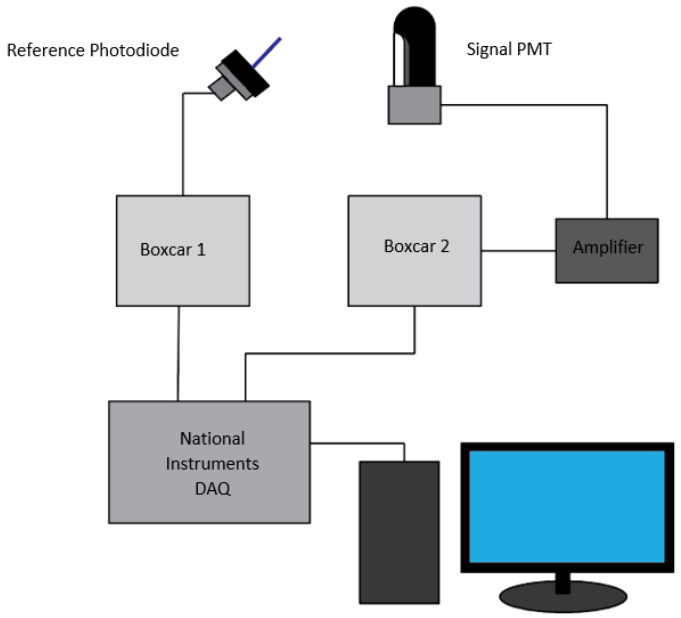

Figure A1: Signal processing scheme for SHG experiments

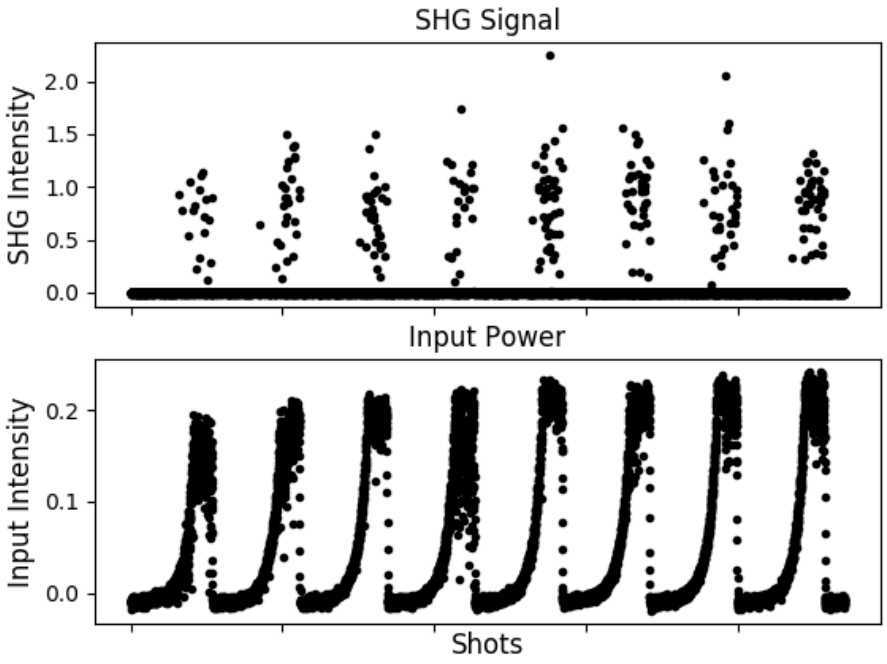

Figure A1: Example data trace for deep-UV second harmonic generation experiments

Figure A2 shows a representative data trace for the first 10000 shots of an SHG experiment. The top plot shows the SHG signal measured for each laser shot, while the bottom trace shows the input power as measured by the photodiode. To analyze the data from a given SHG experiment, the signal and reference values were first binned into 100 intensity bins and histogrammed. Figure A3 shows an example histogram of the reference and signal values for a typical SHG experiment. For the data shown in the histogram three intensity thresholds were defines. The first two thresholds, shown in red on Figure A2, were for the measured input power values and set upper and lower bounds for acceptable data points. Only laser shots with input powers which fell between these two bounds were included in the data analysis. These thresholds were set to cut out the very lowest and very highest power laser shots. These points were removed because they could cause artifacts in the fitting due to the abrupt transition between the low and high optical density regions on the power modulating N.D. wheel. The third threshold, shown in purple in the figure, was set for the signal histogram and determined for a given laser shot whether a photon reached the detector. A measured integrated signal value above this threshold was counted as the detection of a photon, while

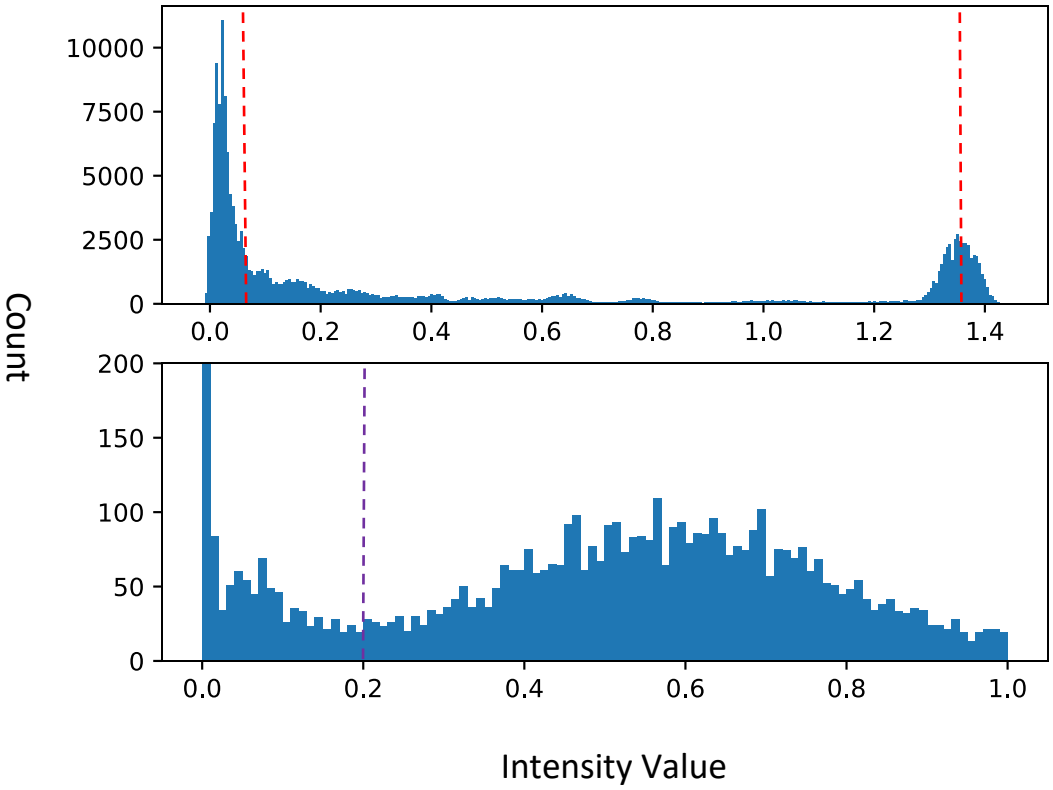

Figure A3: Histogram of input intensity and measured signal values

signals below this level were counted as no photon detected. The results of the data analysis were only modestly sensitive to the exact values of these three thresholds, but consistency in the measured data sets was maintained by setting the reference low and high bounds in the input power histogram to 10% and 90% of the maximum bin intensity respectively and by setting the signal threshold to a value of ~.2 for all experiments.

For each of the bins in the input power histogram the measured SHG intensity was then determined. Due to the low efficiency of the SHG process, the detected signal intensity for all input intensity bins was in the photon counting regime and Poissonian statistics were therefore applicable. The Poissonian probability distribution for discrete events, such as the arrival of a photon at the detector, can be written as:

$$P(k,\lambda) = \frac{e^{-\lambda}\lambda^{k}}{k!}$$

Here k is the number of events and λ is the average number of events per time period, in this case an event being the arrival of a photon at the detector. The probability of measuring no events, i.e. no photons, can therefore be written as:

$$P(0,\lambda) = \frac{e^{-\lambda}\lambda^{k0}}{0!} = e^{-\lambda}$$

The average number of events per time period, λ, can therefore be extracted from the probability of measuring zero events:

$$-\ln(P(0, \lambda))$$

For each input intensity bin, the probability of detecting zero photons was:

$$\lambda_{bin} = \left[\frac{N_{shots} - N_{shots,photon}}{N_{shots}}\right]$$

Here λ_{bin} is the intensity for a given input power bin, N_{shots} is the total number of laser pulses which fall in the input intensity bin and $N_{shots,\ photon}$ is the total number of shots in the bin for which a photon was detected, as determined by the previously discussed signal threshold. For each input intensity bin then, we determined the average number of photons detected per shot, λ_{bin}, using the above relations. We then plotted the measured value of λ_{bin} for each bin as a function of the input intensity squared. Recall that for a second order nonlinear process the intensity is given by the expression:

$$I_{SHG} \approx \chi^{(2)} I^2$$

As such, plotting the second harmonic signal as a function of the input intensity squared should yield a straight line with slope proportional to the value of $\chi^{(2)}$, as can be seen in Figure A4. In the case of the ion adsorption experiments, $\chi^{(2)}$ itself contains information about the number density of ions at the interface through the relation:

$$\chi^{(2)} = N_{ion}\langle\beta_{ion}\rangle$$

Here N_{ion} is the number density of ion and β_{ion} is the hyperpolarizability averaged over all molecular orientations. As such the slope is dependent on the number of ions adsorbed at the interface and hence on concentration. For each experiment the slope of the best fit line to the plot of SHG intensity vs. input squared was taken as the overall SHG intensity measured for that sample of sodium thiocyanate. These values are normalized to the best fit lines from pure water samples taken on the same day and added to the SHG isotherm.

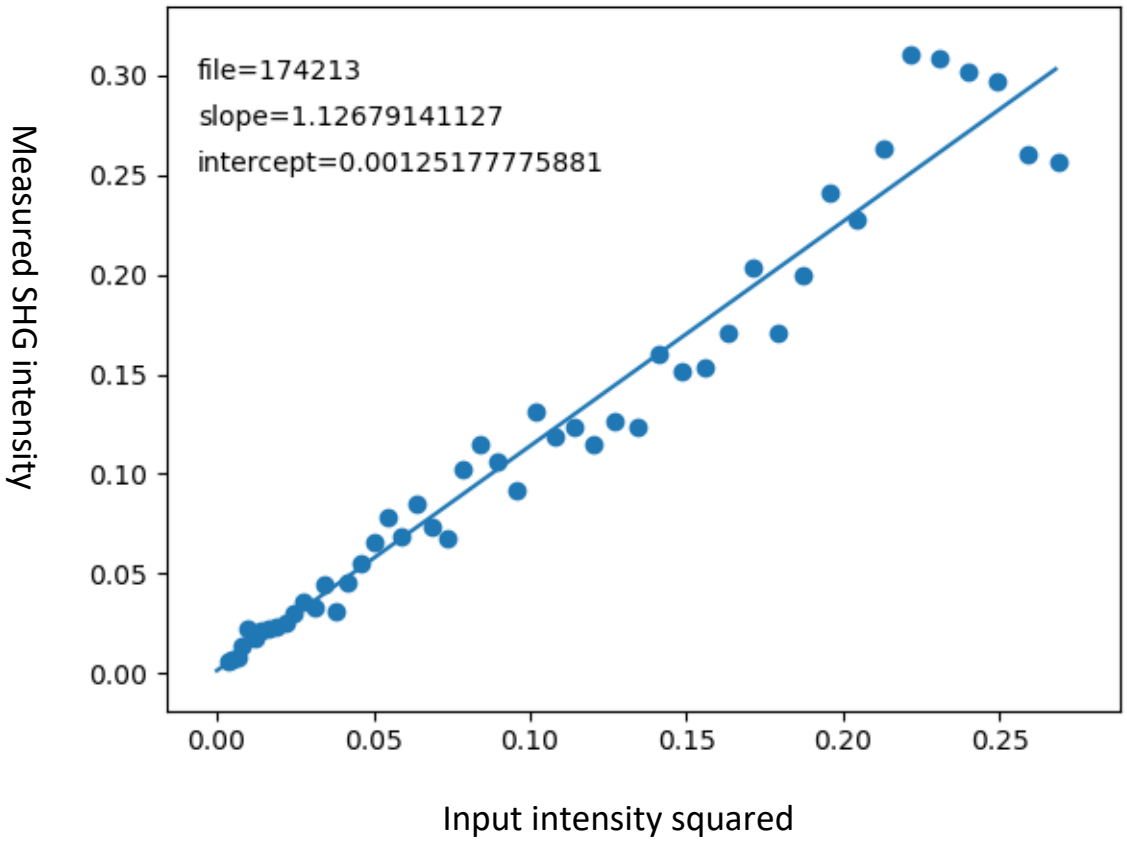

Figure A4: Example best fit line to SHG data